

ELECTRONIC AND MECHANICAL PROPERTIES OF CHEMICALLY FUNCTIONALIZED NANOWIRES

A Thesis
Presented to
The Academic Faculty

by

Sanjay K. Bidasaria

In Partial Fulfillment
of the Requirements for the Degree
Doctor of Philosophy in the
School of Physics

Georgia Institute of Technology
May 2009

ELECTRONIC AND MECHANICAL PROPERTIES OF CHEMICALLY FUNCTIONALIZED NANOWIRES

Approved by:

Professor Alexei Marchenkov, Adviser
School of Physics
Georgia Institute of Technology

Professor Elisa Riedo
School of Physics
Georgia Institute of Technology

Professor Phillip First
School of Physics
Georgia Institute of Technology

Professor William Russ Callen
School of Electrical Engineering
Georgia Institute of Technology

Professor Marcus Kindermann
School of Physics
Georgia Institute of Technology

Date Approved: 24 November 2008

To my parents,

Shankar L. Bidasaria,

Sakuntala D. Bidasaria,

ACKNOWLEDGEMENTS

I want to thank many people who have helped me during my time at Georgia Tech. Foremost, is my advisor, Professor Alexei Marchenkov; without whom I would not be where I am. Many other friends, co-workers and professors have guided me while I pursued my research. Dr. Brandon Donehoo, John Howard, and Daniel Benjamin were of great importance to the completion of my degree. Nikhil Sharma, Joanna Hass, and Professor Phillip First gave me valuable advice and assistance on many, many occasions, and hopefully will continue to do so in the years to come. The people with whom I have worked over the years are, in fact, too numerous to list here, and since my thesis is long enough already, so to all of you thanks, a lot. I would finally like to thank Judy Melton for reading and editing this dissertation, my thesis committee for reading this dissertation, as well as Professor Andrew Zangwill and Professor Mei-Yin Chou for helping me complete my degree here at Georgia Tech.

TABLE OF CONTENTS

DEDICATION	iii
ACKNOWLEDGEMENTS	iv
LIST OF TABLES	viii
LIST OF FIGURES	ix
SUMMARY	xi
I INTRODUCTION	1
II NIOBIUM NANOWIRE STRUCTURE	4
2.1 Density Functional Theory	5
2.1.1 The many body problem	5
2.1.2 Hohenberg-Kohn Theorems	6
2.1.3 Kohn-Sham Theory	7
2.1.4 The exchange-correlational functional	9
2.1.5 Pseudopotential	11
2.1.6 Representation of the wave functions	13
2.2 SIESTA	14
2.2.1 Quickstart	17
2.2.2 FDF File	18
2.2.3 Input parameters	19
2.2.4 Generationing the pseudopotential	22
2.3 Simulations and Results	23
2.3.1 Niobium dimer	23
2.3.2 Niobium dimer between two niobium atoms	25
2.3.3 Niobium dimer between two niobium electrodes	27
III ELECTRON TRANSPORT IN NANOWIRES	34
3.1 Length Scales	35

3.2	The Landauer Scattering Approach	37
3.3	Non-equilibrium Green's Function technique [27]	41
3.4	Atomistix Tool Kit	49
3.4.1	Two-Probe Set-up	52
3.4.2	Analysis of Output	55
3.5	Niobium Nanowire	56
3.5.1	Perfect Niobium Nanowire	56
3.5.2	Niobium nanowire point contact	60
3.6	Graphene	62
3.6.1	Transport Properties	63
3.6.2	Simulation and Results	64
IV	PICONEWTON FORCE SENSOR AND ITS CALIBRATION	70
4.1	Theoretical Background	71
4.1.1	Resonance frequency of cantilever	72
4.1.2	Hydrodynamic function	75
4.1.3	Adding an external mass on QTF	78
4.1.4	Electrical equivalent circuit of quartz tuning fork	80
4.1.5	Low temperature effect	82
4.2	Setup for calibration of QTF	82
4.2.1	Sample preparation	83
4.2.2	Frequency measurement	83
4.2.3	Tip Preparation	84
4.3	Results	85
4.3.1	Sample effect on resonance frequency	85
4.3.2	QTF and cantilever	86
4.3.3	Gravity effect	90
4.3.4	Low temperature effect	90
4.4	Experimental Setup	93

4.4.1	Vibration isolation	95
4.4.2	Tunneling current amplifier	97
4.4.3	Approach mechanism	99
4.4.4	Phase-locked loop	102
4.5	Mechanically Controllable Break Junctions [66, 67]	104
V	SQUEEZE-FILM EFFECT	105
5.1	Theoretical background	106
5.2	Results and analysis	110
5.3	Conclusion	116
APPENDIX A	MEASUREMENT OF TRANSFER FUNCTION	118
APPENDIX B	MODELING IN COMSOL MULTIPHYSICS	122
APPENDIX C	PHASE LOCK LOOP CHIP MC14046B CONFIGURATION	128
REFERENCES	131
VITA	137

LIST OF TABLES

1	Resonance Frequency at Room Pressure for QTF after addition of different masses.	90
---	--	----

LIST OF FIGURES

1	Self consistency algorithm for density functional Theory	14
2	Relaxed niobium dimer	25
3	$\Delta\rho$ (DRHO) and ρ (RHO) of relaxed niobium dimer	26
4	Niobium dimer between two niobium atoms	28
5	Pseudocharge density for niobium dimer between two niobium atoms	28
6	$\Delta\rho$ for niobium dimer between two niobium atoms	28
7	ρ of symmetric niobium dimer between two niobium electrodes	30
8	$\Delta\rho$ of symmetric niobium dimer between two niobium electrodes . . .	30
9	Asymmetric niobium dimer between two niobium electrodes	31
10	$\Delta\rho$ for asymmetric niobium dimer between two niobium electrodes . .	31
11	Tilted niobium dimer between two niobium electrodes	32
12	Tilted niobium dimer distances between two niobium electrodes . . .	33
13	Scattering formalism	38
14	Screenshot of package.	52
15	Transmission of a perfect niobium nanowire.	57
16	Eigenstate of niobium linear chain.	58
17	Transmission spectrum of point contact wire.	60
18	Transmission eigenstate 0	61
19	Transmission eigenstate 1	61
20	Armchair and zigzag graphene.	64
21	Transmission eigenstates of zigzag graphene.	67
22	Transmission spectrum and DOS of zigzag graphene.	68
23	Transmission eigenstates of armchair graphene.	68
24	Transmission spectrum and DOS of armchair graphene.	69
25	Pressure profile of fluid.	76
26	Velocity of fluid around the cantilever.	77
27	Hydrodynamic function obtained from finite-element simulations. . .	78

28	Butterworth-Van Dyke circuit.	80
29	Transfer function of Butterworth-Van-Dyke filter.	81
30	Quartz tuning fork	82
31	Tip preparation	85
32	Sample effect on resonance frequency	87
33	Ceramic substrate	88
34	Theoretical and experimental comparisons of $-\Delta f/f_0$	89
35	Variations of $-\Delta f/f_0$ after adding different masses.	91
36	Effect of gravitational force.	92
37	Parallel and perpendicular arrangements of the QTF prongs with respect to gravity.	93
38	Low temperature measurements.	94
39	Current to voltage amplifier circuit.	97
40	Operational amplifier circuit to convert small current to measurable voltage.	98
41	Approach mechanism design.	100
42	Step motor	101
43	Piezo stack actuator	102
44	Phase-locked loop	103
45	Dimensions of tuning fork.	111
46	Polynomial fit	112
47	Theoretical model generated to fit the experiment	113
48	Hydrodynamic function	114
49	Squeeze-film effect on QTFs	115
50	Labview front panel for data acquisition from SR780 network analyzer.	121
51	Mesh generated from the finite-element analysis.	126
52	PLL chip MC14046B	129

SUMMARY

Organic and inorganic nanostructured materials, nano- and mesoscale objects and devices, and their integration into existing microelectronic technologies have been at the center of recent fundamental and applied research in nanotechnology. One of the critical needs is to develop an enhanced predictive capability of structure-property correlations and enable robust high performance systems by design. My thesis work was concerned with the theoretical and experimental studies of electronic and mechanical properties of chemically functionalized nanowires.

I will first describe a theoretical approach for investigating structure-property correlations in atomic-sized metallic wires based on the Density Functional Theory (DFT) for structure calculations and the Non-equilibrium Green's Function (NEGF) technique for electronic transport properties simulations. This synergistic approach is shown to yield the atomic structure of the smallest niobium nanowires. Furthermore, the method was applied to simulate electronic properties of chemically functionalized graphene nanoribbons.

Further, I will demonstrate an experimental technique for simultaneous measurements of force and conductance in atomic-size objects based on quartz tuning fork piezoelectric sensors. A peculiar scaling effect, relevant for a broad range of test and measurement applications, namely the squeeze film effect, was observed during the development of the sensors. Using theoretical analysis based on finite element simulations of the hydrodynamic behavior of the sensors in a broad range of ambient conditions, I explain the observed phenomenon.

CHAPTER I

INTRODUCTION

This thesis concerns with the theoretical and experimental descriptions of the electronic and mechanical properties of nanostructures. The technological impetus for studying nanostructures came from molecular electronics. In recent years research in this field has exploded due to a proliferation of new and exciting techniques (e-beam lithography, self-assembled monolayers, etc.) for producing atomic level structures. Coupling of these techniques with the ability to manipulate atomic systems (such as Scanning Tunneling Microscopes (STM), Atomic Force Microscopes (AFM), or Mechanically Controllable Break Junctions (MCBJ)) opens the possibility to create novel quantum coherent devices for both engineering applications and research into fundamental physics. At present the size of commercially available transistors is about 45 nanometers (nm) which is roughly 150 metal atoms in a row. Although new fabrication techniques allow a further 20 nm decrease in size, the transition to the atomic scale is, however, not just a simple continuation of the on-going device miniaturization, but requires a true quantum approach to the system. Consequently, the fabrication and fundamental working principles of the devices require a thorough understanding of the properties of basic nanostructures like nanowires, ribbons, and the point contacts. The development of theoretical ab initio methods like the Density Functional Theory (DFT) for structure calculations and Non-equilibrium Green's Function (NEGF) formalism for electronic transport has accelerated the research further, since now the experimental observations can be verified by accurate modeling.

Before detailing the experimental results and their implications, Chapter II covers structure calculations of mesoscopic conductors. Along with covering the basics

of DFT and related computational techniques this chapter contains calculations of the structure of the smallest niobium nanowires. Just before breaking, the smallest nanowire consists of a dimer made of two niobium atoms suspended between bulk electrodes. This result is consistent with the previous calculations of the structure of niobium nanowires. We also investigate the changes in the morphology of niobium nanowires with elongation and compression. Comparison of our calculation with experimental and other theoretical results gives a verification of our method.

Chapter III deals with the theory of quantum electronic transport properties in nanowires. First, the Landauer's semi-phenomenological model of transport is introduced, followed by a brief introduction into the NEGF method. The relation between the two theories is shown as well. The NEGF calculations were performed on two systems: niobium dimer nanowires and chemically functionalized graphene nanoribbons. Niobium nanowire calculations gave the total conductance values consistent with both the experimental data and similar theoretical calculations. In the case of graphene nanoribbons, the presence of aromatic molecules in the vicinity of the ribbon was shown to give a strong modification of the conductance spectrum at finite voltages. This suggests a potential applications for graphene nanoribbons as chemical sensors.

Among important topics in nanoscale physics is the structure and transport property correlations in nanosystems. Therefore, innovative research methods and techniques capable of measuring several of the basic properties simultaneously are required. In Chapter IV, I present design and calibration of a force sensor, potentially capable of pico-Newton force resolution, which can be combined with a scanning tunneling microscope for simultaneous force-conductance measurement. An originally developed calibration procedure, based on the changes of the resonant frequency of the sensor cantilever in gas at different pressures, is described and verified through both experiments and finite-element computer modeling.

Finally, Chapter V describes a peculiar scaling effect observed at low pressures, the squeeze film effect. The onset of this phenomenon occurs at the pressure where the mean free path of the gas molecules become comparable to the gap height between the oscillating cantilever and the surface. Significant changes in the behavior of the resonance frequency of the probe were observed at lower pressures. A quantitative explanation of this behavior, is based on the laws of hydrodynamics is given. In addition, a semi phenomenological model for the change of the resonant frequency was developed, which successfully describes the behavior of the sensor over six decades of pressure - from atmospheric to all the way deep into the squeeze layer regime.

In Appendices, I describe relevant techniques for different parts of the thesis: Appendix A describes the measurement of transfer function and phase methods to obtain the resonance frequency of the vibrating cantilever. Finite-element methods were used for the computer modeling of the cantilever and the details are given in Appendix B. Finally, Appendix C describes the electronic circuits based on the phase-locked loop, for tracking the change in resonance frequency of cantilever continuously.

CHAPTER II

NIObIUM NANOWIRE STRUCTURE

The study of electronic structure is a complex many-body problem, where the full solution is not possible in practice. It demands the quantum mechanical description of electrons in atoms, molecules and condensed phases. Such a description amounts to an investigation of the spectral properties of Schrödinger or Hamiltonian operators; which are self-adjoint, partial differential operators. In general, an exact solution of the spectral problem is not possible due to the complicated correlations induced in the electron positions by the mutual Coulomb interaction, and consequently approximate methods are required. It was in 1964, when Hohenberg and Kohn (HK) showed that the ground state energy of an electron system is uniquely determined by the ground state electron density [1]. This research established a rigorous framework for earlier density based theories like the Thomas-Fermi theory, and marked the beginning of Density Functional Theory (DFT). Later, in 1965 Kohn and Sham invented a constructive scheme for implementing the HK map of the ground state density to the ground state energy [2]. The Kohn-Sham scheme basically consolidates the complications arising from the mutual electron interaction into a so-called exchange-correlation functional and then treats this functional approximately. Electronic structure calculations based on density functional theory is presented in this chapter.

The chapter starts with a brief introduction to the many-body problem followed by the Hohenberg-Kohn theorems. The Kohn-Sham scheme is then introduced followed by a discussion of the exchange-correlation functional and its various approximations for the pseudopotential and representation of wave functions. Then we discuss the

program SIESTA (Spanish Initiative for Electronic Simulations with Thousands of Atoms), which is one of the numerical implementation of DFT. We also present the simulation parameters under which the program was used. Finally, we compare the results obtained from this program with results for the structure of the niobium nanowire published earlier [3].

2.1 *Density Functional Theory*

2.1.1 The many body problem

A many-body Hamiltonian is a self-adjoint operator in a Hilbert space which governs the dynamics of the negatively charged electrons and positively charged nuclei which constitute matter. The many-body Hamiltonian is significantly simplified when the large difference in mass between electrons and nuclei, $m_e/M_n \approx 10^{-3} - 10^{-5}$, is used to decouple the nuclear and electron systems. The simplification is more commonly referred to as Born-Oppenheimer approximation [4]. Physically, the decoupling implies that the light electrons respond instantaneously to changes in the nuclear positions. Thus, a sum of the electron kinetic energy, T , the attractive interaction between electrons and nuclei, V_{en} , the Coulomb repulsion between the electrons, V_{ee} , and the Coulomb repulsion between the nuclei, V_{nn} gives the Hamiltonian describing N electrons moving in the potential from M fixed nuclei of charge $Z_k > 0$:

$$H = T + V_{en} + V_{ee} + V_{nn}. \quad (1)$$

The term V_{nn} is a constant depending only on the nuclear positions that enter the Hamiltonian as parameters. The possible presence of force fields other than those originating from the nuclear charges are taken into account by generalizing the Hamiltonian such that the term V_{en} is replaced by V_{ext} , the potential due to these external forces. Thus, the Hamiltonian of Eq. (1) takes the form:

$$H = -\frac{1}{2} \sum_{i=1}^N \nabla_i^2 + \sum_{i=1}^N \sum_{k=1}^M \frac{Z_k}{|\mathbf{r}_i - \mathbf{R}_k|} + \sum_{i<j}^N \frac{1}{|\mathbf{r}_i - \mathbf{r}_j|} + \sum_{k<l}^M \frac{Z_k Z_l}{|\mathbf{R}_k - \mathbf{R}_l|}, \quad (2)$$

where $\mathbf{r}_i, \mathbf{r}_j$ represents the position vector of electrons and $\mathbf{R}_k, \mathbf{R}_l$ represents the position vector of the nuclei. This Hamiltonian is a partial differential operator whose existence of self-adjoint extensions is intimately related to the existence of the ground state. The ground state and the corresponding ground state energy satisfy the eigenvalue equation $H\Psi_0 = E_0\Psi_0$, while the excited states (if they exist) are eigenstates with eigenvalues $E_n > E_0$. Presently, the most popular and powerful method for calculating ground state properties of atomic-scale systems is the Density Functional Theory (DFT) [5, 6]. In contrast to the N-particle wave function used in the variational schemes or the Green's function used in many-particle perturbation theory, the central object in DFT is the electron density. The next three sections give a general introduction to DFT.

2.1.2 Hohenberg-Kohn Theorems

In principle, DFT is an exact theory with only one Born-Oppenheimer approximation. However, its practical realization will require additional approximations. DFT is based on two variational theorems, also known as the Hohenberg-Kohn (HK) theorems [1]. The first theorem states that for systems with a non-degenerate ground state, there is a one-to-one correspondence between the external potential, $v_{\text{ext}}(\mathbf{r})$, of the many-body Hamiltonian, (Eq. (1)) and the corresponding ground state electron density, $n(\mathbf{r})$. In other words, two potentials differing by more than a constant lead to different ground state densities. This observation has profound theoretical consequences because it sets up a correspondence between densities and ground states: $n(\mathbf{r}) \rightarrow \Psi_0[n]$. This follows since $n(\mathbf{r})$ determines $v_{\text{ext}}(\mathbf{r})$ that in turn defines H and thus its ground state. The correspondence $n \rightarrow \langle \Psi_0[n] | A | \Psi_0[n] \rangle$ shows that all ground state properties are determined by the ground state density. This holds in particular for the ground state energy for which we introduce the functional

$$E_v[n] = \langle \Psi[n] | T + V_{\text{ee}} | \Psi[n] \rangle + \int v_{\text{ext}}(\mathbf{r})n(\mathbf{r})d\mathbf{r}. \quad (3)$$

The subscript v indicates the dependence on the external potential. An application of the variational principle shows that the ground state energy and density can be obtained by minimizing $E_v[n]$ over the set of densities originating from non-degenerate ground states. The DFT can be used for a degenerate ground state by relying on functionals (that are unique for the state) instead of the construction of the wavefunctions that could be different for ground state. Since the full Hamiltonian is the functional of electron density, it is desirable to consider the sum of kinetic and interaction energies as a functional of density too because then we can use the universality of this functional for not depending on the system properties which are given by external potential. I denote this functional $F[n]$.

The second theorem states the variational principle for the universal functional F . For a given external potential V_{ext} the global minimum of the universal functional:

$$E[n(\mathbf{r})] = F[n(\mathbf{r})] + \int V_{ext}(\mathbf{r})n(\mathbf{r})d\mathbf{r} \quad (4)$$

gives the exact ground state energy E_0 . Any electron density distribution $n(\mathbf{r})$ is indeed an exact ground state density on which the above global minimum is realized and since the ground state exists for any physical system, the question of existence of ground state density does not rise. The second theorem provides a way to construct the ground state density and, in view of first theorem, all other properties of the system by minimizing the functional E . No other information is required. However, the explicit form of this functional is unknown and the core problem in DFT is to find good approximations to F . In the next section we discuss a less direct, though much more accurate, approach for determining F .

2.1.3 Kohn-Sham Theory

The decomposition of the usual variational problem into a complicated universal part and a relatively simple system-dependent part is the main achievement of the density functional formalism. However, still the HK theorems do not provide a way

to minimize the energy functional or the functional itself. So Kohn and Sham (KS) [2] extended the basic idea of the Thomas-Fermi model, namely, to obtain the ground state kinetic energy from a non-interacting reference system. For a given interacting ground state density, $n(\mathbf{r})$, KS assumed the existence of an external potential, $V_s(\mathbf{r})$, such that the ground state density of the non-interacting Hamiltonian,

$$H_s = T + V_s, \quad (5)$$

is equal to $n(\mathbf{r})$. In other words, KS treated the “interacting electrons” as “non-interacting electrons in an effective potential.” Since V_s is uniquely determined by n (by the non-interacting version of the HK theorem), we have the density functional:

$$E_s[n] = T_s[n] + \int V_s(\mathbf{r})n(\mathbf{r})d\mathbf{r}, \quad (6)$$

where T_s is the kinetic energy of the non-interacting electron gas of a system with density $n(\mathbf{r})$. Further, the energy functional (Eq. (3)) of the interacting system can be decomposed as:

$$E_v[n] = T_s[n] + \frac{1}{2} \int \int \frac{1}{|\mathbf{r} - \mathbf{r}'|} n(\mathbf{r})n(\mathbf{r}')d\mathbf{r}d\mathbf{r}' + \int V_{\text{ext}}(\mathbf{r})n(\mathbf{r})d\mathbf{r} + E_{\text{xc}}[n], \quad (7)$$

where we have introduced the exchange-correlation (xc-) functional:

$$E_{\text{xc}}[n] = F[n] - T_s[n] - \frac{1}{2} \int \int \frac{1}{|\mathbf{r} - \mathbf{r}'|} n(\mathbf{r})n(\mathbf{r}')d\mathbf{r}d\mathbf{r}' + \int V_{\text{ext}}(\mathbf{r})n(\mathbf{r})d\mathbf{r}. \quad (8)$$

The xc-functional contains the correlation contribution to the kinetic energy as well as the electron interaction energy beyond the Hartree approximation. The philosophy of the decomposition is to extract as much energy as possible and then hope that the rest (E_{xc}) is a small correction for which reasonable approximations can be constructed. Note that E_{xc} , like F , is a universal functional. Next we address the determination of the potential V_s . The ground state density, n_0 , is by assumption a common minimizer for $E_v[n]$ and $E_s[n]$ when the variational densities are subject

to the condition $\int n(\mathbf{r})d\mathbf{r} = N$. In terms of functional derivatives this condition is expressed by:

$$\left. \frac{\delta}{\delta n} \right|_{n_0} \left(E_v[n] - \mu \int n(\mathbf{r})d\mathbf{r} \right) = 0 \quad (9)$$

with a similar equation for E_s . The number μ is a Lagrange multiplier invoking the condition of constant particle number. To within a trivial constant these variational equations, together with equations (6) and (7), determine V_s :

$$V_s(\mathbf{r}) = V_{\text{ext}}(\mathbf{r}) + \int \frac{1}{|\mathbf{r} - \mathbf{r}'|} n_0(\mathbf{r}')d\mathbf{r}' + V_{\text{xc}}([n_0]; \mathbf{r}), \quad (10)$$

where the exchange-correlation potential is defined by

$$V_{\text{xc}}([n_0]; \mathbf{r}) = \left. \frac{\delta E_{\text{xc}}[n]}{\delta n(\mathbf{r})} \right|_{n_0}. \quad (11)$$

The potential V_s and the single-particle Hamiltonian (Eq. (5)) are referred to as the effective or Kohn-Sham potential Hamiltonian. A similar prefix is used for the corresponding single-particle eigenstates, ψ_n , and eigenvalues, ε_n . The ground state density, n_0 , can be obtained from the N lowest Kohn-Sham eigenstates. Since the Kohn-Sham potential in turn depends on n_0 , the solution must in practice be obtained through a self-consistent procedure.

2.1.4 The exchange-correlational functional

Within the Kohn-Sham scheme, all effects originating from the correlation between the positions of the electrons in the many-body ground state are contained in the xc-functional. In fact, neglecting E_{xc} leads to the Hartree approximation. The first attempt was the Local Density Approximation (LDA) [2], where it is assumed that the xc-energy density $\varepsilon(\mathbf{r})$ in the functional $E = \int n(\mathbf{r})\varepsilon(\mathbf{r})d\mathbf{r}$ takes the form

$$\varepsilon(\mathbf{r}) = \varepsilon[n(\mathbf{r}')](\mathbf{r}) \approx \varepsilon[n(\mathbf{r})](\mathbf{r}) = \varepsilon_{\text{lda}}(n(\mathbf{r}), \mathbf{r}) \quad (12)$$

making $\varepsilon(\mathbf{r})$ a function of position of the observation point and the electron density at that point. Then the real density function $n(\mathbf{r})$ is approximated and replaced by

that of a free homogeneous electron gas in infinite space without external fields. So, the exchange correlation potential can be calculated for the free homogenous electron gas as a function of electron density and this also satisfies the universal property of the functional. In practice xc-energy density, ε_{lda} , is represented by some analytic function fitted to numerical calculations [7, 8, 9]. Although the LDA is only valid for slowly varying densities, it performs surprisingly well for a much larger class of systems [10]. One possible explanation for the unexpected success of LDA is that the partitioning of the energy is in such a way, that the exchange-correlation part is only about one percent of the total energy. Another reason is that the exchange-correlation hole describing the mutual electron repulsion is correctly described in LDA. It is often pointed out, that the errors appearing through LDA effectively and often cancel out in DFT.

LDA is further improved by considering the gradient of the density instead of the spatially homogeneous density $n(\mathbf{r})$, at any point \mathbf{r} . The first attempt “gradient-expansion approximations” (GEA) tries to systematically calculate gradient corrections of the form $|\Delta n(\mathbf{r})|$, $|\Delta n(\mathbf{r})|^2$, $\Delta^2 n(\mathbf{r})$, etc., to the LDA. However, in practice, the inclusion of the low-order gradient corrections never improves on the LDA and often worsens it. On the other hand, higher-order corrections like $|\Delta n(\mathbf{r})|^\alpha$ or $\Delta^\beta n(\mathbf{r})$ (with $\alpha, \beta > 2$) are exceedingly difficult to calculate, and little is known about them. A major breakthrough was the so-called Generalized Gradient Approximation (GGA), where the more general functions of $n(\mathbf{r})$ and $\Delta n(\mathbf{r})$, which need not proceed order by order, were used instead of a power-series-like systematic gradient expansions [11]. Such functionals, take the general form:

$$E_{\text{xc}} = \int f(n(\mathbf{r}), \nabla n(\mathbf{r})) d\mathbf{r}. \quad (13)$$

In the above equation different GGAs differ in the choice of the functions $f(n(\mathbf{r}), \nabla n(\mathbf{r}))$ and this makes different GGAs much more different from each other than the different parametrization of the LDAs. The xc-functional used for most of the calculations

presented in this thesis is the GGA of Perdew, Burke, and Ernzerhof (PBE) [12] and revised PBE (RPBE) [13] GGA functionals have been applied.

2.1.5 Pseudopotential

The pseudopotential for a particular chemical system is approximated by some universal *atomic pseudopotential* for the free atom. The fact that the chemical properties of an atom are determined almost entirely by their outermost valence electrons is used in the pseudopotential method. So, the core electrons are chemically inert, therefore they are ignored in the self-consistent solution of the KS problem, and the core states are simply frozen to those obtained for the free atom. This simplification is connected with a corresponding replacement of the true valence wave functions with pseudo-wave functions that lead to a major reduction in the number of wave functions which have to be handled. The pseudopotential is designed to make the pseudo-wave functions node-less and as smooth as possible, thereby rendering them more easy to represent. The generation of pseudopotentials usually follow three basic guidelines [16]:

1. The pseudopotential should reproduce the true valence eigenvalues for the isolated atom.
2. The pseudo-wave functions should coincide with the true valence wave functions, beyond a given core radius, r_c .
3. The integrated charge of the pseudo-wave function within the core should equal the corresponding charge of the true valence wave function, and this condition gives pseudopotentials that are called norm-conserving pseudopotentials.

The scattering properties of the atom are guaranteed by the continuity of the wave functions, and together with charge conservation, the scheme produces correct ground

state density outside of the atomic core regions. However, the space in the region outside and inside the spheres surrounding the atomic cores is split by this procedure and additional spherical coordinates defining the spheres are introduced in the calculations making the norm-conserving pseudopotential less efficient. To resolve this problem, a method [14] called projected augmented wave (PAW) is introduced in which instead of partitioning the space, the wave function is partitioned. The partitioned wavefunction is equal to pseudo wavefunction defined everywhere, minus the pseudo wavefunction inside the pseudization spheres plus the exact wavefunction inside the pseudization spheres. A method physically similar to PAW is the ultrasoft pseudopotentials, pointing to the improved smoothness of the associated pseudo-wave functions [15]. This is especially good for some elements like oxygen and nickel where the valence states are so localized that a representation of the pseudo-wave functions in terms of plane waves requires a very high energy cut-off. Application of ultrasoft pseudopotentials implies that the pseudo-wave functions, $\tilde{\psi}_n$ are not orthonormal in the usual sense, but instead satisfy the generalized orthonormality relation, $\langle \tilde{\psi}_n | S | \tilde{\psi}_m \rangle = \delta_{nm}$, where $S = I + \sum_{ij} |\beta_i^{(n)}\rangle Q_{ij}^{(n)} \langle \beta_j^{(n)}|$ is a generalized non-local overlap operator [15]. Although these methods resolve most of the issues, another problem remains. The rapid variations of the valence states in the core region (where their kinetic energy is very high) are extremely difficult to represent in terms of a fixed basis set. In the pseudopotential method this problem is overcome by replacing the strong field from the nucleus and the core electrons by a softer pseudopotential [16, 17]. Such a replacement is always connected with a corresponding replacement of the true valence wave functions with pseudo-wave functions. In this work norm-conserving soft pseudopotentials have been used for all calculations.

2.1.6 Representation of the wave functions

The wavefunction is expanded in a basis set, $\{\phi_n\}$ in order to determine the spectrum of the KS Hamiltonian:

$$\psi_n(\mathbf{r}) = \sum_m (\mathbf{c}_n)_m \phi_m(\mathbf{r}). \quad (14)$$

The KS eigenvalues, ε_n , and eigenvectors, c_n , are found as the solutions to the generalized matrix eigenvalue problem, $\mathbf{H}\mathbf{c}_n = \varepsilon_n \mathbf{S}\mathbf{c}_n$, where $\mathbf{H}_{nm} = \langle \phi_n | H | \phi_m \rangle$ and $\mathbf{S}_{nm} = \langle \phi_n | \phi_m \rangle$ are the Hamiltonian and overlap matrices. In practical computer implementations only a finite number of basis functions can be handled, and thus the basis set has to be truncated. Basis sets used for electronic structure calculations can be roughly divided into two groups. The first type of basis functions covers the system-independent functions such as plane waves [18] or wavelets [19]. The main advantage of these basis sets, is that their size can be systematically increased until the result of the calculation has converged. However, the main disadvantage is that the number of basis function required to obtain convergence is normally so large that direct solution of the matrix eigenvalue problem within the entire basis space is not possible. Therefore one has to use iterative methods to determine the lowest (occupied) part of the spectrum [18].

The second type of basis set is designed to mimic the exact eigenstates of the system already at the outset. Examples of such basis sets are the atomic orbitals used in the DFT program SIESTA [20, 22] and the atom-centered Gaussian orbitals used in the Gaussian electronic structure package [21]. In general, these DFT codes give reliable results with a relatively small number of basis functions, making them optimal for large scale computations where high accuracy is less crucial. On the other hand there is no consistent way to extend these basis sets and thereby converge the results with respect to the size of the basis. In this work the second type of basis sets have been used for all calculations, because we wanted to obtain results on a desktop computer. Further, the self consistent algorithm used in the package is shown in Fig.

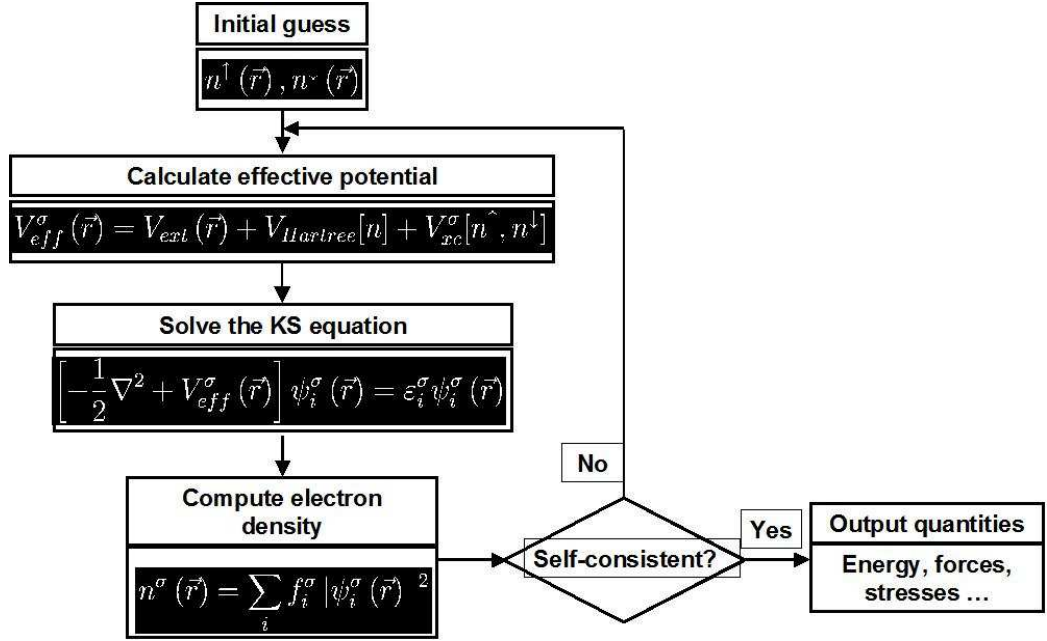


Figure 1: Self consistency algorithm for density functional Theory.

1.

2.2 SIESTA

Spanish Initiative for Electronic Simulations with Thousands of Atoms (SIESTA) is not only a computer program implementation but also a method to perform electronic structure calculations and *ab initio* molecular dynamics simulations of molecules and solids. It uses the standard KS self-consistent density functional method in the local density (LDA) or generalized gradient (GGA) approximations with norm-conserving pseudopotentials. Additionally, it projects the electron wavefunctions and density onto a real-space grid in order to calculate the Hartree and exchange-correlation potentials and their matrix elements.

SIESTA solves the Kohn-Sham equations by expanding the wave functions using localized, numerical orbitals as basis sets. It uses atomic orbitals as basis set, allowing multiple-zeta and angular momenta, polarization and off-site orbitals. The radial shape of every orbital is numerical, and any shape can be used and provided by

the user with the condition that it has to be strictly zero beyond a user-provided distance from the corresponding nucleus. This condition is the key for calculating the Hamiltonian and overlap matrices in $O(N)$ (order N) operations. It also allows the use of localized linear combinations of the occupied orbitals like the valence-bond, or Wannier-like functions, making the computer time and memory scale linearly with the number of atoms. Using the nomenclature of quantum chemistry, the hierarchy of basis sets are established, from single- ζ (zeta) to multiple-zeta. Four different types of basis sets are available in SIESTA, and they are listed below in order of increasing size and accuracy.

1. `SingleZeta`; least accurate; a single basis orbital for each valence orbital.
2. `SingleZetaPolarized`; `SingleZeta` plus one basis orbital for the first unoccupied shell.
3. `DoubleZeta`; two basis orbitals for each valence orbital.
4. `DoubleZetaPolarized`; `DoubleZeta` plus one basis orbital for the first unoccupied shell.

In most practical cases, the `DoubleZetaPolarized` basis set gives very good accuracy, but for large systems with many (e.g., transition metal) atoms this basis set might be too big to fit in the computer memory. A brief theoretical background of the basis sets is given below.

Single Zeta Orbitals: The single zeta basis set covers the valence configuration, which contains all open shells and, in some cases, also some high-energy closed shells (such as the d shell in transition metals). The basis functions are found by solving the radial Schrödinger equation for the atom with a confinement potential. The confinement potential is defined by the parameters, V_0 , r_{inn} and r_c . Here V_0 defines the softness of the confined potential. If this parameter is zero, a hard-wall potential is used.

The parameter r_c determines the confinement radius of the numerical orbitals. The confinement radius is taken as the position of the first node of the wave function with energy $E_{nl} + \Delta E$, where E_{nl} is the energy of the corresponding pseudo-atomic eigenstate and ΔE is the excitation energy of pseudo atomic orbital due to its confinement to a finite range. Additionally, r_{inn} is the inner radius where the soft confinement potential starts off.

Double Zeta Orbitals: The double zeta orbital is constructed through a procedure reminiscent of the splitting of a Gaussian basis set. The split orbital is obtained by constructing an analytical basis orbital that matches the first zeta orbital smoothly at the radius r^{split} . The functional form used for the split orbital is,

$$\phi_l^{2\zeta}(r) = \begin{cases} r^l(a_l - b_l r^2), & \text{if } r < r_l^{\text{split}} \\ \phi_l^{1\zeta}(r), & \text{if } r \geq r_l^{\text{split}}. \end{cases} \quad (15)$$

The split radius r^{split} is determined by specifying a split norm parameter. This parameter finds the matching radius of an analytical orbital which splits the first zeta orbital into a double zeta basis. The matching radius is determined by specifying that the norm of the split orbital relative to the norm of the first zeta orbital should have the value `split_norm`. Valid numbers are in the range from (but not including) 0 to 1.

Polarization Orbitals: The polarization orbitals have higher angular momenta than the valence orbitals. Such orbitals are generated by perturbing the single zeta orbitals by an electric field, and extracting the $l + 1$ component of the perturbed orbital.

Further, SIESTA is written in Fortran 90 and the computer memory is allocated dynamically. Also, it may be compiled for serial or parallel processors' execution. All these reasons make simulations with several hundred atoms feasible with modest workstations and desktop computers. In output, SIESTA provides total and partial energies, atomic forces, stress tensor, electric dipole moment, atomic, orbital and bond

populations (Mulliken), and electron density. It also provides geometry relaxation for fixed or variable cell, constant-temperature molecular dynamics (Nose thermostat), variable cell dynamics (Parrinello-Rahman), spin polarized calculations (collinear or not), k-sampling of the Brillouin zone, and projected density of states. In the following sections, an overview of the SIESTA package is given.

2.2.1 Quickstart

An appropriate Fortran Compiler is required for installing SIESTA. Although the compiler can be downloaded and run under Windows operating system, Linux is more appropriate and stable operating system for programming and scientific simulations. Next we downloaded SIESTA, which is distributed freely for academic use after registration.

The downloaded file for SIESTA is in compressed format that is unpacked and then installed to obtain the fully functional program. The source code with the Makefile resides in the SRC directory. The command `./configure` in a terminal will start an automatic scan of your system and then the `make` command will complete the required installation. Although we did not edit, the configure script might need some help in order to find the Fortran compiler. Also, it is recommended to install (unpack and configure) SIESTA in `/usr/local` directory and then set the PATH and link as suitable.

A fast way to test the installation of SIESTA and to get a feeling for the workings of the program is implemented in directory `Tests`. There are several subdirectories with pre-packaged (Flexible Data Format) `FDF` files and pseudopotential references in this directory. After compiling SIESTA the command `make` will run the program in subdirectory `work`, where all the resulting files can be found.

2.2.2 FDF File

The main input file, which is read as the standard input, contains **all** the physical data of the system and the parameters of the simulation to be performed. This file is written in a special format called FDF that allows data to be given in any order or to be omitted in favor of default values. Here we offer a glimpse of it through the following rules:

1. The FDF syntax is a “data label” followed by its value. Values that are not specified in the data file are assigned a default value.
2. FDF labels are case insensitive, and characters ‘-’ ‘_’ ‘.’ in a data label are ignored. Thus, `LatticeConstant` and `lattice_constant` represent the same label.
3. All text following the ‘#’ character is taken as comment.
4. Logical values can be specified as `T`, `true`, `.true.`, `yes`, `F`, `false`, `.false.`, `no`. Also a blank is equivalent to `true`.
5. Character strings should not be in apostrophes.
6. Real values which represent a physical magnitude must be followed by its units. The function `fdf_convfac` in file `~/siesta/Src/fdf/fdf.f` has the units that are currently supported by the program. Also, it is important to include a decimal point in a real number to distinguish it from an integer, in order to prevent ambiguities when mixing the types on the same input line.
7. Complex data structures are called blocks and are placed between `%block` label and a `%endblock` label.
8. It has the flexibility to include other FDF files and redirect the search for a particular data label to another file. If a data label appears more than once, its

first appearance is used.

Almost all of the tags are optional except `NumberOfSpecies`, `NumberOfAtoms`, and `ChemicalSpeciesLabel` in addition to introducing the atomic positions via `AtomicCoordinatesAndAtomicSpecies`. Rest is assigned default by SIESTA (which can be seen in `out.fdf` file) if a given tag is not found in the input file.

2.2.3 Input parameters

The `fdf` file takes several input parameters. This section describes the changes made in the different input parameters during the customizing of SIESTA.

- **Geometry Constraints:** The data label fix constraints to the change of atomic coordinates during geometry relaxation or molecular dynamics. More details are available in the instruction manual for SIESTA [22]. However, in this section only the details used in simulation of the niobium wire are presented. Geometry Constraints is a block input, and it can take several constraints within the block. We needed to fix the position of 40 atoms out of 44 atoms. So we used the position constraint. It fixes the positions of the specified atoms to their initial values. Typical example is: `%block GeometryConstraints`

```
cellside    c
cellangle   alpha  beta  gamma
position    from -1 to -10
position    4 5 6
rigid       1 2
%endblock GeometryConstraints
```

Lines may be up to 130 characters long. Ranges of atoms in a line may contain up to 1000 atoms. All names must be in lower case. The list of atoms for a given constraint may contain several atoms (as in lines 4 and 5) or a range (as in the third line), but not both.

- **Geometry Relaxation:** The molecular dynamics type of run has to be conjugate gradient to obtain the relaxed structure of the system. So `MD.TypeOfRun` should be added and set to `CG` because the default is set to `Verlet` for more than one-atom systems. Along with type of run other parameters which are changed are the number of `CG` steps, maximum force tolerance etc.
- **PAO.Basis:** Since we included the semi-core electrons in the simulation we had to specify the `PAO.Basis` (pseudo atomic orbital (PAO) basis) in the FDF file. Default values of `rc` are taken if they are set to 0. The format is also important. The orbitals should be specified in the increasing values of l quantum number and then n quantum number if there are more than one n values for one l value. The tutorial has a method to find the optimum values for the cut-off radius (r_c) of orbitals by plotting the **Final Total Energy** of single atom for different values of r_c .
- **PAO.EnergyShift:** A standard for orbital-confining cutoff radii. It is the excitation energy of the PAO's due to the confinement to a finite-range. It offers a general procedure for defining the confining radii of the original *first - zeta* PAO's for all the species guaranteeing the compensation of the basis. It has effect when the block `PAO.Basis` is not present or when the radii specified in that block are zero for the first zeta. It should be noted that `PAO.EnergyShift` has to be positive (Default value: 0.02 Ry).
- **Mesh Cut-off:** Parameter defining the density of the real-space grids. The parameter is given as an energy E , which implicitly defines the grid spacing Δx from the equivalent plane wave cut-off component $k_c = \pi/\Delta x$ (note that there is no factor of 2 here) which is related to the energy as $E = \hbar^2 k_c^2 / 2m_e$, where m_e is the electron mass. A higher value (energy) of this parameter gives better accuracy but it requires more and more computation power because the mesh is

more and more finer. Making the `MeshCutoff` too small can lead to the eggbox effect. This effect can increase the number of steps required for relaxation. The block `EggboxRemove` can be used to handle this problem. Refer to the manual for more details about this block.

- `ElectronicTemperature`: The electron temperature, T that enters in the Fermi distribution

$$f(E) = \frac{1}{e^{(E-E_f)/k_B T} + 1}, \quad (16)$$

where E_f is the Fermi energy, and k_B is the Boltzmann constant. For molecules with a very small HOMO-LUMO gap, the convergence rate of the self-consistent loop can usually be improved by increasing the electron temperature to smooth the Fermi distribution. Also metals (and in particular semi-metals) can sometimes be hard to converge at a low electron temperature, if there are band edges close to the Fermi level. In such cases, it is often possible to use a smaller k-point sampling if the the electron temperature is increased. The electron temperature has nothing to do with the lattice temperature or phonons, but is strictly related to the electron distribution function. The default value is 300 Kelvin.

- `Denchar`: The program `Denchar` calculates charge densities and/or electronic wavefunctions in real space of 3D grid points, from the output generated by SIESTA. For spin-unpolarized calculations, the fully self-consistent charge density and the difference between the self-consistent field (SCF) charge density and the superposition of atomic densities are calculated. In this way, we can study how the chemical bonds change the charge distribution. To run the program the first thing we must do is to run SIESTA for the system we are interested in, setting up variable `WriteDenchar` to `true`. In this way SIESTA will generate two files called `SystemLabel.PLD` and `SystemLabel.DIM` where information needed to plot the charge density and/or wavefunctions in real space is dumped. We

also need to have the file `ChemicalSpecies.ion` that contains the information about the basis set for each species in our system. Besides these files, we will need the density matrix file, `SystemLabel.DM` to plot the charge density and the file `SystemLabel.WFS` to plot the wavefunctions. Finally, we need to define the number of grid points and the three spanning vectors in the real space. The program is run separately using the command `denchar <SystemLabel.fdf>` and the output is printed in a standard Gaussian Cube format file, that is visualized using the package *Xcrysden*.

2.2.4 Generation of the pseudopotential

The atomic pseudopotentials are stored either in binary files (`ChemicalSpeciesLabel.vps`) or in ASCII files (`ChemicalSpeciesLabel.psf`), and are read at the beginning of the execution for each species defined in the input file. These files are generated by the ATOM program. It is included in `siesta/Pseudo/atom`. All pseudopotentials should be thoroughly tested before using them. We refer to the standard literature on pseudopotentials in ATOM manual `siesta/Pseudo/atom/atom.tex`. The program's basic capabilities are:

- All-electron DFT atomic calculations for arbitrary electronic configurations.
- Generation of *ab-initio* pseudopotentials (several flavors).
- Atomic calculations in which the effect of the core is represented by a previously generated pseudopotential. These are useful to make sure that the pseudopotential correctly reproduces the all-electron results for the valence complex.

Atom: The program ATOM has to be compiled and configured separately. Go to the `/siesta/Pseudo` directory and make appropriate changes to the `Makefile` for a different compiler and type `make` to install the program. The `Tutorial` directory has several examples that will help to test the program. Note: The program is very

sensitive to the format of the input file. There is a scale at the end of the file that will help to guide to enter the inputs. Make sure that the different input statements including the comment statements are according to the particular format.

Nb Pseudopotential: The Nb pseudopotential was generated using `tm2` method with 13 electrons in the core cell. The orbitals used were 4s, 4p, 4d and 4f. The corresponding cut-off radii were 0.97, 1.04, 1.42 and 1.42 Bohrs. Also the pseudopotential was non-relativistic and non-spin polarized.

2.3 Simulations and Results

The different structures of niobium nanowires, that were simulated using SIESTA are described in this section. Several numerical and experimental results showed consistent electronic properties of the smallest niobium contacts. Thus, we assumed the smallest stable structure i.e., a niobium dimer and started with a relatively simpler model of just two niobium atoms without any constraints. Then to test the effect of constraints, we placed two fixed atoms on either side of the dimer. Next we moved to our real system of having two semi-infinite electrodes with a hanging dimer. In each of the subsections, simultaneous comparison of the obtained results is also made with earlier published experimental and theoretical results.

2.3.1 Niobium dimer

We set our first simulation in SIESTA to obtain the relaxed structure of a simple niobium dimer. The initial position as shown in Fig. 2 was set to be plus and minus 1.00 Å for the two atoms of the dimer. We did not put any geometry constraints on any of the atoms and thus allowing them to move freely with each iteration to minimize the energy and the force between the atoms. However, the iterations were constrained by the tolerance levels. We set the tolerance level for density matrix by defining the `DM.Tolerance` to be 10^{-4} and for force to be 0.01 eV/Å. Also, if the simulation is not converging we set the upper limit for maximum allowed number of

self consistent field iterations and force iterations. The upper limit for self consistent field iterations `MaxSCFIterations` was set equal to 100 and the force iterations were bounded by setting `MD.NumCGsteps` (Molecular Dynamics - Number of Conjugate Gradient Steps) equal to 50. Since we want to obtain the relaxed structure we used the Conjugate Gradient (CG) for the `MD.TypeofRun` (Molecular Dynamics Type of Run). We also fix the maximum displacement for each conjugate gradient step to be 0.1 Å. We choose the `PA0.Basis` to be double zeta polarized and the electronic temperature set to 50 meV. The orbital confining cutoff radii were chosen by setting `PA0.EnergyShift` equal to 150 meV. `MeshCutoff` was chosen 200 Ry to be balanced between the computational power and accuracy.

The simulation converged at the relaxed distance between niobium atoms at 2.13 Å (Fig. 2). It took four conjugate gradient steps in approximately 750 seconds to minimize the force to 0.001322 eV/Å. The earlier results have reported a relaxed distance as 2.117 Å for the singlet state of niobium dimer [23]. Further we also analyzed the binding energy of the dimer. We ran the program explicitly for single niobium atom and doubled the total energy. The difference of the total energy obtained from single atoms simulation and dimer simulation was taken as the binding energy since all other parameters were kept constant. Our simulations gave the total energy of single atoms to be -1526.12 eV and the total energy of dimer was -3062.15 eV. These numbers give us a binding energy as 9.91 eV for the dimer or 4.955 eV for each atom. The reported binding energy is between 4 eV to 6 eV depending on the configuration of the dimer as singlet or triplet state [23]. Also, Delta RHO and RHO is plotted in Fig. 3 to support the dimerization. In conclusion, we verified that our simulations give satisfactory results for the dimer.

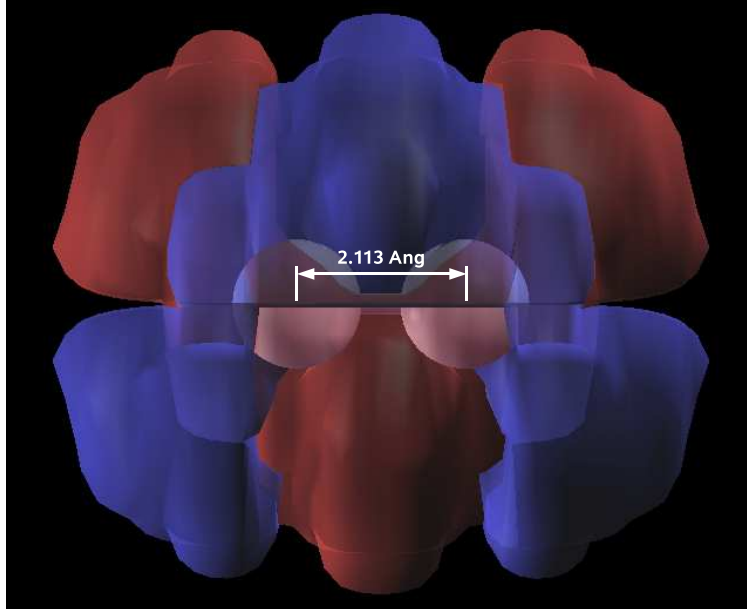


Figure 2: Final relaxed distance between the niobium dimer atoms is 2.113 \AA . The resulting wavefunction is also plotted at grid isovalue, -10^{-4} rendered both negative and positive values.

2.3.2 Niobium dimer between two niobium atoms

The next simulation was run for a niobium dimer hanging between two other niobium atoms. We set the initial the coordinates of the niobium dimer atoms such that the distance, ‘ d ’, between the dimer atoms is 1.65 \AA , and the positions of each of the two outermost atoms is fixed at distances, $a = a' = 3.16 \text{ \AA}$ away from the respective dimer atoms (Fig. 4). A new block `GeometryConstraints`, defined in previous section, was used to fix the positions of outer atoms. Also, we choose these positions such that the interatomic separation is greater then the dimer distance, and thus we biased the simulation to dimerize the atoms in the middle instead of forming two separate dimers. Most of the other parameters were kept similar, but to converge the simulations we changed the `PAO.EnergyShift` equal to 20 meV , the `PAO.Basis` was set to `DoubleZeta` and the `DM.Tolerance` to be 10^{-3} . Some other parameters were also changed during the trial and error part to make the program converge, but they will not change the output significantly.

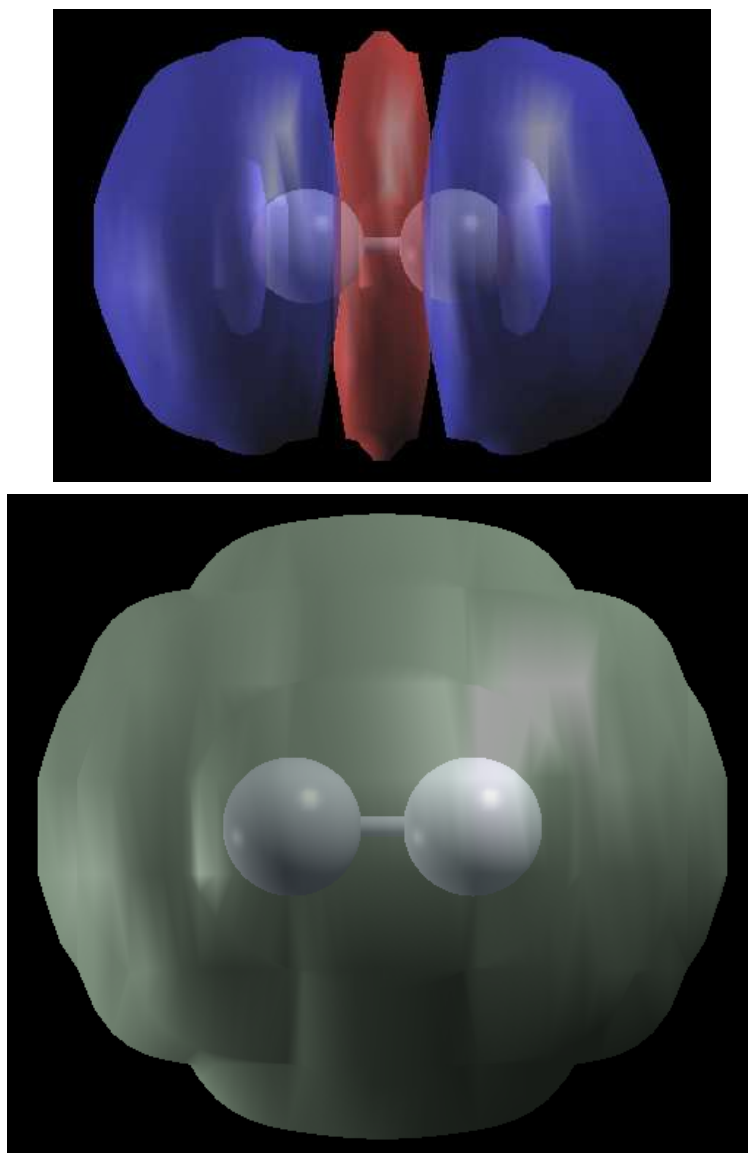


Figure 3: Delta RHO (Top) is plotted at grid isovalue, 5×10^{-4} rendered both negative and positive values and Valence pseudocharge density. RHO (Bottom) is plotted at grid isovalue, 10^{-3} rendered for positive values only.

After 51 conjugate gradient interaction steps the program converged and gave the final relaxed coordinates. Fig. 4 shows the wavefunction along with the final relaxed structure. The final relaxed positions were $a = 2.91 \text{ \AA}$, $d = 2.19 \text{ \AA}$, and $a' = 2.87 \text{ \AA}$. The results show that we started with the the initial position where the dimer atoms were closer than the relaxed state atoms. Also, it was seen in test simulations that if we start with the atoms placed at the positions separated by lattice constants, the relaxed state can result in two dimers. All these decisions to choose the initial coordinates can be justified by the limitation of SIESTA that we have to start with initial conditions that are close the final expected state. On comparison of the initial and final coordinates, we see that simulations in SIESTA changed the coordinates upto 0.5 \AA . Fig. 5 displays the RHO, the valence pseudocharge density at the mesh used by `dhscf.f`, (which calculates the self-consistent field contributions to Hamiltonian matrix elements, total energy, and atomic forces); and the Fig. 6 plots DRHO, i.e. the valence pseudocharge density minus the sum of atomic valence pseudocharge densities of the relaxed system. The maximum force for these positions was 0.08 eV/\AA . There are no previous data to verify these results. However, we can justify the distances using the fact that the outer fixed atoms try to pull the dimer atoms in the middle. This increases the bond distance between the dimer atoms. Also, a bulky lattice of niobium atoms is absent, so it was difficult to obtain a relaxed state of free dimer. We consider the complete lattice in the remaining part of the chapter.

2.3.3 Niobium dimer between two niobium electrodes

Finally, we moved to a more realistic situation of having two semi-infinite electrodes with the niobium dimer hanging between the two tips of the electrodes. We analyzed three different situations for the dimer. The first was to set the dimer exactly in the center of the two tips, which we called the symmetric position. The next position

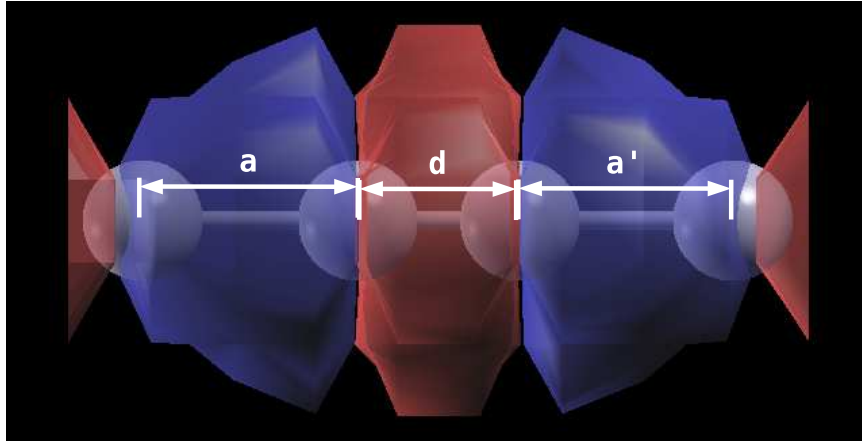


Figure 4: Wave function is plotted at grid isovalue, 10^{-3} rendered for both positive and negative values. The distances between different atoms are displayed by the arrows. Initial distances were $a = a' = 3.16 \text{ \AA}$ and $d = 1.65 \text{ \AA}$ whereas the final relaxed positions were $a = 2.91 \text{ \AA}$, $d = 2.19 \text{ \AA}$, and $a' = 2.87 \text{ \AA}$.

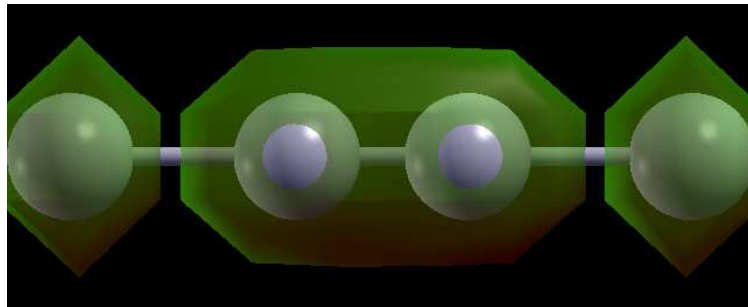


Figure 5: Valence pseudocharge density (RHO) is plotted at grid isovalue, 1.0 rendered for positive values.

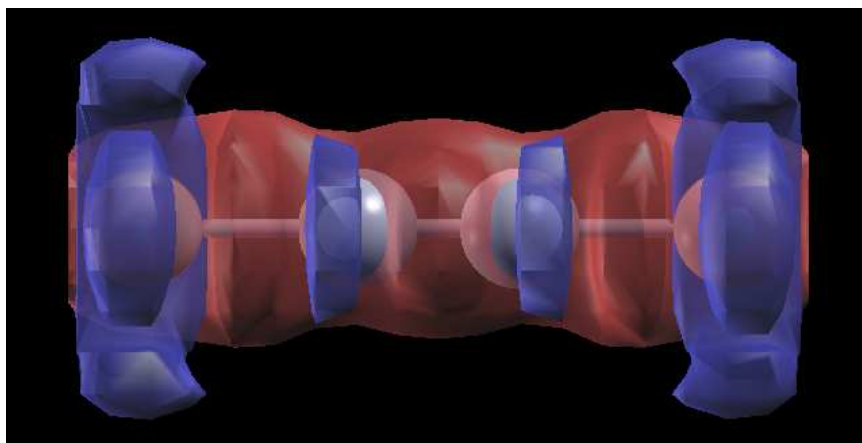


Figure 6: Bottom: Delta RHO is plotted at grid isovalue, 10^{-2} rendered for both positive and negative values.

was to displace the dimer slightly towards one of the electrode and we referred this one as the asymmetric position. Finally, we tilted the dimer and obtained the relaxed structure. This setup was referred to as the tilted positions. In each of the three cases we used 21 atoms for each electrode. We set the positions of each atoms according to the niobium lattice. The lattice was chosen so that electrode form a tip on one end and regular bulk at the other end. The atom of the tip was allowed to move with respect to each iteration, whereas the rest of the atoms in the electrode were fixed using the geometry constraint block. Most parameters were same as the previous case except `DM.MixingWeight` was set to 0.05 and `DM.NumberPulay` was set to 50 to speed up the convergence process. In the next paragraphs we will explain each of these structures in more details.

Symmetric Dimer: We started with the dimer placed symmetrically between the electrode. Only the tip atoms of the electrode and the dimer atoms were allowed to move. The geometry constraint block fixed the remaining 40 atoms during the simulation. The resulting structure is shown in Fig. 7. The initial distances between the electrode and dimer atoms were $a = a' = 2.78 \text{ \AA}$ and $d = 2.05 \text{ \AA}$. These values were taken from the earlier published results and so we were expecting our relaxed distances close to the initial values. The simulation did not change the coordinates significantly except that the tip atoms were pulled inside by the electrodes and the dimer distance increased by 2%. The final coordinates relaxed to $a = a' = 3.00 \text{ \AA}$, $d = 2.09 \text{ \AA}$. These changes can be considered small, and thus the results are in agreement with the distances reported in Ref. [3]. Fig. 7 displays the grid isovalue for the valence pseudocharge density, RHO . It shows that the pseudocharge density between the dimer and the electrode tips is reduced indicating a free dimer with no significant chemical bonding with the electrodes. Further, Fig. 8 displays the change in pseudocharge density DRHO which implies that during the simulation the pseudocharge density for the valence shell has significantly increased between the

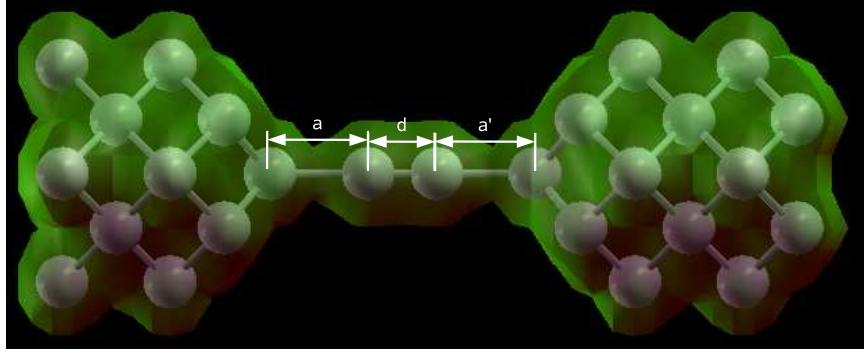


Figure 7: Symmetric niobium Dimer between two niobium electrodes with valence pseudo charge density, RHO plotted for grid isovalue 10^{-1} rendered for positive values only. The initial distances were $a = a' = 2.78 \text{ \AA}$ and $d = 2.05 \text{ \AA}$, and the final relaxed distances were $a = a' = 3.00 \text{ \AA}$ and $d = 2.09 \text{ \AA}$.

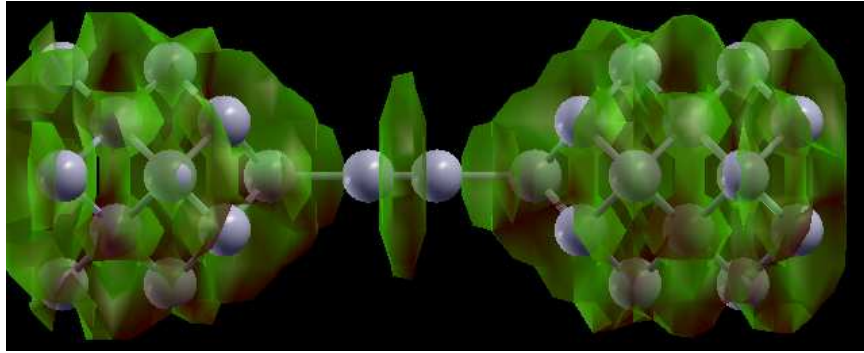


Figure 8: Symmetric niobium Dimer between two niobium electrodes with DRHO plotted for isovalue 10^{-4} rendered for positive values only.

dimer atoms. However, it is to be noted that the isovalues has been chosen such that they magnify the results making them easy to compare. These results prove the expected dimerization process.

Asymmetric Dimer: In case of asymmetric dimer, we increased the inter-electrode distance to 9.2 \AA and displaced the dimer to one side by 1.05 \AA so that the coordinates of the dimer were at distances 1.55 \AA and 0.5 \AA from the origin. As shown in Fig. 9, we placed the atoms with $a = 3.05 \text{ \AA}$, $d = 2.05 \text{ \AA}$, and $a' = 3.55 \text{ \AA}$. The final coordinates relaxed to $a = 3.01 \text{ \AA}$, $d = 2.09 \text{ \AA}$, and $a' = 3.55 \text{ \AA}$. So, the result we obtained is an asymmetric dimer and it is comparable to earlier results [3]. However, we could not obtain a relaxed structure at the electrode distance of

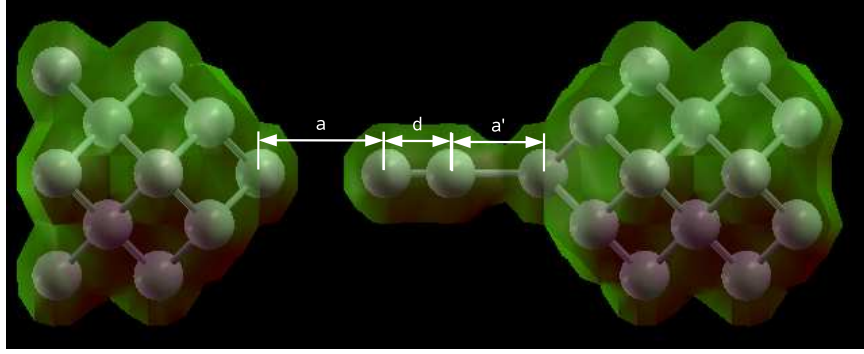


Figure 9: Asymmetric niobium dimer between two niobium electrodes with RHO plotted for grid isovalue 10^{-1} rendered for positive values only. The initial distances were $a = 3.05 \text{ \AA}$, $d = 2.05 \text{ \AA}$ and $a' = 3.55 \text{ \AA}$; and the final relaxed distances were $a = 3.01 \text{ \AA}$, $d = 2.09 \text{ \AA}$, and $a' = 3.55 \text{ \AA}$.

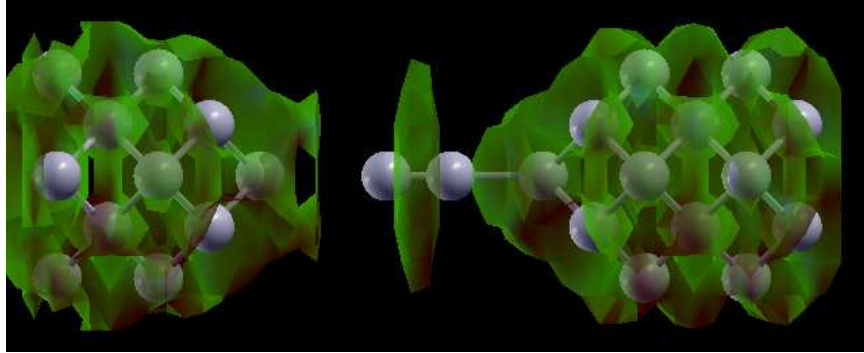


Figure 10: Asymmetric niobium dimer between two niobium electrodes with DRHO plotted for grid isovalue 10^{-5} rendered for positive values only.

8.5 \AA . Similar to the symmetric structure case we obtained figures for the valence pseudocharge density, RHO (Fig. 9) and change in pseudocharge density, DRHO (Fig. 10) which proves the dimerization.

Tilted Dimer: We studied this structure in more detail. We started by reducing the distance between the two electrodes, and then changed the initial rotation angle of the dimer axis from 90° to 110° in five different steps of 90° , 94° , 97° , 100° , and 110° degrees. The dimer stayed in its original position for the 90° . However, for all other angles except the 110° , we obtained the relaxed angle of 99° between the dimer axis and the line connecting the tip of the two electrodes. We obtained the relaxed structure for 6.50 \AA , 6.63 \AA and 6.8 \AA ; and we observed that the change in distance

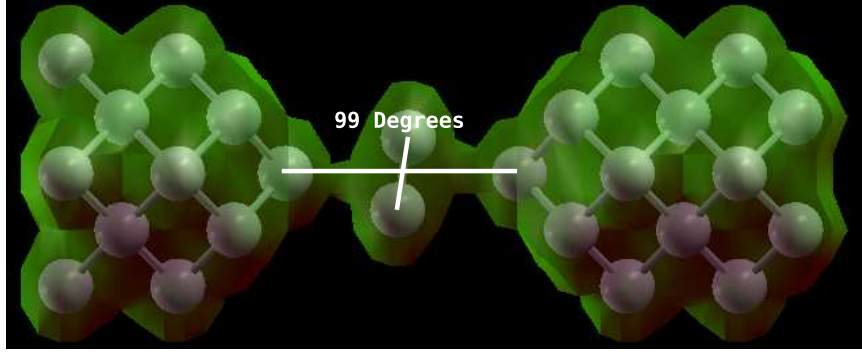


Figure 11: The initial angle was 97° while the relaxed final angle between the dimer axis and the axis connecting the two niobium electrodes was 99° . The valence pseudocharge density, RHO, is plotted for grid isovalue 10^{-1} rendered for positive values only.

between the electrodes did not change the angle of rotation significantly. Finally, for 110° , the simulation did not converge. Fig. 11 displays the final angle between the dimer axis and the line connecting the two niobium electrodes with the RHO density isosurface. Fig. 12 displays the final distances of tilted dimer between two niobium electrodes with delta RHO density isosurface rendered for both the negative and positive values.

The results obtained from SIESTA are not in close agreement with the earlier published results. While Marchenkov et al. [3], have shown that the tilted dimer should make an angle of 94° with the electrodes, we have obtained 99° . Another notable difference is the relaxed distance between the tip atoms of the electrodes. Our results give a tip to tip distance between 6.8 \AA and 6.9 \AA as compared to 6.63 \AA published earlier. The differences can be attributed to the difference in method of calculations. The previous results have been calculated using plane-wave basis whereas we have used a basis set that resembles the system wavefunctions.

In conclusion, we can say that we verified the earlier published results using SIESTA. One of the major problems with SIESTA is that the simulations may never converge. But given this disadvantage, we simulated all the results on a desktop computer using a single processor. All the results are obtained in comparatively less

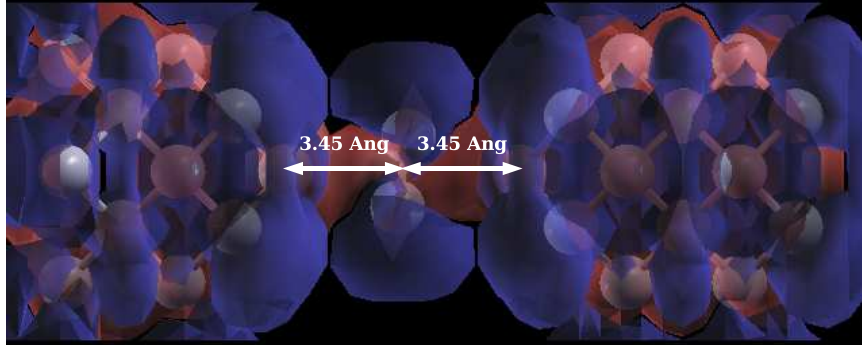


Figure 12: Final positions of tilted dimer between two niobium Electrodes with DRHO plotted for grid isovalue 10^{-3} rendered for both positive and negative values.

time then the ones obtained using plane-wave basis. A previous intuition of the final relaxed structure was definitely helpful for our case. Several times we have observed that some atom may start moving in some arbitrary direction and still the simulation converged. So we obtained some other relaxed state in which we may not be interested. However, in our simulations, we had previous knowledge of the relaxed state, thus we were able to verify the results successfully. Once we had the required structure, we deal with the transport properties in the next chapter.

CHAPTER III

ELECTRON TRANSPORT IN NANOWIRES

The theoretical description of quantum electron transport through molecular systems is a complex many-body problem similar to that of the electronic structure calculation. The study of electron transport became unavoidable when the advances in the semiconductor technology made it possible to fabricate conductors so small that the quantum nature of electrons could be observed directly in transport experiments. These semiconductor structures are characterized as mesoscopic systems (the lengthscales are of the order of $1 \mu\text{m}$), intermediate between the microscopic and macroscopic scales. So to study the variety of transport calculation problems, diverse approaches, ranging from exact many particle problem treatment within some simplified model for the system to semi-empirical models for transport through quite realistic structures consisting of hundreds of atoms, were developed. Here we will focus mainly on realistic systems such that we include the atomic descriptions of both the molecular system and the metal electrodes. Among the different available methods we use the *ab initio* method, often known as first principle calculations that start from the geometry of the system, then transport properties can be calculated using the Green's functions and the DFT used in the previous chapter. Although the results depend on the degree of approximations used, the main advantage of the *ab initio* method is that the obtained results are free from any empirical estimations and expectations needed in other methods. Moreover, the approximations used in the numerical methods can be improved on, and thus the convergence can be checked. In this chapter a general method for describing quantum electron transport will be introduced. We demonstrate how the transport formalism can be combined with

standard electronic structure methods to provide a first-principles description of electron transport in atomic-scale systems. The method is based on the non-equilibrium Green's function (NEGF) formalism of Keldysh [24] and Kadanoff and Baym [25], and originally was used to study transport in mesoscopic systems.

The chapter starts with an introduction of three important length scales that are used to characterize electron transport in the quantum regime. Further, the general transport formalism is introduced and an expression for the current through a quantum constriction is derived under fairly general conditions. For non-interacting electrons the obtained formula is shown to reduce to the well-known Landauer formula. A brief discussion of the NEGF method describing transport through a single energy level is presented to give the background of the package *Atomistix*, which was used for calculating the transport properties. A more comprehensive account of the theory presented in this chapter can be found in Refs. [26, 27, 28]. We also describe important parameters used in *Atomistix* to run the simulation on a desktop computer. Finally, we compare the transport properties of niobium nanowire with the results published by Marchenkov et. al.

3.1 Length Scales

Electrical conductance, relating the current through a conductor to the applied voltage $G = I(V)/V$, is a key quantity in the description of electron transport. For a macroscopic sample the classical conductance is given by

$$G = \sigma \frac{A}{L}, \quad (17)$$

where A and L are the cross-sectional area and the length of the sample, respectively, and σ is the material-dependent conductivity whose inverse is also known as resistivity. When the dimensions of the sample become comparable to the de Broglie wavelength of the particles, the quantum nature of the charge carriers becomes important, and the classical relation, Eq. (17), breaks down. Next, we introduce the

three length scales; Fermi wavelength, phase coherence length, and mean free path. These scales are important in the microscopic description of electron transport.

Fermi wavelength: The wave function of an electron in a crystalline metal contains a Bloch factor, $\exp(i\mathbf{k}\mathbf{r})$, that determines the complex phase of the wave function throughout the crystal [4]. The wavelength of this oscillating phase associated with a conduction electron at the Fermi level is called the Fermi wavelength, $\lambda_F = 2\pi/k_F$. In metals the Fermi wavelength is of the order of the lattice spacing, i.e., a few Å; while in semiconductors where the density of conduction electrons is very low, the Fermi wavelength can be tens of nanometers. These numbers give an estimate of the limiting length of a quasi one-dimensional quantum wire.

Phase coherence length: Physically, the phase coherence length, l_ϕ , defines the length scale on which the electron's wavefunction retains information about the initial phase; i.e., the distance a conduction electron moves before its phase is lost, i.e., $l_\phi = v_F\tau_\phi$, where v_F is the Fermi velocity. Therefore quantum interference can be observed on this length scale. Here, τ_ϕ , is the phase coherence time during which the phase of an electron is completely lost due to inelastic interactions with the dynamic environment of phonons, magnetic impurities, and other conduction electrons. However, static scatterers such as lattice defects, boundaries, or impurities do not destroy the electronic phase.

The decoherence can be illustrated by considering an electron in the two possible states $|a\rangle$ and $|b\rangle$. During the time τ_ϕ the electron interacts with another system initially in a state $|0\rangle$, and the combined states evolve as: $|a\rangle \otimes |0\rangle \rightarrow |a\rangle \otimes |1\rangle$ and $|b\rangle \otimes |0\rangle \rightarrow |b\rangle \otimes |0\rangle$. The consequence is

$$(|a\rangle + e^{i\phi}|b\rangle) \otimes |0\rangle \rightarrow |a\rangle \otimes |1\rangle + e^{i\phi}|b\rangle \otimes |0\rangle \quad (18)$$

and the state of the electron thus evolves from the pure state $|a\rangle + e^{i\phi}|b\rangle$, to the mixed state $|a\rangle\langle a| + |b\rangle\langle b|$, in which the phase is completely lost. At low temperatures, external degrees of freedom are frozen out, and l_ϕ increases accordingly. A typical

phase coherence length for Au at $T = 1$ K is around $1\mu\text{m}$ [29].

Mean free path: The mean free path is defined as $l_m = v_F\tau_m$, where τ_m is the time it takes for a conduction electron to change its initial momentum through scattering events. However, these events can be elastic as well as inelastic, so τ_m is not related to τ_ϕ . In a perfect crystal, the electron moves unhindered, and thus $\tau_m = \infty$ whereas in a real system, the presence of scatterers will reduce τ_m to a finite value.

In combination with the characteristic system dimension, L , the relative sizes of the length scales introduced above define different transport regimes. The systems considered in the present work are assumed to be in the phase-coherent regime where $l_\phi > L$. Additionally, $l_m > L$ can be realized in high purity samples like atomic contacts [29] and carbon nanotubes [30]. Under these conditions electron transport is said to be ballistic, since the electrons can move unhindered through the system. However, the formation of a good contact is crucial; because in most molecular junctions, the electrons will scatter significantly at the interface between electrodes and molecule as well as inside the molecule itself. In this case, $l_\phi > L > l_m$ and the transport are called diffusive. The distance between atoms is comparable to λ_F in a metal, and therefore molecules coupled to metallic leads must take the full atomic structure into account. The section is concluded by stating the relevant relation of length scales that characterize the molecular contacts investigated in this work: $\lambda_F \simeq l_m < L < l_\phi$.

3.2 The Landauer Scattering Approach

If phase coherence length is greater than the dimension of the system, all the characteristic lengths of the device coherence is maintained over all distinct paths of the device. Then, the entire circuit itself acts as a quantum scatterer of coherent electrons from the input leads, which are considered to act as perfect reservoirs for electrons. Pursuing this concept further Landauer [31] proved that when the entire device region is quantum coherent, it is possible that the transport properties of the system may

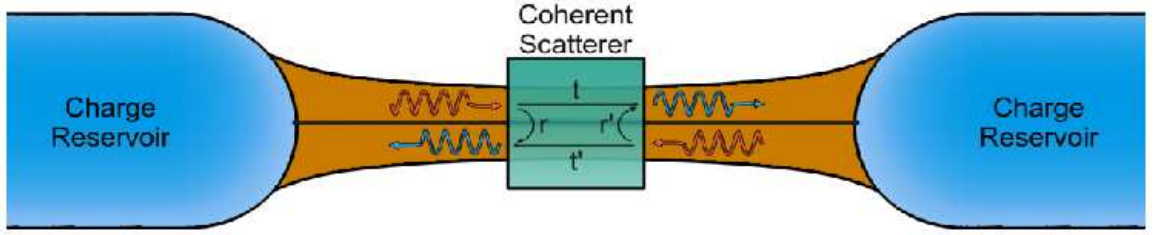


Figure 13: Scattering problem with charge reservoirs injecting electron waves into ideal leads that connect to the device region.

be obtained by using a scattering matrix approach. Moreover, he was able to show that the conductance of a quantum coherent circuit is quantized and depends on the transmission coefficients of the scattering matrix only.

The Scattering Matrix Formalism: Landauer considered the physical situation depicted in Fig. 13, where, charge reservoirs inject electron waves into ideal leads that connect to the device region, which is considered as a scattering center. The reservoirs absorb an incident electron perfectly without any backscattering and the leads are considered as electron waveguides that restrict the motion to only one dimension. This restriction quantizes the electronic states in the leads, which implies that only a finite number of modes are capable of propagating to and from the device region. Sharvin's conductance formula predicts semiclassically that this number is proportional to $k_F^2 A$, where A is the cross-sectional area of the conductor. With the physical picture in place, the scattering matrix approach can now be applied in order to solve for charge transport across a coherent device. To begin, we define the scattering matrix analogous to standard quantum mechanics textbooks [32]:

$$\mathbf{S} = \begin{pmatrix} s_{11} & s_{12} \\ s_{21} & s_{22} \end{pmatrix} = \begin{pmatrix} r & t' \\ t & r' \end{pmatrix}, \quad (19)$$

such that \mathbf{S} relates the incoming probability amplitudes, a_i , with the outgoing amplitudes, b_i , in the following fashion:

$$\begin{pmatrix} b_1 \\ b_2 \end{pmatrix} = \begin{pmatrix} \mathbf{r} & \mathbf{t}' \\ \mathbf{t} & \mathbf{r}' \end{pmatrix} \begin{pmatrix} a_1 \\ a_2 \end{pmatrix}. \quad (20)$$

In general \mathbf{s}_{ij} of the scattering matrix are matrices whose entries relate the probability of an incoming electron wave on mode i being scattered into mode j . Therefore, in general the a_i and b_i in the previous equation are vectors. Moreover, the diagonal terms in the scattering matrix refer to reflection of a wave on mode i into mode j on the same lead, whereas the off diagonal terms relate the transmission of electron waves. Additionally, to ensure particle number conservation, the scattering matrix must be unitary, i.e., $\mathbf{S}\mathbf{S}^\dagger=\mathbf{I}$. This implies that the scattering matrix must have an inverse and thus the matrix is diagonalizable. Further, the decomposition of the scattering matrix into individual, non-interacting modes is unique up to permutations [33]. So, an incoming electron wave on mode i is either transmitted onto mode i of the other lead or is reflected back into mode i of the original lead in the newly diagonalized basis. These diagonalized modes of the system that have been decoupled from one another are also referred to as conduction channels. Hence, the problem of calculating the transport properties for an entire system has been reduced to summing contributions from independent channels. Further, in transport theory, the calculation of the conductance of a device adds practical importance to Landauer formalism.

Single Channel Conductance: The problem of calculating the conductance of a device has been simplified to the conductance of single channel that can be solved by calculating the current through a quantum scatterer. Therefore we introduce the creation and annihilation operators for electron waves on mode m of lead α in the following way: the energy dependent creation and annihilation operators for *incoming* electron waves are $a_{m\alpha}^\dagger(\epsilon)$ and $a_{m\alpha}(\epsilon)$, respectively. Similarly $b_{m\alpha}^\dagger(\epsilon)$ and

$b_{m\alpha}(\epsilon)$ refer to the creation and annihilation operators for *outgoing* electrons. Using these definitions it can be shown that the current due to mode m on lead α is given by the expression [34]:

$$I_{m\alpha} = \int_{-\infty}^{\infty} d\epsilon (\langle a_{m\alpha}^\dagger(\epsilon) a_{m\alpha}(\epsilon) \rangle - \langle b_{m\alpha}^\dagger(\epsilon) b_{m\alpha}(\epsilon) \rangle). \quad (21)$$

Clearly, a net current is caused by an imbalance in the population of incoming and outgoing electrons from the device; however it can be simplified using the scattering matrix, which relates the incoming and outgoing electrons. Using the relation:

$$b_{m\alpha} = \sum_{n\beta} (\mathbf{s}_{\alpha\beta})_{mn} a_{n\beta}, \quad (22)$$

and also the fact that the Fermi distribution of the reservoir imposes the condition:

$$\langle a_{m\alpha}^\dagger(\epsilon) a_{m\alpha}(\epsilon) \rangle = \delta_{mn} \delta_{\alpha\beta} f_\alpha(\epsilon), \quad (23)$$

the equation for the current in lead 1 (summed over all modes) can be rewritten as:

$$I_1 = \frac{2e}{h} \int_{-\infty}^{\infty} d\epsilon (f_1(\epsilon) - f_2(\epsilon + eV)) \text{Tr}(t^\dagger t). \quad (24)$$

Also at the limiting case of small voltages ($V \ll E_F$) and at $T = 0K$, the integral will evaluate to $eV \cdot \text{Tr}(t^\dagger t)$ and the current can be rewritten as:

$$I_1 = \frac{2e^2}{h} \text{Tr}(t^\dagger t) V. \quad (25)$$

The above equation gives the expression for conductance as::

$$G = \frac{2e^2}{h} \text{Tr}(t^\dagger t) = G_0 \cdot \text{Tr}(t^\dagger t), \quad (26)$$

$$G_0 \approx 77\mu S \approx \frac{1}{12.9k\Omega}. \quad (27)$$

Here it should be noted that the expression for conductance is in terms of fundamental constants and scattering matrix parameters only. The fundamental constants combine

to form the quantum of conductance, G_0 . From this expression, the total conductance of the device is then given by a sum over all conductance channels:

$$G_{tot} = \sum_i G_i = G_0 \sum_i \tau_i, \quad (28)$$

where τ_i is termed the transmission coefficient of channel i and is given by, $\tau_i = \text{Tr}(t_i^\dagger t_i)$. Since we know that the decomposition of the scattering matrix into individual conduction channels is unique (up to a permutation), any transport quantity of a mesoscopic coherent device can be given in terms of the transmission coefficients of its conduction channels. These sets of transmission coefficients are also known as the mesoscopic PIN code of that device. However, though the effect can be predicted using first principles arguments, some outstanding questions still remain. For instance, if we let $\tau = 1$ (i.e., a ballistic point contact), this implies that all electrons incident on the scattering center are transmitted with a probability of one, why would the channel still have a finite conductance? One would naively suspect that for a ballistic channel the conductance should approach infinity since there are no scattering centers to impede the transmission of electrons. The answer to this question is subtle and lies in the fact that the distribution of states in the leads is not a Fermi distribution [35]; hence there is a finite conductance of a ballistic contact even if $\tau = 1$.

3.3 Non-equilibrium Green's Function technique [27]

Turning back to the picture introduced in the Landauer formulation of quantum currents, we introduce an alternative/complimentary description to DFT of the metal-molecule-metal system, which is known as non-equilibrium Green's function (NEGF) method. Besides calculating the expressions for current and charge densities in nanoscale (both molecular, metallic, and semiconductor) conductors under bias, we give some intuitive explanations of one particle Green's functions in a compact form together with derivations of the expressions for the current and the density matrix. Starting with the introduction of Green's function, we develop formalism for the self

energies of the leads. With these definitions in place, we calculate the expression for current and transmission spectrum.

Green's Function: In the discrete Schrödinger equation, $H|n\rangle = E|n\rangle$, we divide the Hamiltonian H and wavefunction $|n\rangle$ of the system into contact ($H_{1,2}, |\psi_{1,2}\rangle$) and device ($H_d, |\psi_d\rangle$) subspaces:

$$\begin{pmatrix} H_1 & \tau_1 & 0 \\ \tau_1^\dagger & H_d & \tau_2^\dagger \\ 0 & \tau_2 & H_2 \end{pmatrix} \begin{pmatrix} |\psi_1\rangle \\ |\psi_d\rangle \\ |\psi_2\rangle \end{pmatrix} = E \begin{pmatrix} |\psi_1\rangle \\ |\psi_d\rangle \\ |\psi_2\rangle \end{pmatrix}, \quad (29)$$

where $\tau_{1,2}$ describes the interaction between device and contacts. In general we have N contacts ($H_{1,\dots,N}$) connecting ($\tau_{1,\dots,N}$) the device H_d to the reservoirs. It is also assumed that the contacts are independent, i.e., there are no cross terms (τ) between the different contacts. Now the Green's function, $G(E)$ can be defined as:

$$(E - H)G(E) = I. \quad (30)$$

The reason for calculating the Green's function is that it is easier than solving the Schrödinger equation. Moreover, the Green's function gives the response of a system to a constant perturbation, $|v\rangle$ in the perturbed Schrödinger equation:

$$H|\psi\rangle + |v\rangle = E|\psi\rangle. \quad (31)$$

The response to this perturbation is given by:

$$\begin{aligned} (E - H)|\psi\rangle &= -|v\rangle \\ |\psi\rangle &= -G(E)|v\rangle. \end{aligned} \quad (32)$$

Notation: In this text we will denote the retarded Green's function with G or G^R and the advanced with G^\dagger or sometimes with G^A . Additionally, capital G denotes the full Green's function, and its sub-matrices are denoted by G_1, G_d, G_{1d} etc. Lowercase is used for the Green's functions of the isolated subsystems, e.g., $(E - H_2)g_2 = I$. Also, note that the retarded Green's function of the isolated contact (g_2), gives the

solution corresponding to an outgoing wave in the contact and the advanced Green's function, (g_2^\dagger) , gives the solution corresponding to an incoming wave.

Self Energies: The Green's function of the device (G_d) can be calculated separately without calculating the whole Green's function (G). We start from the definition of the Green's function and obtain:

$$\begin{pmatrix} E - H_1 & -\tau_1 & 0 \\ -\tau_1^\dagger & E - H_d & -\tau_2^\dagger \\ 0 & -\tau_2 & E - H_2 \end{pmatrix} \begin{pmatrix} G_1 & G_{1d} & G_{12} \\ G_{d1} & G_d & G_{d2} \\ G_{21} & G_{2d} & G_2 \end{pmatrix} = \begin{pmatrix} I & 0 & 0 \\ 0 & I & 0 \\ 0 & 0 & I \end{pmatrix} \quad (33)$$

Selecting the three equations in the second column:

$$\begin{aligned} (E - H_1)G_{1d} - \tau_1 G_d &= 0, \\ -\tau_1^\dagger G_{1d} + (E - H_d)G_d - \tau_2^\dagger G_{2d} &= I, \\ (E - H_2)G_{2d} - \tau_2 G_d &= 0. \end{aligned} \quad (34)$$

Solving the above set of equations, we obtain:

$$G_d = (E - H_d - \Sigma_1 - \Sigma_2)^{-1}, \quad (35)$$

where the expressions for $\Sigma_1 = \tau_1^\dagger g_1 \tau_1$ and $\Sigma_2 = \tau_2^\dagger g_2 \tau_2$ are the so called self-energies. The effect of the contacts on the device can be interpreted as the addition of the self-energies to the device Hamiltonian, since when we calculate the Green's function of the device, we just calculate the Green's function for the effective Hamiltonian $H_{effective} = H_d + \Sigma_1 + \Sigma_2$. However, this interpretation is valid during the calculation of the Green's function only, because the eigen-values and -vectors of this effective Hamiltonian are quantities that cannot be interpreted easily. Additionally, the Green's function gives the spectral function, $A = i(G - G^\dagger)$ that gives the density of states and all solutions to the Schrödinger equation. To prove this, we start with the two solutions $|\psi^R\rangle$ and $|\psi^A\rangle$ corresponding to advanced and retarded Green's functions for the Schrödinger Eq. (31) in presence of a perturbation $|v\rangle$:

$$|\psi\rangle^A = -G|v\rangle \quad (36)$$

$$|\psi\rangle^R = -G^\dagger|v\rangle. \quad (37)$$

Since the difference of these solutions $(|\psi\rangle^A - |\psi\rangle^R) = (G - G^\dagger)|v\rangle = -iA|v\rangle$ is a solution to the Schrödinger equation:

$$(E - H)(|\psi\rangle^A - |\psi\rangle^R) = (E - H)(G - G^\dagger)|v\rangle = (I - I)|v\rangle = 0, \quad (38)$$

we have $|\psi\rangle = A|v\rangle$, that is also a solution to the Schrödinger equation for any vector $|v\rangle$. Next we expand the Green's function in the eigenbasis to show that the spectral function actually gives all solutions to the Schrödinger equation:

$$G = \frac{1}{E - H} = \int_k \frac{|k\rangle\langle k|}{E + i\delta - \epsilon_k}, \quad (39)$$

where the δ is the small imaginary part, $|k\rangle$'s are all normalized eigenvectors to H with the corresponding eigenvalues ϵ_k . Expanding the spectral function in the eigenbasis gives:

$$A = i \left(\frac{1}{E + i\delta - H} - \frac{1}{E - i\delta - H} \right) \quad (40)$$

$$= i \int dk |k\rangle\langle k| \left(\frac{1}{E + i\delta - \epsilon_k} - \frac{1}{E - i\delta - \epsilon_k} \right) \quad (41)$$

$$= i \int dk |k\rangle\langle k| \left(\frac{2\delta}{(E - \epsilon_k)^2 + \delta^2} \right) \quad (42)$$

where δ is our infinitesimal imaginary part of the energy. In the limiting case when δ goes to zero we obtain:

$$A = 2\pi \int dk \delta(E - \epsilon_k) |k\rangle\langle k| \quad (43)$$

$$= 2\pi \text{DOS}(E) |k(E)\rangle\langle k(E)| \quad (44)$$

In the Eq. (42), since $\frac{2\delta}{(E - \epsilon_k)^2 + \delta^2}$ goes to zero everywhere except at $E = \epsilon_n$, the expression for A simplifies to integration of the delta function, $\delta(E - \epsilon_n)$ over E that gives the $2\pi\delta(E - \epsilon_n)$ factor along with the function $\text{DOS}(E)$ or density of states. Eq. (44) shows that the spectral function gives us all solutions to the Schrödinger equation.

The same method can be extrapolated to find all solutions to the Schrödinger equation of the isolated contact from its spectral function, a_i .

Transport Problem: After we have the expression for the self-energy of the individual contacts, we consider the transport problem by analyzing the response to the incoming wave. First, we note that in the non-equilibrium case reservoirs with different chemical potentials will inject electrons and occupy the states corresponding to incoming waves in the contacts. Therefore, to find the solutions corresponding to these incoming waves, we consider contact 1 isolated from the other contacts and the device. It should be noted that at a certain energy, we will have solutions corresponding to an incoming wave that is totally reflected at the end of the contact. These solutions are denoted with $|\psi_{1,n}\rangle$, where 1 is the contact number and n is a quantum number indicating that we may have several modes in the contacts. As shown earlier these solutions can be obtained from the spectral function a_1 of the isolated contact. To calculate the wavefunction on the whole system caused by the incoming wave in contact 1, we connect the contacts to the device. Also a wavefunction should be of the form $|\psi_{1,n}\rangle + |\psi^R\rangle$, where $|\psi_{1,n}\rangle$ is the totally reflected wave and $|\psi^R\rangle$ is the retarded response of the whole system. Putting in the ansatz $|\psi_{1,n}\rangle + |\psi^R\rangle$ into the Schrödinger equation (Eq. (29)) gives:

$$\begin{pmatrix} H_1 & \tau_1 & 0 \\ \tau_1^\dagger & H_d & \tau_2^\dagger \\ 0 & \tau_2 & H_2 \end{pmatrix} (|\psi_{1,n}\rangle + |\psi^R\rangle) = E(|\psi_{1,n}\rangle + |\psi^R\rangle) \quad (45)$$

$$\begin{pmatrix} E|\psi_{1,n}\rangle \\ \tau_1^\dagger|\psi_{1,n}\rangle \\ 0 \end{pmatrix} + \begin{pmatrix} H_1 & \tau_1 & 0 \\ \tau_1^\dagger & H_d & \tau_2^\dagger \\ 0 & \tau_2 & H_2 \end{pmatrix} |\psi^R\rangle = E(|\psi_{1,n}\rangle + |\psi^R\rangle) \quad (46)$$

$$H|\psi^R\rangle = E|\psi^R\rangle - \tau_1^\dagger|\psi_{1,n}\rangle. \quad (47)$$

It should be noted that in the above equation:

$$|\psi^R\rangle \equiv \begin{pmatrix} |\psi_1\rangle \\ |\psi_d\rangle \\ |\psi_2\rangle \end{pmatrix} \quad \text{and} \quad |\psi_{1,n}\rangle \equiv \begin{pmatrix} |\psi_{1,n}\rangle \\ 0 \\ 0 \end{pmatrix}. \quad (48)$$

Similar to Eq. (31), we see that $|\psi^R\rangle$ is nothing else but the response of the whole system to a perturbation of $-\tau_1^\dagger|\psi_{1,n}\rangle$,

$$|\psi^R\rangle = G\tau_1^\dagger|\psi_{1,n}\rangle. \quad (49)$$

Note that we have chosen the retarded response that means the part of the wave only that is traveling towards the device is the incoming wave. It will be useful to have the expressions for the device wavefunction ($|\psi_d\rangle$) and contact wavefunction ($|\psi_{1,2}\rangle$).

$$|\psi_d\rangle = G_d\tau_1^\dagger|\psi_{1,n}\rangle \quad (50)$$

$$|\psi_2\rangle = g_2\tau_2|\psi_d\rangle \quad (51)$$

$$= g_2\tau_2G_d\tau_1^\dagger|\psi_{1,n}\rangle. \quad (52)$$

To calculate the wavefunction in the contact containing the incoming wave (contact 1) we need to add the incoming wave:

$$|\psi_1\rangle = (1 + g_1\tau_1G_d\tau_1^\dagger)|\psi_{1,n}\rangle. \quad (53)$$

Knowing the wavefunctions corresponding to incoming waves in different contacts enables us to fill up the different solutions according to the electron reservoirs filling the contacts.

In the non-equilibrium case we are often interested in the charge density matrix ρ ,

$$\rho = \sum_k f(k, \mu) |\psi_k\rangle \langle \psi_k|, \quad (54)$$

where the sum runs over all states with the occupation number $f(E_k, \mu)$, which is determined by the reservoirs filling the incoming waves in the contacts.

$$f(E_k, \mu) = \frac{1}{1 + e^{(E_k - \mu)/k_B T}} \quad (55)$$

is the Fermi-Dirac function with the chemical potential μ_1 , and temperature (T) of the reservoir responsible for injecting the electrons into the contacts. Also the wavefunction on the device is given by an incoming wave in contact 1, which is given by expression in Eq. (51). Adding up all states from contact 1 gives:

$$\rho_d[\text{from contact 1}] = \int_{E=-\infty}^{\infty} dE \text{DOS}(E) f(E, \mu_1) |\psi_k\rangle \langle \psi_k| \quad (56)$$

$$= \int_{E=-\infty}^{\infty} dE f(E, \mu_1) \sum_k \text{DOS}(E) G_d \tau_1^\dagger |\psi_{1,k}\rangle \langle \psi_{1,k}| \tau_1 G_d^\dagger \quad (57)$$

$$= \int_{E=-\infty}^{\infty} dE f(E, \mu_1) G_d \tau_1^\dagger \left(\sum_k \text{DOS}(E) |\psi_{1,k}\rangle \langle \psi_{1,k}| \right) \tau_1 G_d^\dagger \quad (58)$$

$$= \int_{E=-\infty}^{\infty} dE f(E, \mu_1) G_d \tau_1^\dagger \frac{a_1}{2\pi} \tau_1 G_d^\dagger. \quad (59)$$

Introducing the new quantity $\Gamma_1 = \tau_1 a_1 \tau_1^\dagger = i(\Sigma_1 - \Sigma_1^\dagger)$, we obtain the simple formula:

$$\rho[\text{from contact 1}] = \frac{1}{2\pi} \int_{E=-\infty}^{\infty} dE f(E, \mu_1) G_d \Gamma_1 G_d^\dagger. \quad (60)$$

The total charge density thus becomes a sum over all contacts:

$$\rho = \frac{2(2 \text{ for spin})}{2\pi} \int_{E=-\infty}^{\infty} dE \sum_i f(E, \mu_i) G_d \Gamma_i G_d^\dagger. \quad (61)$$

Probability Current and Transmission: A current arises when there is a difference in chemical potentials in the reservoirs that are filling the contact device. This current can be calculated in a way similar to that used to calculate the charge density in the previous paragraph, i.e., we use the expression for wavefunction to obtain the physical quantity current. The reason for using a wavefunction is the not-so-clear velocity operator for a discrete Hamiltonian. In the continuum case, velocity is clearly defined and thus we can obtain nice expression. In our case we have to use the wavefunctions for the system to obtain the current that has a probability associated with it. Therefore, we use the definition of velocity analogous to the one in fluid mechanics and derive an expression for the current from the continuity equation using two contacts. Since in steady-state, the probability to find an electron

on the device is $\sum_i |\psi_i|^2$ (where the sum runs over the device subspace) is conserved, we have the following continuity equation:

$$0 = \frac{\delta \sum_i |\psi_i|^2}{\delta t} \quad (62)$$

$$= \sum_i \frac{\delta \langle \psi | i \rangle \langle i | \psi \rangle}{\delta t} \quad (63)$$

$$= \sum_i \left(\frac{\delta \langle \psi | i \rangle}{\delta t} \langle i | \psi \rangle + \langle \psi | i \rangle \frac{\delta \langle i | \psi \rangle}{\delta t} \right) \quad (64)$$

$$= \frac{i}{\hbar} \sum_i (\langle \psi | H | i \rangle \langle i | \psi \rangle - \langle \psi | i \rangle \langle i | H | \psi \rangle) \quad (65)$$

$$= \frac{i}{\hbar} \sum_i (\langle \psi | H | \psi_d \rangle - \langle \psi_d | H | \psi \rangle) \quad (66)$$

$$= \frac{i}{\hbar} \sum_i (\langle \psi | H_d + \tau_1 + \tau_2 | \psi_d \rangle - \langle \psi_d | H_d + \tau_1^\dagger + \tau_2^\dagger | \psi \rangle) \quad (67)$$

$$= \frac{i}{\hbar} \sum_i ([\langle \psi_1 | \tau_1 | \psi_d \rangle - \langle \psi_d | \tau_1^\dagger | \psi_1 \rangle] + [\langle \psi_2 | \tau_2 | \psi_d \rangle - \langle \psi_d | \tau_2^\dagger | \psi_2 \rangle]). \quad (68)$$

Using the previously derived results the in continuity equation, we obtain Eq. (68) in which the first term in the bracket represents the incoming probability current into the device from contact 1 and the one in second bracket from contact 2. Generalizing to an arbitrary contact i gives us the electric current (at one energy) as the charge (-e) times the probability current:

$$i_i = -\frac{ie}{\hbar} \left(\langle \psi_i | \tau_i | \psi_d \rangle - \langle \psi_d | \tau_i^\dagger | \psi_i \rangle \right). \quad (69)$$

Here, i_i is defined as positive for a current from the contacts into the device. The total current through the device can be calculated by putting in the wavefunction of the device and the contacts ($|\psi_d\rangle, |\psi_1\rangle, |\psi_2\rangle$) together and then adding all the contributions. Thus, the current into the device from a incoming wave of one energy

(E) in contact 1 ($|\psi_{1,n}\rangle$) through the coupling defined by τ_2 is:

$$i_{2 \text{ from } 1} = -\frac{ie}{\hbar} \left(\langle \psi_2 | \tau_2 | \psi_d \rangle - \langle \psi_d | \tau_2^\dagger | \psi_2 \rangle \right) \quad (70)$$

$$= -\frac{ie}{\hbar} \left(\langle \psi_{1,n} | \tau_1 G_d^\dagger \tau_2^\dagger g_2^\dagger \tau_2 G_d \tau_1^\dagger | \psi_{1,n} \rangle - \langle \psi_{1,n} | \tau_1 G_d^\dagger \tau_2^\dagger g_2 \tau_2 G_d \tau_1^\dagger | \psi_{1,n} \rangle \right) \quad (71)$$

$$= -\frac{ie}{\hbar} \langle \psi_{1,n} | \tau_1 G_d^\dagger \tau_2^\dagger (g_2^\dagger - g_2) \tau_2 G_d \tau_1^\dagger | \psi_{1,n} \rangle \quad (72)$$

$$= -\frac{e}{\hbar} \langle \psi_{1,n} | \tau_1 G_d^\dagger \Gamma_2 G_d \tau_1^\dagger | \psi_{1,n} \rangle. \quad (73)$$

Adding over the modes n and noting that the levels are filled from the reservoir connected to contact 1 gives (2 for spin):

$$I_{2 \text{ from } 1} = -2\frac{e}{\hbar} \int_{E=-\infty}^{\infty} dE f(E, \mu_1) \sum_n \text{DOS}(E) \langle \psi_{1,n} | \tau_1 G_d^\dagger \Gamma_2 G_d \tau_1^\dagger | \psi_{1,n} \rangle \quad (74)$$

$$= \frac{2e}{\hbar} \int_{E=-\infty}^{\infty} dE f(E, \mu_1) \sum_{m,n} \text{DOS}(E) \langle \psi_{1,n} | \tau_1 | m \rangle \langle m | G_d^\dagger \Gamma_2 G_d \tau_1^\dagger | \psi_{1,n} \rangle \quad (75)$$

$$= \frac{2e}{\hbar} \int_{E=-\infty}^{\infty} dE f(E, \mu_1) \sum_m \langle m | G_d^\dagger \Gamma_2 G_d \tau_1^\dagger \left(\sum_n \text{DOS}(E) | \psi_{1,n} \rangle \langle \psi_{1,n} | \right) \tau_1 | m \rangle \quad (76)$$

$$= \frac{2e}{\hbar} \int_{E=-\infty}^{\infty} dE f(E, \mu_1) \sum_m \langle m | G_d^\dagger \Gamma_2 G_d \tau_1^\dagger \frac{a_1}{2\pi} \tau_1 | m \rangle \quad (77)$$

$$= \frac{e}{\pi\hbar} \int_{E=-\infty}^{\infty} dE f(E, \mu_1) \text{Tr}(G_d^\dagger \Gamma_2 G_d \Gamma_1). \quad (78)$$

$$(79)$$

To get the total current through the device, the current from contact two has to be subtracted away:

$$I = \frac{e}{\pi\hbar} \int_{E=-\infty}^{\infty} dE (f(E, \mu_1) - f(E, \mu_2)) \text{Tr}(G_d^\dagger \Gamma_2 G_d \Gamma_1), \quad (80)$$

which is exactly the Landauer formula for the current (Eq. (24)).

3.4 *Atomistix Tool Kit*

Among the different available choices to *ab initio* electron transport simulation codes, we used the *Atomistix Tool Kit*, which was earlier known as TransSIESTA (transport

properties using SIESTA) [36, 37, 38, 39]. It is a program capable of modeling electrical properties of nanostructured systems coupled to semi-infinite electrodes (open system). For instance, the two electrodes could be metal crystals and the nanostructure could consist of molecules between the metal surfaces.

The NEGF techniques are combined with the DFT for the electronic structure calculations. The method is capable of modeling the electronic structure of geometries where periodic boundary conditions are employed in the x and y direction, while in the z direction the system is divided into three regions with two semi-infinite atomic systems (viewed as periodic crystals) coupled via a scattering region in the middle. Before the semi-infinite system calculation can start, a separate calculation of the bulk phase of the electrodes must be performed in order to obtain the bulk Hamiltonian parameters. This Hamiltonian is used for calculating the surface Green's function of the electrode. Next a computational supercell is defined that includes all atoms in the left electrode, scattering region and right electrode. The interaction range of the localized basis set determines the number of atoms needed to describe the electrode region. In the open system calculation, all Hamiltonian parameters within the supercell are calculated within a DFT self-consistent approach and passed to the NEGF subroutine. The Hamiltonian parameters of the electrode atoms are substituted with bulk Hamiltonian parameters and determine the non-equilibrium (NE) density matrix of the system by combining the supercell Hamiltonian with the remainder of the electrodes using the surface Green's functions. New Hamiltonian parameters are determined from the NE density, and the steps are repeated self-consistently.

To start the calculation, a starting guess for the potential in the scattering region is used, typically from a separate bulk calculation in the supercell region. When a bias voltage is applied the semi-infinite electrode systems have different electrochemical potentials, and a good starting point across the scattering region is to start from

the unbiased system potential. The Hamiltonian matrix is calculated from this starting guess using a localized basis set. This matrix is used to setup the NEGF of the system. In the next step the NE density matrix is calculated from the NEGF. The density matrix defines the effective potential in the scattering region and thereby new Hamiltonian parameters. The steps are repeated until a self-consistent solution is found. Once the self-consistent Hamiltonian is obtained, post-processing tools can be used to extract additional information. It is possible to calculate transmission coefficients within an energy window and separate transmission into eigenchannels. It also calculates the total current from transmission. Additionally, left or right propagating scattering states for a particular energy can be obtained and separated into eigenchannels. Eigenstates of projected self-consistent Hamiltonian are also accessible. Current-voltage characteristics can be obtained after successful calculation for a range of voltages.

Just like in SIESTA, all the parameters for the simulation can be defined in the script. However, the difference is that SIESTA uses FORTRAN whereas Atomistix uses Python programming language. Also, Atomistix is more sophisticated and has a graphical user interface Virtual Nano Lab (VNL). We installed the software Atomistix along with VNL and defined all our simulation parameters using VNL. The script (*.py file) is generated while using VNL and can be accessed any time for detailed information about the simulation parameters. Since Atomistix is based on an algorithm similar to that of SIESTA, most of the parameters defined in VNL are same as the parameters defined in SIESTA, and their details are given in previous chapter. Besides the common parameters there are some additional parameters in Atomistix because this software can handle the quantum transport simulations. Therefore, in this section we present an overview of these new parameters.

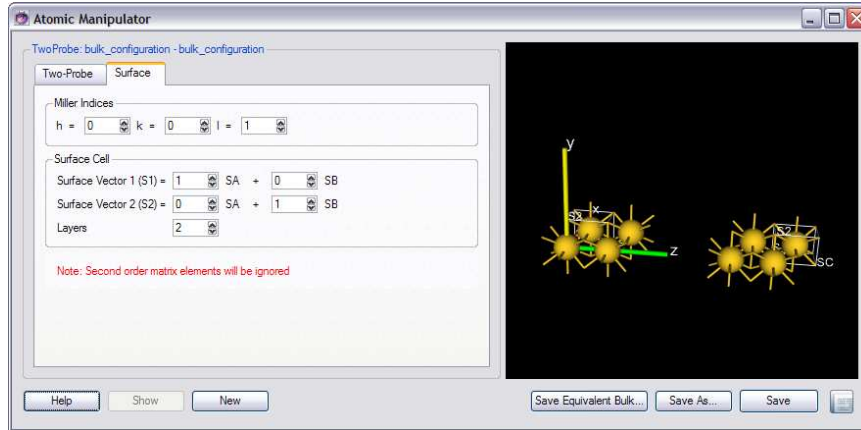


Figure 14: Screenshot of Atomistix software package.

3.4.1 Two-Probe Set-up

The general definition of a two-probe system is a geometry where two semi-infinite periodic systems, or **electrodes**, are combined with a finite scattering region, called the **central region**. The electrodes are created by cleaving a crystal or a nanotube, and the cleaved surfaces are then combined with the central region to form the two-probe system. VNL automatically takes care of most of the setup of the electrodes. Additional fine tuning, such as the positioning, rotation, and translation of molecules in the central region must be handled by the user. We give the details of the set-up in following paragraphs.

Cleaving a periodic system: When a periodic system, which can be either a bulk crystal or a nanotube, is open in the Atomic Manipulator, right-clicking either the left panel or the 3D preview window will display an option to **Cleave** the bulk. When the bulk is cleaved, it is transformed from a periodic system to a two-probe system without any central region. The result is two separate surfaces. Two new tabs, called **Two-Probe** and **Surface** appear in the Atomic Manipulator. Fig. 14 displays the screenshot of the set-up.

At the top of the **Surface** tab, three integer numbers (**h**, **k**, and **l**) corresponding

to the Miller indices for the crystal system are entered. The other important quantity to specify when setting up a surface is the two-dimensional surface cell that is spanned by two surface unit vectors (called S1 and S2). Combining the surface cell with a unit vector in the transport direction SC, we obtain the three-dimensional electrode cell (visualized as boxes around the atoms of the left and right electrodes). The part of each electrode that is contained in these boxes will be repeated periodically along the SC direction (which is always parallel to the Cartesian Z axis) to form semi-infinite electrodes.

Once the Miller indices have been specified, VNL will attempt automatically to determine the smallest possible surface unit cell, specified in terms of the primitive surface vectors SA and SB. A slight complication arises from the numerical requirement that the electrodes must be periodic in the transport direction. Therefore, for some Miller indices and crystal types, it is required that the surface cell contains more than one layer. Each atom with a unique Z coordinate defines a layer. A typical example is an fcc crystal cleaved along the [111] plane. In this case, the unit cell contains 3 atoms, corresponding to the stacking sequence ABC. The depth of the electrode cells is specified in terms of the number of layers in the direction perpendicular to the surface plane. By default, VNL suggests a number of layers that generates the smallest cell fulfilling the two basic requirements mentioned above. Usually, there is no reason to change this value. By default, the surface vectors S1 and S2 are set identical to the primitive surface vectors SA and SB. However, S1 and S2 can be defined as an arbitrary linear combination of SA and SB, and thereby control both the shape and the size of the surface cell.

The central region of a two-probe system: The central region of a two-probe system consists of all the atoms not included in the electrode cells. When cleaving a bulk, the `Atomic Manipulator` automatically adds several “electrode atoms”; these, however, are not contained in the electrode cell. These atoms are part of the central

region, and are so-called surface atoms. The number of surface atoms is controlled by the **Surface Layers** parameters, which can be set separately for the left and right electrodes. In general, these atoms can be separated into three groups: left surface atoms, right surface atoms, and the rest. There is no strict rule for choosing the right number of surface layers, but a good guess is to use values that give a surface depth comparable to the screening length (a certain distance away from the central region where the electrodes can be considered unperturbed by the addition of the molecule).

Close to the central region, the electrodes are modified by the presence of the molecule and the “gap” in the electrode material. The number of surface layers specify the extension of this perturbation region, i.e., the part of the electrodes in which the electron density may differ from its bulk equivalent. If this region is not long enough, implying that the influence of the central region in reality extends deeper into the electrodes, the central region will not be completely screened. As a consequence, the results will not be accurate. The recommended approach is to choose a moderate value for the number of surface layers, and then increase this systematically until the results converge.

Another parameter on the two-probe panel is the central region width, which is equivalent to the distance between the two last electrode atoms facing the central region. A new value for the central region width may be entered in the left panel, or one may use the **Translate** command from the context menu to move the electrode in a controlled fashion.

To insert molecules in the central region, simply drop a molecular configuration on the open **Atomic Manipulator** window. Also, new molecules can be added manually while working on a two-probe system by right-clicking the left panel and choosing **Insert** new molecule entry from the context menu. Working with molecules in the two-probe configuration of the **Atomic Manipulator** is completely analogous to creating molecules when it comes to positioning and orienting the molecule.

3.4.2 Analysis of Output

The simulation gives the transmission spectrum, transmission coefficients, eigenvalues, eigenstates, and density of states along with several other results, which are less relevant for our purpose of calculating transport properties. However, the output is generalized and the default values may not give the right interpretations. Therefore, in this part of the chapter, we discuss the analysis and interpretation of different simulation results.

Transmission Spectrum: The function calculates and returns the total transmission coefficient $T_\sigma(E)$, where σ is the spin as a function of the energy E based on a self-consistent two-probe calculation. The total transmission coefficient is defined as an integral of the \mathbf{k} -point dependent transmission coefficients $T_E(\mathbf{k}, \sigma)$ (It can be calculated separately using the function **Transmission Coefficients**.) over the \mathbf{k} -points (k_x, k_y) in the 2D Brillouin zone perpendicular to the transport direction.

Transmission Eigenvalues: The function calculates the transmission eigenvalues

$$\lambda_i(E, \mathbf{k}, \sigma), \quad i = 1, \dots, N_{\text{eigenchannels}} \quad (81)$$

for a given energy E and a given set of quantum numbers (\mathbf{k}, σ) . Here, $N_{\text{eigenchannels}}$ indicates the number of eigenchannels that corresponds to non-vanishing eigenvalues. The transmission eigenvalues $\lambda_i(E, \mathbf{k}, \sigma)$ are calculated as the eigenvalues of the Hermitian matrix $t^\dagger t$, where $t(E, \mathbf{k}, \sigma)$ is the transmission matrix.

Transmission Eigenstates: The function calculates and returns the transmission eigenstates $\Psi_n(E, \mathbf{k}, \sigma)$ corresponding to a given energy E and a given set of quantum numbers (n, \mathbf{k}, σ) . The transmission eigenstates $\Psi_n(E, \mathbf{k}, \sigma)$ are calculated as the eigenvectors (expressed in real space) of the Hermitian matrix $t^\dagger t$.

For all the transmission properties, the following values need to be defined.

1. Energies: A list of energies for which the transmission values should be calculated. The list is determined by specifying how many equidistant energy values there are from which starting value to which ending value.
2. Green's Function Infinitesimal: The imaginary infinitesimal added to the energy of the retarded Green's function.
3. Quantum Numbers: Sequence of quantum numbers (k -points for A and B) for which the transmission coefficients are to be calculated, and the spin of the system.

The rest of the parameters are left default. However, depending on the computation power, some can be changed to give more accurate results. A significant one is the `Brillouin Zone Integration` in the `Method` tab of `Nanolanguage Scripter`. The default values are set to 1 for number of k -points along x and y axis (A and B). This gives results for a one dimensional linear chain. But for more complicated systems, these values should be increased to obtain meaningful results.

3.5 Niobium Nanowire

We started the calculation of the transport properties of a niobium nanostructure by first simulating a perfect nanowire. Then we moved to more complex structures, namely the pyramid shaped electrodes of niobium to create a point contact. For this we used the relaxed structure obtained from SIESTA in previous chapter. We describe the simulation results below and simultaneously discuss the comparison with the previously published data.

3.5.1 Perfect Niobium Nanowire

The simplest form of nanowire is a one dimensional linear chain of niobium atoms separated by the lattice constant of bulk material, i.e., 3.3 Å. We followed the instructions given in the solved example of Atomistix manual for aluminum. So we picked

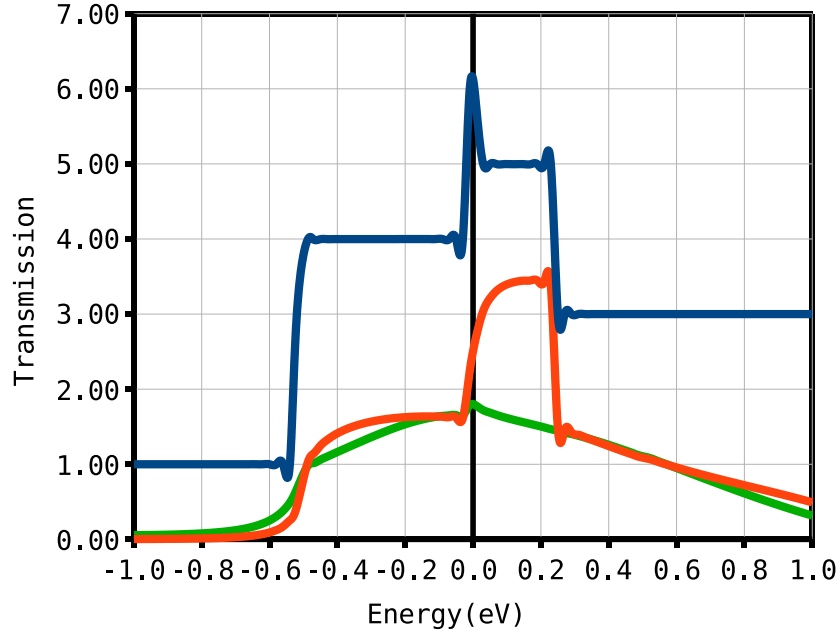


Figure 15: The transmission spectrum of a perfect niobium nanowire. The three curves represent following configurations: (1) the blue curve represents the configuration in which all the atoms are separated by the lattice constant (3.3 \AA); (2) the red curve displays that a niobium dimer in the wire reduces the transmission; and (3) the green curve shows that the transmission is further reduced when the dimer is displaced from its symmetric position.

up a linear chain template from the `Crystal Cupboard` and changed the `Basis` atom from carbon to niobium. In the `Atomic Manipulator`, we also changed the z axis lattice constant to 3.3 \AA and made the x and y axis separation very large (15.0 \AA) compared to the lattice constant. The linear chain was then cleaved to make electrodes and then we placed two more niobium atoms between the electrodes. We changed the `Width` between the electrodes to 9.9 \AA and placed the extra atoms were placed at distances separated by the regular lattice constant. Most of the parameters in `Nanolanguage Scripiter` were kept constant except for the `Analysis` tab we selected the `Transmission Coefficients`, `Transmission Eigenstates`, `Transmission Eigenvalues`, and `Transmission Spectrum`.

The results were obtained as expected. As shown in the blue curve of Fig. 15, we

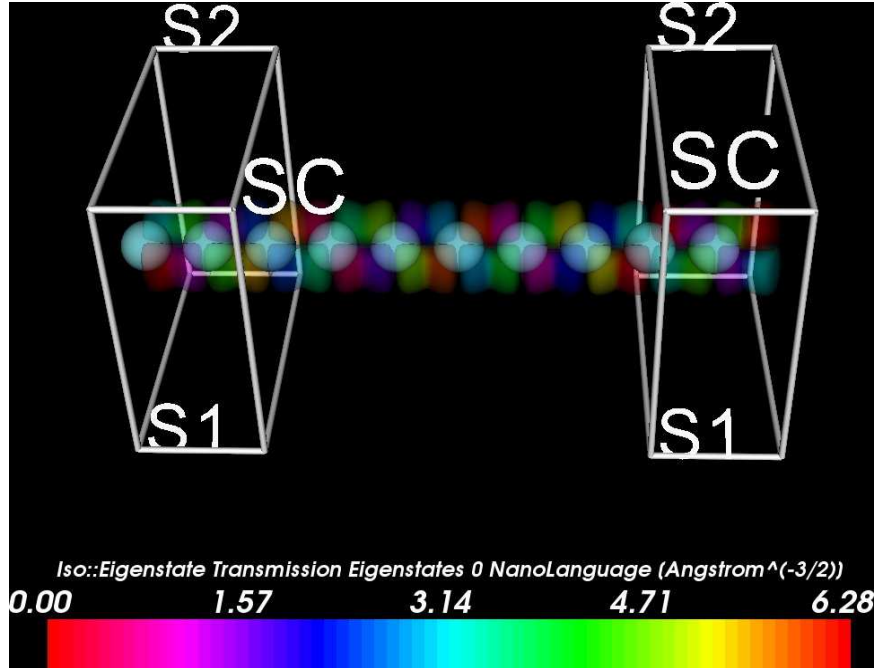


Figure 16: The transmission eigenstates of a perfect nanowire of niobium at isosurface 0.005.

see that niobium has six channels at Fermi energy that is consistent with the 5d and 4s orbitals of niobium. Because we are studying a perfect wire, the conductance is quantized in integer steps of $\frac{2e^2}{h}$ as expected from the Landauer formula $G = \frac{2e^2}{h} N(\epsilon)$, where $N(\epsilon)$ denotes the number of bands existing at the energy ϵ . The results are comparable to that of aluminum perfect wire analyzed by [40] because aluminum has three eigenchannels and niobium has six.

Further in Fig. 16 we display the transmission eigenstates of the perfect nanowire at isosurface 0.005. The eigenstates are calculated at $\mathbf{k} = (0.0, 0.0)$ because our system effectively is one-dimensional, and we require one k -point only in the transverse direction.

The transmission eigenvalues of the matrix $t^\dagger t$ are six integer values equal to unity representing the six eigenchannels. This is consistent with the transmission coefficient, 5.963 at Fermi energy. Theoretically, this value was expected to be 6.0 but it is off by a few decimal places because of the limitations of the mesh that can

be generated on a desktop computer.

Next we placed a dimer in the linear chain and performed the similar calculations. The dimer was placed such that the distances between the electrodes and two atoms of the dimer were similar to the distances obtained from the relaxed structure from SIESTA in the previous chapter of this thesis. To introduce the least error, we used the distances from the Ref. [3] for our calculations. So for a symmetrically placed dimer, we used $a = a' = 3.04 \text{ \AA}$ and $d = 2.05 \text{ \AA}$, where a and a' represent the distance from electrode to dimer, and d is the distance between the two dimer atoms. The red curve in Fig. 15 displays the effective transmission on the energy scale. Clearly, the dimerization reduces the transmission of individual channels, hence the total transmission is also reduced. All other parameters were kept similar to that of a perfect wire configuration where all the atoms are separated by the lattice constant of bulk niobium. Since the total conductance is transmission multiplied by the G_0 (conductance quanta), the conductance of wire with symmetrically placed dimer is $2.5G_0$ at Fermi energy. This value is comparable to $2.8G_0$, which is measured experimentally using the mechanically controlled break junction technique [3]. The difference in the values can be attributed to the fact that we are considering a one dimensional chain instead of the point contact.

To study the limits of the linear chain, we also simulated the configuration in which the dimer is displaced from its symmetric position. All other parameters were kept constant, and we obtained the transmission spectrum displayed by the green curve in Fig. 15. Again as expected the transmission reduced and the observed conductance value was $1.8G_0$, which is comparable to the experimental value of $2.1G_0$. The decreased conductance justified the name for anti-symmetric dimer configuration as the low conductance configuration.

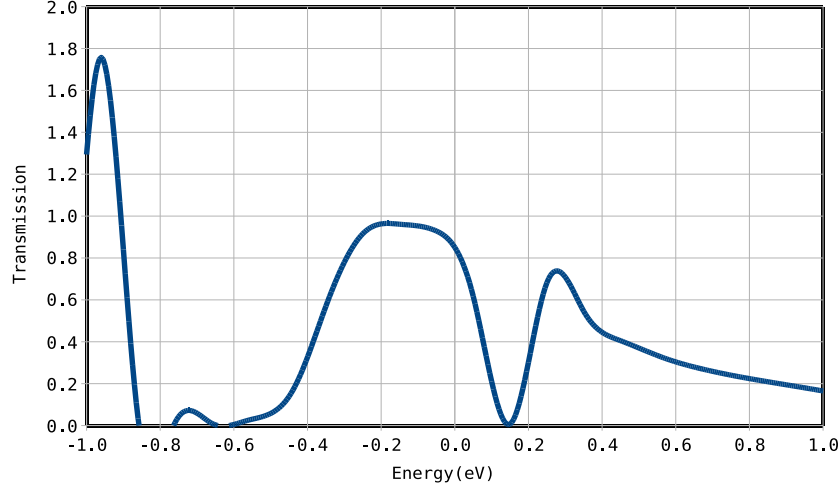


Figure 17: Transmission spectrum of point contact niobium nanowire.

3.5.2 Niobium nanowire point contact

Although a linear chain gives significant information, still there are differences as mentioned in the previous part. So we simulated a point contact to extract more information about the nanowire. We configured the coordinates of the niobium atoms such that they make a pyramidal shape and placed the dimer in between the electrodes. The arrangement is displayed in Figs. 18 and 19. To calculate the transmission spectrum, the range of energy was set from -1.0 to 1.0 eV. The resulting plot is displayed in Fig. 17. Further, we also calculated the transmission eigenstates and eigenvalues. For both the eigenstates and eigenvalues, we set the parameter `energy` that is scaled with respect to the Fermi energy equal to 0.0 eV, and the k quantum numbers were chosen to be (0.0,0.0) and (0.5,0.5). For the two quantum numbers the results are displayed in Fig. 18 and Fig. 19, respectively.

The results do not match the expected results published in Ref. [3]. The reason is attributed to the fact that we were not able to simulate the exact structure because of the limitations of computational power. Also, we could not find the transmission spectrum of the individual channels of niobium because Atomistix gives eigenvalues that are dependent on the quantum number, k . To find the transmission of a channel,

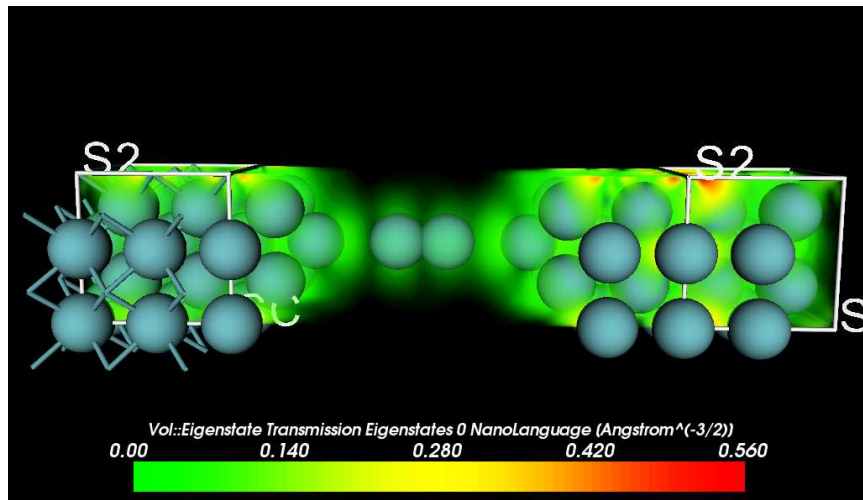


Figure 18: Transmission eigenstate 0.

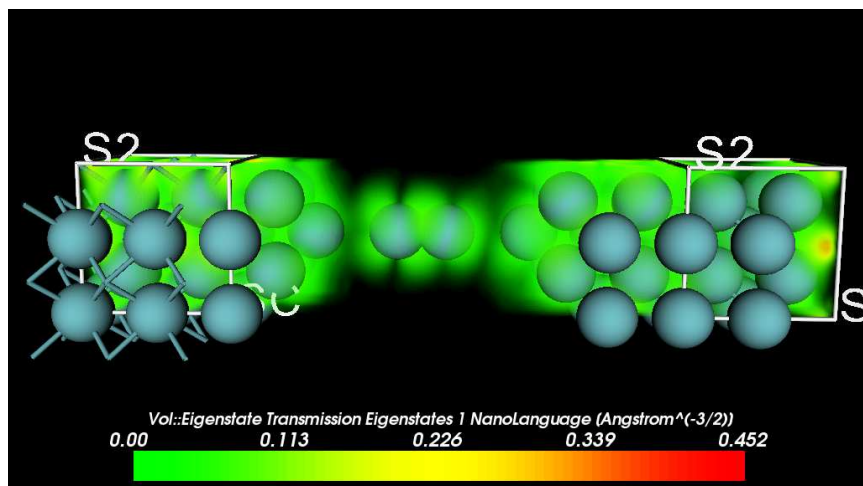


Figure 19: Transmission eigenstate 1.

we need to integrate over k_{\perp} [40].

$$G = \int \frac{d\mathbf{k}_{\perp}}{\Omega_{BZ}} G(\mathbf{k}_{\perp}), \quad (82)$$

where, Ω_{BZ} is the area of the first Brillouin zone and the integral is carried out by converting it into a finite sum $\int \frac{d\mathbf{k}_{\perp}}{\Omega_{BZ}} \rightarrow \sum_{\mathbf{k}_{\perp}} w(\mathbf{k}_{\perp})$, where $w(\mathbf{k}_{\perp})$ represents the weights of the discrete \mathbf{k}_{\perp} points. Since transmission and conductance, G are related by Eq. (26), the transmission of single channel depends on the weight, $w(\mathbf{k}_{\perp})$, and finding the weight was beyond the scope of the thesis. Although, I did not find the conductance of individual channels, the main achievement was obtaining the transport properties on nanowires on a desktop computer.

3.6 Graphene

Graphene is a rapidly rising star on the horizon of materials science and condensed matter physics. This strictly two-dimensional material exhibits exceptionally high crystal and electronic quality and, despite its short history, has already revealed a cornucopia of new physics and potential applications. Owing to its unusual electronic spectrum, graphene has led to the emergence of a new paradigm of “relativistic” condensed matter physics, where quantum relativistic phenomena, some of which are unobservable in high energy physics, can now be mimicked and tested in tabletop experiments. More generally, graphene represents a conceptually new class of materials that are only one atom thick and, on this basis, offer new inroads into low-dimensional physics that have never ceased to surprise and continue to provide a fertile ground for applications. Graphene is the name given to a flat monolayer of carbon atoms tightly packed into a two-dimensional (2D) honeycomb lattice and is a basic building block for graphitic materials of all other dimensionalities. It can be wrapped up into 0D fullerenes, rolled into 1D nanotubes, or stacked into 3D graphite. Graphene also provides an excellent condensed-matter analogue of (2+1)-dimensional quantum electrodynamics [41, 42, 43], which propelled graphene into a thriving theoretical toy

model. On the other hand, although known as integral part of 3D materials, graphene was presumed not to exist in the free state, being described as an “academic” material [42] and believed to be unstable with respect to the formation of curved structures such as soot, fullerenes, and nanotubes. All of a sudden, the vintage model turned into reality, when free-standing graphene was unexpectedly found three years ago [44, 45] and, especially, when the follow-up experiments [46, 47] confirmed that its charge carriers were indeed massless Dirac fermions. So, the graphene “gold rush” has begun.

3.6.1 Transport Properties

The high electronic mobility found in graphene nanoribbons (GNRs) and the facilities for their growth suggest they may be used for future electronics and in many other nano-technological applications. GNRs are single atomic layers that are understood as an infinite unrolled carbon nanotube. Similar to the case of nanotubes, ballistic transport and quantized electronic conductance are expected to be found in graphene structures. In particular, different quantization rules have been predicted for clean zigzag-GNRs and armchair-GNRs. Edge states in zigzag ribbons provide a single channel for electron conduction which is not the case for armchair configuration. Distinct and amusing designs of GNRs are proposed to highlights their peculiar transport properties. One example is the manifestation of the so-called Klein paradox [48], that predicts that the electron can pass through a high potential barrier without an exponential decay. Also interesting is the discussion about the possible manifestation of half-metallicity in nanometer-scale GNRs reported on recent first-principles calculations [49]. From the point of view of applications, it has been shown that graphene exhibits chemical sensors properties. Recently, it was reported a graphene-based gas sensor allows the detection of individual gas molecules adsorbed on graphene. In this work, we will focus on the effects of side-attached one-dimensional chains of hexagons

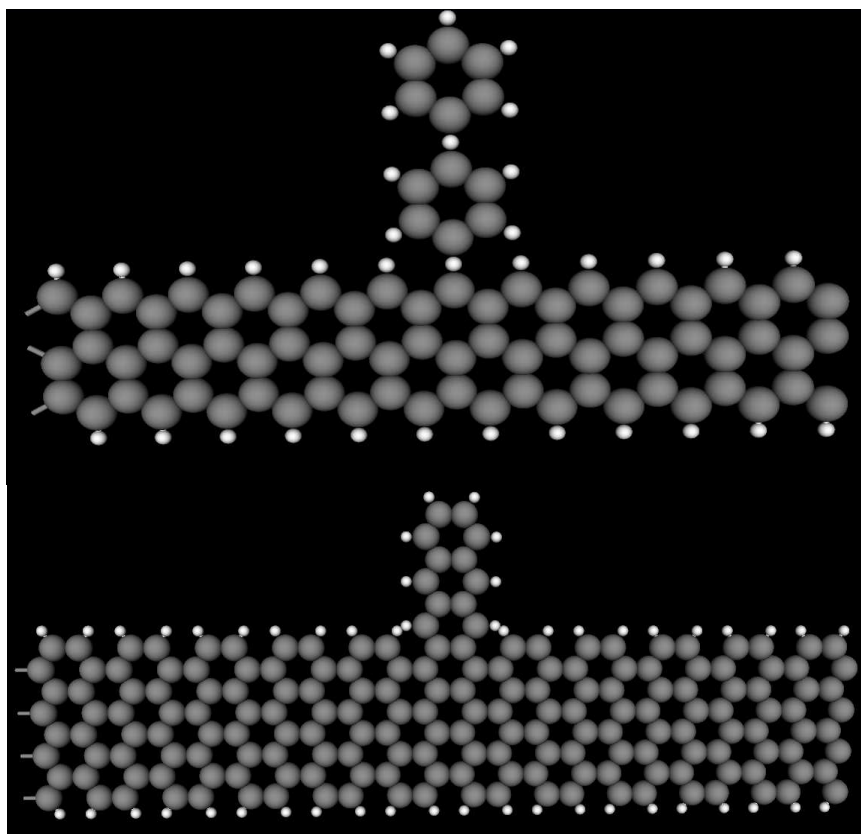


Figure 20: The top (bottom) figure displays a zigzag (armchair) graphene nanoribbon with a aromatic ring attached on its side.

pinned at the edges of the GNRs. These one dimensional chains could be useful to simulate, qualitatively, the effects on the electronic transport of GNRs when benzene-based organic molecules are attached into the edges of the ribbons. A simple scheme is proposed to reveal the main electronic properties and the changes on the conductance of such decorated planar structures. For simplicity, we consider the structures shown in Fig. 20 for armchair (AGNRs) and zigzag (ZGNRs) nanoribbons with the linear poly-aromatic hydrocarbon as the organic molecules attached to the nanoribbons.

3.6.2 Simulation and Results

In this section we will present how the capabilities in *ATOMISTIX TOOLKIT* and *VNL* can be used to study various types of systems involving graphene, ranging from

a simple, infinite sheet of graphene to complex junctions that are investigated for, e.g., gas sensors. The geometrical structure of graphene is simple and regular, and the infinite, planar structure is readily available in the `Crystal Cupboard` in VNL. However, to create any kind of device-like structure, the infinite sheet must be cut into a suitable shape. A common shape, at least for electronics applications, is a so-called graphene nanoribbon (GNR). These can actually be quite cumbersome to set up in an effective manner, not least considering the required protonization of the edges (hydrogen termination) that is needed in finite structures in order to satisfy all carbon valence electron bonds. Therefore, here we use a `NanoLanguage` script provided with the VNL for constructing graphene nanoribbons.

The graphene ribbon script itself is relatively simple (less than 100 lines of code) and quite instructive with detailed comments. However, it is not necessary to dig into the code at all in order to use the script in practice. The only thing required is the modification of four simple parameters. The parameters are easy to understand, and there are only four basic ones:

- **armchair**: The option allows us to choose an armchair/zigzag ribbon by setting this parameter to `True/False`.
- **width**: The width of the ribbon is specified by the number of atomic layers across the ribbon. This number must be even for zigzag ribbons.
- **repetitions**: This parameter configures the number of times the unit cell should be repeated along the ribbon.
- **PAC**: Set this parameter to `True/False` to select whether the structure should be constructed as a `Periodic Atom Configuration` (`True`) or a `Molecule Configuration` (`False`).

To set up a two probe system of a zigzag or armchair ribbon, drop the script on the `Atomic Manipulator`, and create the two electrodes. Although VNL is satisfied

with only one repetition of the electrode cell, it is safer to select two periods to ensure quality results. The calculation time overhead will be very small. To create the central region we can simply choose a suitable number of surface layers. Any even number, both left and right, will work geometrically, but to ensure sufficient screening, we used at least 8 layers both left and right. To close the gap between the left and right surfaces, the central region width should be set to 1.23 \AA , which is consistent with the C-C bond length in graphene. The benzene rings were inserted using the `Molecular Configuration` tab in VNL. The rings were translated and rotated to place them in appropriate positions as shown in Fig. 20. Additionally, the hydrogen atoms were adjusted to satisfy the valency of the graphene and benzene bonds. We change the basis set to `SingleZeta` to speed up the calculations, and the `Brillouin Zone Integration Parameter` values were set to 20, 2, and 100 for x , y , and z axis, respectively. While choosing these parameters we maintained a balance between the computation power and accuracy of the results. (Note: The transport properties are calculated in the z direction and the ribbon extends along x axis.) On the `Analysis` tab we select `Transmission Spectrum` (100 points from 5 eV to +5 eV), and `Transmission Eigenstates` at 0 eV.

The graphs in Fig. 22 display the results of simulation of GNR after adding the benzene rings. Here all the energies are scaled with respect to Fermi energy. The transmission spectrum displays the black curve for the transmission of a zigzag graphene nanoribbon in absence of any aromatic rings. The red curve is for one aromatic ring, whereas the green curve displays the effect of adding two rings. A prominent feature of the spectrum is the enhanced transmission near the Fermi level. This peculiarity can be attributed to the conductance gaps due to the Anderson localization of electrons [50, 51, 52, 53]. Further, in the presence of benzene we see the dips in the transmission spectrum and peaks in the DOS plot at particular energies that increase with the increase in the number of rings. Although a complete

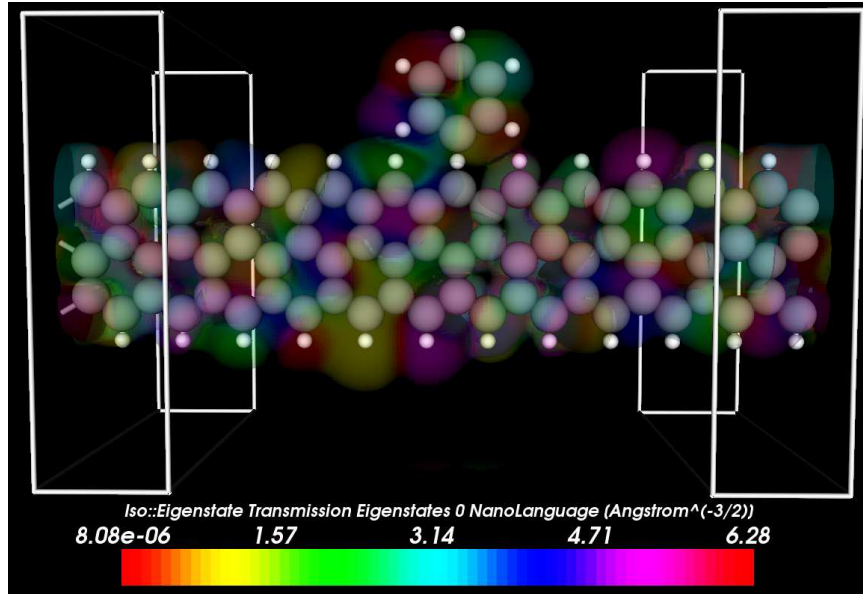


Figure 21: The figure displays the zigzag graphene nanoribbon (width = 6) with an aromatic ring attached on its side. It also displays transmission eigenstates. The color bar across the bottom gives information about the particular transmission value at certain locations on the nanoribbon.

theory of the dips, also known as the Fano antiresonances (FARs), is not discussed in this thesis; in brief, the dips emerge in a system when discrete states coexist with continuum energy states [54]. Essentially, the behavior of the electronic transport is in agreement with the expected results proved by other authors [55].

The armchair nanoribbon was a comparatively complex structure because the side-attached rings were connected to the ribbon via more than one C-C bond. The corresponding transmission spectrum and DOS plot are displayed in Fig. 24. Besides the ideal AGNR transmission displayed by the black curve, the figure displays the effect of aromatic rings. It should be noted that N=1 configuration (red curve) is not a complete ring. Two carbon atoms and equivalent valence hydrogen atoms are removed from the benzene ring to match the geometry. Again, like the ZGNAR plot, we have the green and blue curves for the addition of one and two rings, respectively. The results are in complete agreement with the results published by Rosales, et al. [55].

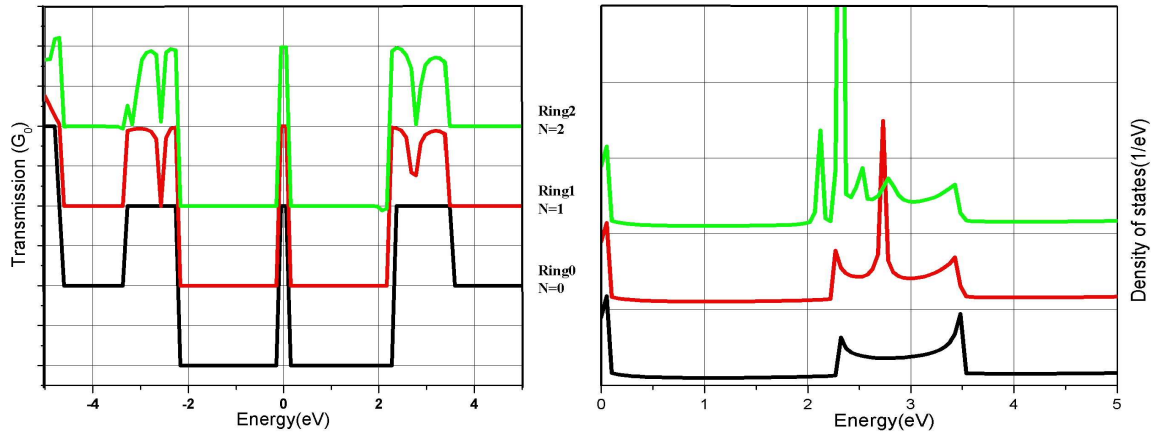


Figure 22: The graphs displays transmission spectrum (left) and density of states (right) of graphene in presence of aromatic rings. The black curve displays the transmission of a zigzag graphene nanoribbon in absence of any aromatic rings. In the presence of benzene we see dips in transmission (left) and peaks in DOS (right) at particular energies (scaled with respect to Fermi energy) which increase with an increase in the number of rings. The red curve is for one aromatic ring, whereas the green curve displays the effect of the addition of two rings.

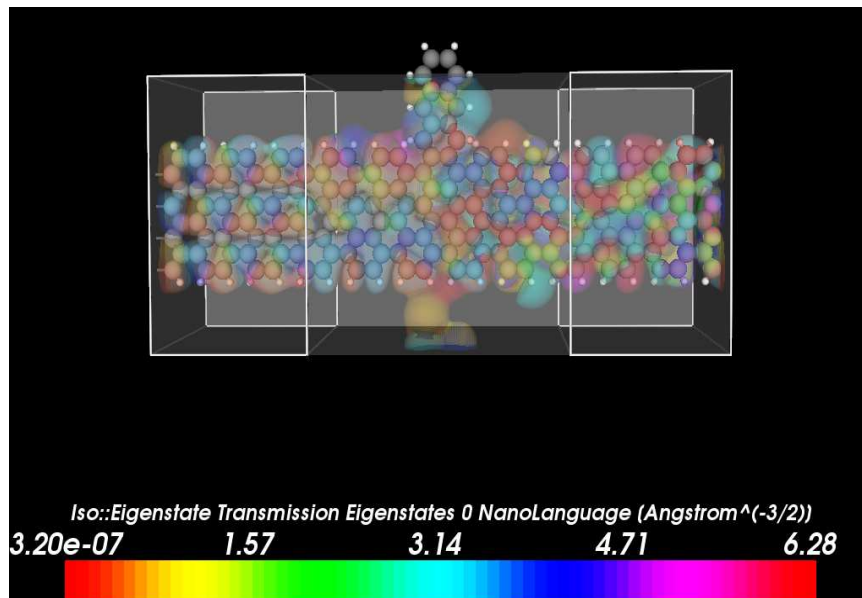


Figure 23: The figure displays the armchair graphene nanoribbon (width = 6) with a aromatic ring attached on its side. It also displays transmission eigenstates. The color on the graphene nanoribbon can be interpreted using the color bar in the bottom. The color shade gives the particular transmission value at certain locations on the nanoribbon.

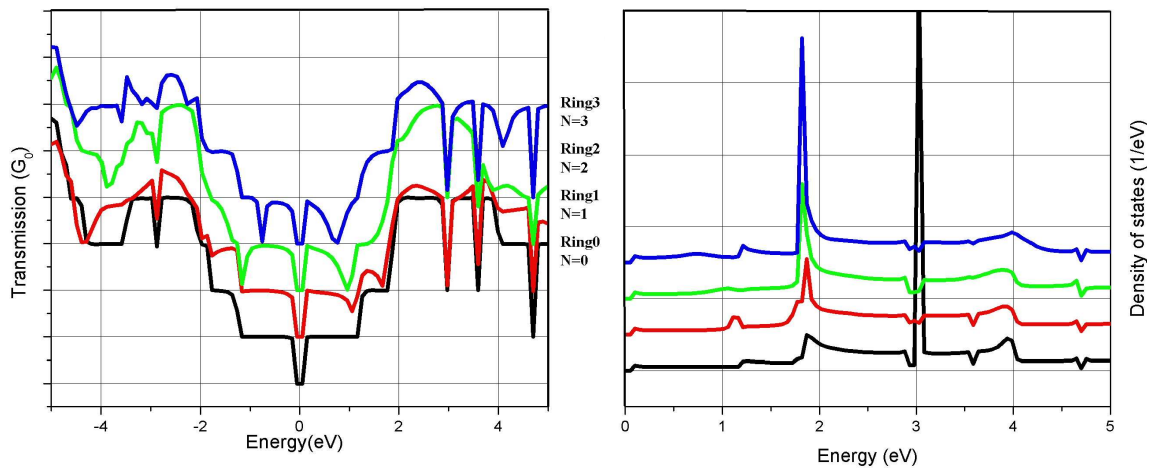


Figure 24: The graphs displays transmission spectrum (left) and density of states (right) of graphene in the presence of aromatic rings. The black curve displays transmission of a armchair graphene nanoribbon in the absence of any aromatic rings. In the presence of benzene we see dips in transmission (left) and peaks in DOS (right) at particular energies (scaled with respect to Fermi energy) which increase with increase in number of rings. The red curve is for one aromatic ring, the green curve for two rings, and the blue curve for three rings.

In conclusion, this chapter provides a method for theoretical calculations of the transport properties of nanostructures. Although, theoretical explanation of the curves are described briefly, the main emphasis was on the method of computing the results. Although there are limitations because of the computation power, we still obtained results which give significant information about the behavior of mesoscopic quantities. It is worth mentioning here that we have used only a single processor mode of the package, and the software can be used in parallel mode on dual or quad processor computers. Thus, more complicated structures like biomolecules and proteins can be simulated. Therefore the method described and tested in this chapter gives a beginning of a new dimension of research.

CHAPTER IV

PICONEWTON FORCE SENSOR AND ITS CALIBRATION

In nanoscale physics the correlation in structure and transport properties of nanosystems is of particular interest and innovative research methods and techniques capable of measuring several properties simultaneously are required. Therefore, this chapter describes the experimental approach planned to verify the simulation results presented in previous chapters. To verify the relaxed structure obtained by minimizing the force and energy simultaneously, we designed a force sensor that can measure potentially piconewton forces. Depending upon the order of magnitude of force, using the Newton's second law of motion, different methods can be employed to measure force. But forces of atomic scales are difficult to measure, and the need for measuring these forces in both industrial and research environments has increased the role of force sensors. Among the different available sensors that measure forces of atomic scales, the Atomic Force Microscope (AFM) is the one most widely used. In experimental condensed matter physics, the AFM is used to scan surfaces, to measure the nano-scale forces and for many similar applications. The heart of the AFM and other surface profilometers is the sensor tip, which maps the surface. The forces acting on the tips are usually sensed by mounting the tip on a cantilever beam (CL). Optical detection is the most common method to detect the deflection, but piezoresistive and piezoelectric detection schemes are also available. The piezoelectric quartz tuning forks (QTF), which are produced annually in millions mainly for the watch industry, can be used as force sensors instead of CLs. Giessibl [56] showed various advantages of using tuning forks in the AFM, the most remarkable is using tuning forks in a

cryogenic environment.

Continuing with the QTF approach, an absolute calibration of these forks is presented in this chapter. Some terminology is presented first to provide a common basis for understanding the cantilever motion in force sensors. The first section is the theoretical background for the calibration process. Then, we present the experimental designs and results of the calibration process. We measured frequency shift with respect to pressure and related it to the added mass that can be connected to external force acting on the QTF. We also compared our results for alignment of QTF in a gravity field. The perpendicular and parallel alignment gives different results. Further the experiment is performed at low temperature. The obtained results agree with the theoretical prediction. This shows that this method of measuring force gives us more flexibility to measure the forces in different environments as compared to normal AFMs. Next, we combine this force measurement setup with a simple scanning probe microscopy. Although this method of measuring force has several advantages, it was not used for the actual measurements. Instead, a more robust system that uses the micro-fabrication techniques was used to verify the niobium nanowire structure and transport properties. This system is discussed briefly in last section.

4.1 Theoretical Background

In this section we introduce the theory used to deal with the QTFs. Since the individual prongs of QTFs (Fig. 30) are like vibrating prismatic beams, first we introduce the model for vibration of cantilever in viscous fluid. We begin with a brief description of the derivation of the ratio of resonance frequency of cantilever in fluid, ω_f , to that in a vacuum, ω_{vac} [57]. The ratio involves a cantilever geometry dependent function, namely the hydrodynamic function. Next, we derive this function for the prismatic geometry of our cantilever. The following section combines the prior two sections and

gives a simplified equation for the normalized frequency shift, which is the main measurement parameter of our system. Then, we describe the effect of adding an external mass on the QTF to change the resonance frequency of the cantilever. Additionally, we present an equivalent electronic circuit of our piezoelectric QTF that was used to measure the resonance frequency using a network analyzer and to analyze of observed data. Finally, we demonstrate that the resonance frequency and the quality factor depend on the temperature.

4.1.1 Resonance frequency of cantilever

In this section, we present a general theory for the dynamic deflection of a cantilever beam immersed in a viscous fluid and excited by an arbitrary external driving force. Also, here we derive the theory applicable to any cross section that is uniform along its entire length. The governing equation for the dynamics deflection function, $w(x, t)$ of such a cantilever is [57]:

$$EI \frac{\partial^4 w(x, t)}{\partial x^4} + \rho_c h b \frac{\partial^2 w(x, t)}{\partial t^2} = F(x, t), \quad (83)$$

where E is the Young's modulus, I is the moment of inertia of cantilever, and ρ_c is the density of cantilever. Also the dimensions of the cantilever are given by L , b , and h corresponding to length, width, and thickness of the cantilever. The right hand side of the equation has the external applied force per unit length, F , that is the function of the spatial coordinate x along the length of cantilever, and t is the time. The boundary conditions for Eq. (83) are the clamped and free ends of the cantilever that can be represented by following mathematical expressions:

$$\left[w(x, t) = \frac{\partial w(x, t)}{\partial x} \right]_{x=0} = \left[\frac{\partial^2 w(x, t)}{\partial x^2} = \frac{\partial^3 w(x, t)}{\partial x^3} \right]_{x=L} = 0. \quad (84)$$

Since we are interested in deriving an expression for frequency, it is easier to proceed with the Fourier transform ($\hat{X} = \int_{-\infty}^{\infty} x e^{i\omega t} dt$) of Eq. (83). We obtain

$$\frac{EI}{L^4} \frac{d^4 W(\hat{x}|\omega)}{dx^4} - \rho_c h b W(\hat{x}|\omega) = \hat{F}(x|\omega). \quad (85)$$

For a cantilever moving in fluid, the external force has the hydrodynamic loading component, $\hat{F}_{hydro}(x|\omega)$, and the driving force term, $\hat{F}_e(x|\omega)$ (applied electric potential across the piezoelectric QTF.) The driving force is taken arbitrarily, so Eq. (83) can be solved by first replacing this function with a Dirac-delta function and then using Green's function theory. However, at this point we are more interested in the resonance frequency instead of complete solution of the equation, therefore we need to consider the hydrodynamic force in detail. This force can be obtained from the Navier-Stokes equation given by:

$$\rho \left(\frac{\partial \mathbf{u}}{\partial t} + \mathbf{u} \cdot \nabla \mathbf{u} \right) = \nabla p + \eta \nabla^2 \mathbf{u} + \mathbf{f}, \quad (86)$$

where ρ is density of fluid, \mathbf{u} is flow velocity, p is the pressure, and η is its viscosity. Under the incompressible assumption, density is a constant and it follows that the gradient of the velocity field is zero, i.e., $\nabla \cdot \mathbf{u} = 0$. This equation is more specifically a statement of the conservation of volume and a necessary condition for Newtonian fluids. Further, we take the Fourier transform of the fluid flow equation and apply an extra condition that the external force, $\mathbf{f} = 0$, to obtain the following form of Eq. (86):

$$-\nabla \hat{p} + \eta \nabla^2 \hat{\mathbf{u}} = i\rho\omega \hat{\mathbf{u}}. \quad (87)$$

Now we calculate the effect of the hydrodynamic force on the cantilever [58] using the generalized expression for force vector, \mathbf{F} , on any three-dimensional body with surface \mathbf{S} , moving in any manner whatsoever in an incompressible viscous fluid, which is at rest at infinity.

$$\mathbf{F} = \int_{\mathbf{S}} [-pd\mathbf{S} + \rho\Omega \times d\mathbf{S}]. \quad (88)$$

This equation gives force per unit length using the parameters, pressure per unit length, p , and the curl of velocity field which is commonly known as vorticity, Ω . These parameters can be obtained from solving Eq. (87), and we obtain a general

form of the $\hat{F}_{hydro}(x|\omega)$ as:

$$\hat{F}_{hydro}(x|\omega) = \frac{\pi}{4}\rho\omega^2b^2\Gamma(\omega)\hat{W}(x|\omega), \quad (89)$$

where the function $\Gamma(\omega)$ is hydrodynamic function, and it depends on the geometry of the cantilever. We calculate this function in the next part of this section. But now, we plug in the equation for generalized hydrodynamic force in Eq. (85), and we obtain,

$$\frac{d^4\hat{W}(x|\omega)}{dx^4} - C_1^4\left(\frac{\omega}{\omega_{vac,1}}\right)^2\left(1 + \frac{\pi\rho b}{4\rho_c h}\Gamma(\omega)\right)\hat{W}(x|\omega) = \frac{\hat{F}_e(x|\omega)L^4}{EI}, \quad (90)$$

where $\omega_{vac,1}$ is the fundamental radial frequency of the beam in vacuum given by,

$$\omega_{vac,1} = \frac{C_1^2}{L^2}\sqrt{\frac{EI}{\rho_c hb}}, \quad (91)$$

and $C_1 = 1.875104\dots$ is the smallest positive root of the cantilever boundary condition equation [59]:

$$1 + \cos C_n \cosh C_n = 0, \quad n = 1, 2, 3, \dots \quad (92)$$

Finally, in the absence of dissipative effects, the resonant frequency of cantilever ω_f in presence of fluid is given by:

$$\frac{\omega_f}{\omega_{vac}} = \left(1 + \Gamma(\omega)\frac{\pi\rho b}{4\rho_c h}\right)^{-1/2}. \quad (93)$$

For gases $\frac{\rho}{\rho_c}$ is of the order of 10^{-2} . So, we expand Eq. (93) and obtain the shift in resonance frequency

$$\frac{\omega_f}{\omega_{vac}} - 1 = \frac{\Delta\omega_f}{\omega_{vac}} = -\Gamma(\omega)\frac{1}{2}\frac{\pi\rho b}{4\rho_c h}. \quad (94)$$

Since $\omega = 2\pi f$, we have

$$\frac{\Delta f}{f_0} = -\Gamma(\omega)\frac{1}{2}\frac{\pi\rho b}{4\rho_c h}. \quad (95)$$

4.1.2 Hydrodynamic function

We now present analytical expressions for the hydrodynamic function, $\Gamma(\omega)$, of a prismatic cantilever. Investigations of Tuck [58] have demonstrated that for a cylindrical beam the hydrodynamic function is given by

$$\Gamma(\omega) = 1 + \frac{4iK_1(-i\sqrt{iRe})}{\sqrt{iRe}K_0(-i\sqrt{iRe})}. \quad (96)$$

Here, the functions K_0 and K_1 are modified Bessel functions of the third kind. The Reynolds number is given by

$$Re = \frac{\rho\omega d^2}{4\eta}, \quad (97)$$

where d is the diameter of cylinder and corresponds to dominant length scale in the hydrodynamic flow. ω is the vibration frequency of the cantilever and gives the dominant time scale for the motion in fluid. An infinitesimally, thin rectangular cantilever has approximately identical function, as that of the cylinder and the deviations between the two functions never exceed 15% over the range $0.1 \leq Re \leq 1000$. Furthermore, from Appendix 1 of Ref. [58], it is evident that the hydrodynamic function for a cylindrical or a rectangular cantilever possess the same asymptotic forms in the limits as $Re \rightarrow 0$ and $Re \rightarrow \infty$, namely,

$$\Gamma(\omega) = \begin{cases} 1 & : Re \rightarrow \infty \\ \frac{-4i}{Re \ln(-i\sqrt{iRe})} & : Re \rightarrow 0 \end{cases}. \quad (98)$$

Also Dorignac, et al., [60] demonstrated that if the Reynolds number is ≈ 0.05 , there is negligible difference between the values of hydrodynamic functions of cylindrical and prismatic cantilevers. Since our system a has Reynolds number of the same order, we use this approximation for our calculations of hydrodynamic function for the prong of the QTF. To verify the above approximation we used the package, *COMSOL Multiphysics*, that uses the finite-element method to solve the required differential equations. The model for the simulation was designed such that we fixed

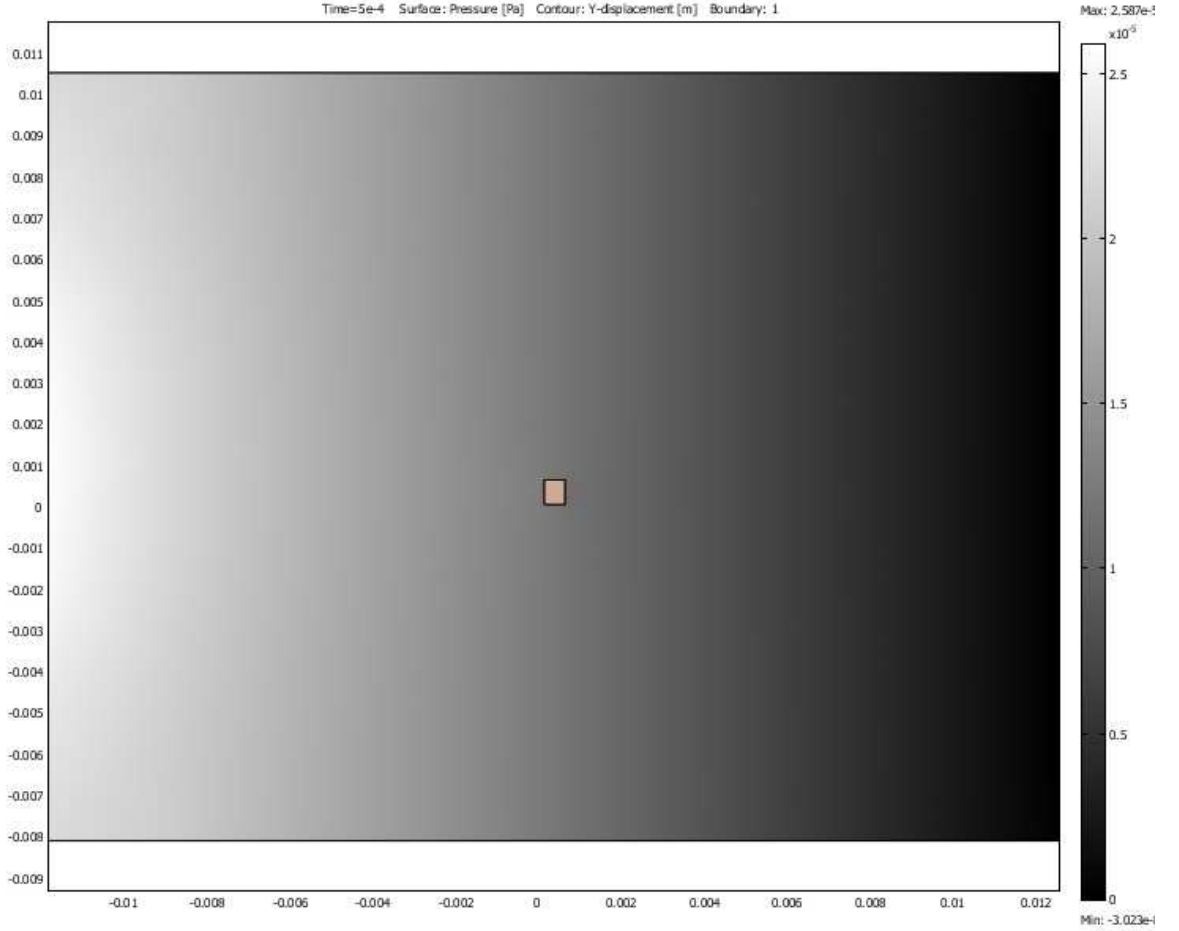


Figure 25: Surface pressure profile of fluid using the color map. The maximum and minimum values represented by the particular color are shown on the scale on the right. Also the scale on the right and bottom of the figure can be used to find the width and height of cantilever.

the cantilever and moved the fluid with the velocity of the same order as that of the cantilever motion. We obtained the velocity field displayed in Fig. 26 and the pressure field of the fluid displayed in Fig. 25. Then we used Eq. (88) to obtain the force per unit length, \mathbf{F} , by surface integration of pressure and vorticity (curl of velocity field). We compared these values with Eq. (89). All the parameters in this equation are known, except the hydrodynamic function, $\Gamma(\omega)$. Thus we obtained the unknown function and plotted it with respect to pressure as shown in Fig. 27. This graph supports our hypothesis that the hydrodynamic function can be taken as unity for the pressure lying between 0.1 to 1.0 bar. We discuss the theory and

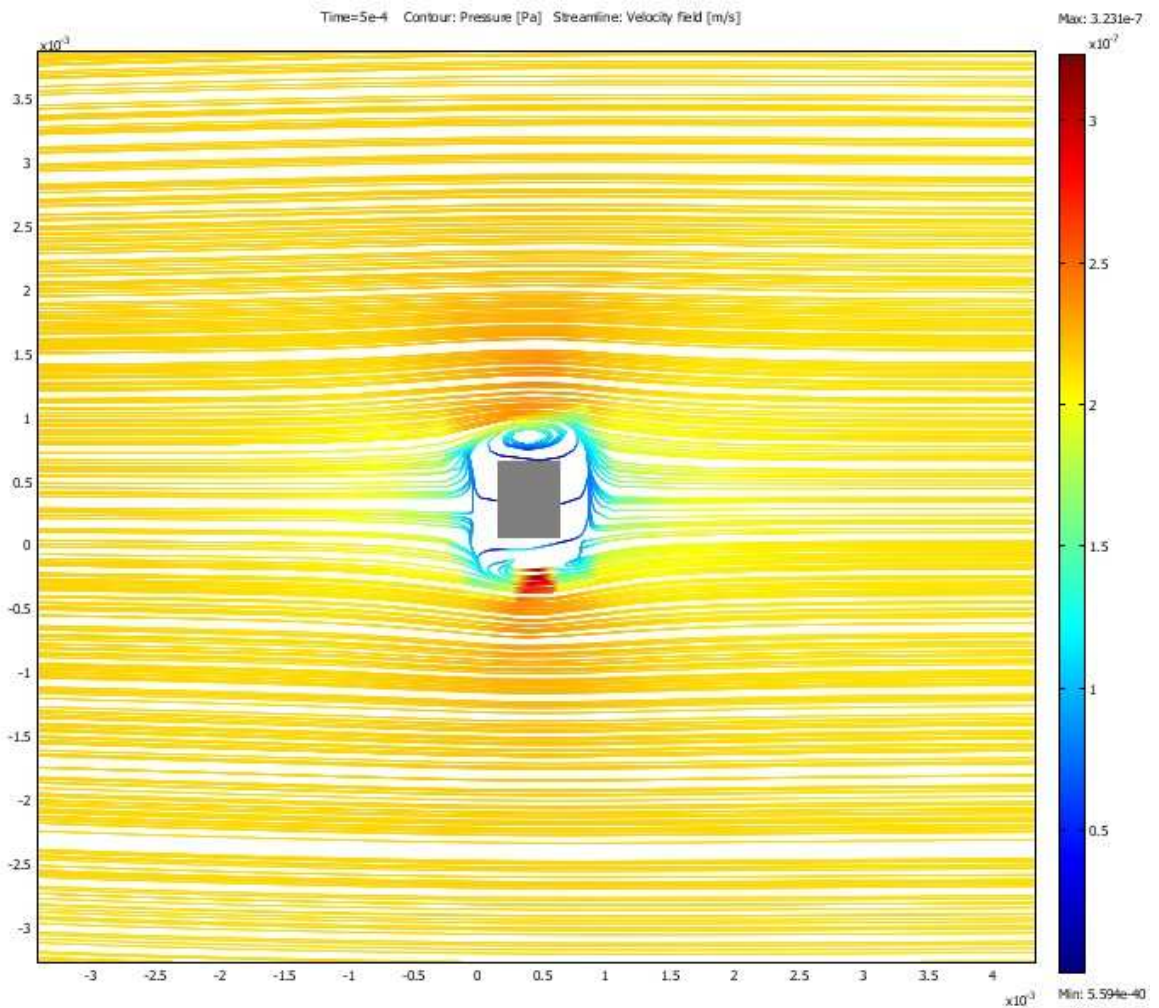


Figure 26: Velocity of fluid is plotted using the color map. The maximum and minimum values represented by the particular color are shown by the scale on the right.

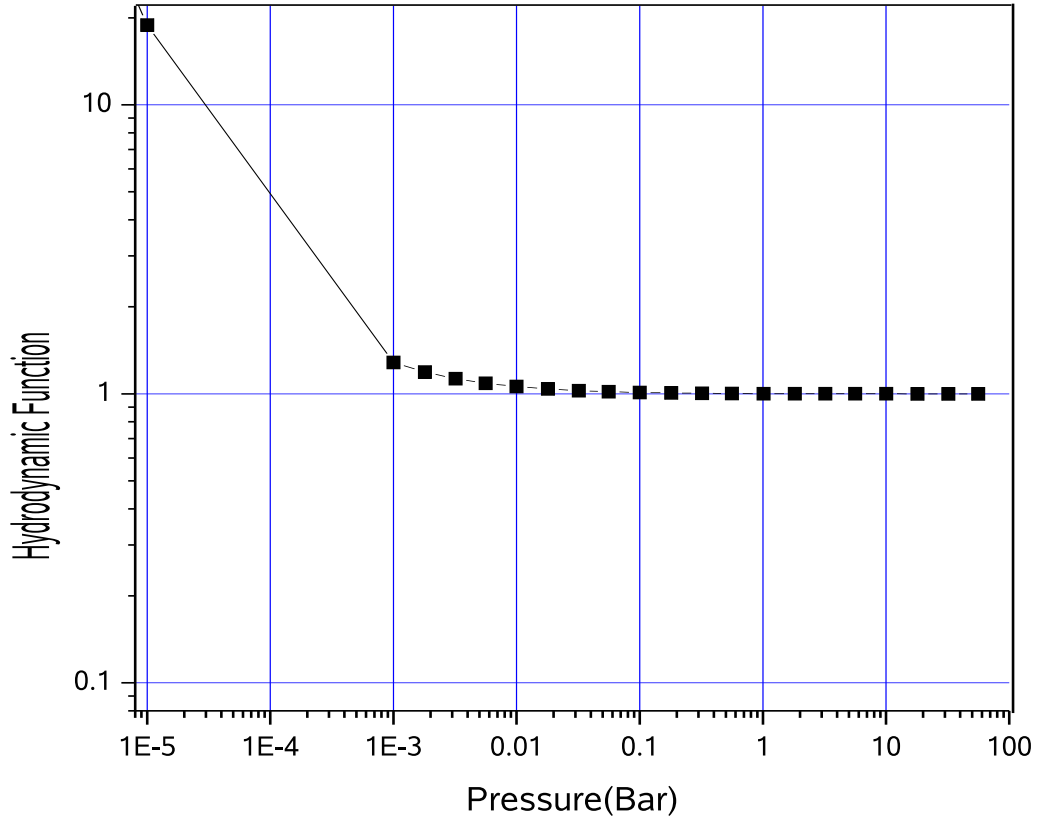


Figure 27: The hydrodynamic function for a rectangular cross-section geometry is displayed in this graph. For pressure range, $0.1 < \text{pressure} < 1.0$ bar, this function can be considered unity.

approximations for pressures below 0.1 bar in the next chapter.

4.1.3 Adding an external mass on QTF

With the approximation of hydrodynamic function, we have the complete theory for the required calibration. Eq. (95) gives a linear correspondence between the resonance frequency of the QTF and the fluid density. In the following part, we show that an external force acting on the QTF has an equivalent linear correspondence relation that connects the force on the cantilever with the $-\Delta f/f_0$. Therefore, once we establish this equivalent relation, we will have the absolute force measurement

technique because the proportionality constants for force measurements are similar to that for the calibration process. The external force acting on the prong can be considered as an external mass glued to the tuning fork. The effect of external mass on the resonance frequency of the cantilever can be estimated using the fact that $-\Delta f/f_0$ is proportional to added mass, m . It can be easily checked using the relation for simple harmonic oscillation.

$$\begin{aligned} f &= \frac{1}{2\pi} \sqrt{\frac{k}{m_0 + m}} & (m_0 = \rho_c Lhb) \\ \frac{\Delta f}{f_0} &\approx -\frac{1}{2} \frac{m}{m_0}. \end{aligned} \quad (99)$$

Here, k is the effective spring constant of the QTF, m_0 is effective mass of the QTF, f_0 is resonance frequency when $m = 0$. So, f_0 in this equation is equivalent to that in previous discussion of cantilever vibrating in a fluid at very low pressure. This relationship shows that the shift in resonance frequency is proportional to extra added mass and inversely proportional to mass of QTF. Thus, if m_0 is known, we can find m by measuring $-\Delta f/f_0$ hence the force acting on the QTF. The approximate sign shows the approximation that m is much smaller than m_0 . Christen [61] has studied the air and gas damping on vibrating QTF. Higher pressure range has shown that

$$\frac{\Delta f}{f_0} = -\frac{1}{2} \frac{M}{\rho_c A} \quad (100)$$

Here, M is mass per unit length, i.e., the uniform load on the beam, and A is cross-sectional area. By simply knowing ρ_c and A , we obtain a direct measure of added mass M . The resonance frequency of the QTFs is measured with respect to different pressures, and then using Eq. (95) we found the effective density, ρ_c . Using the measured values of dimensions of QTFs, we found the effective mass, (m_0), of cantilever.

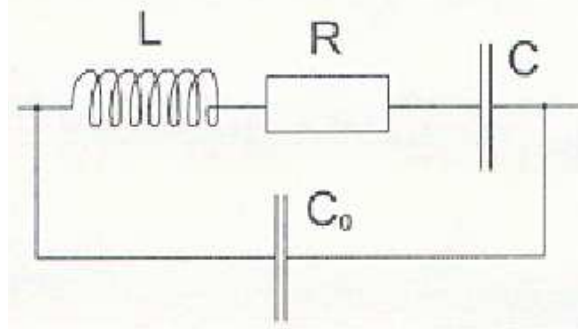


Figure 28: Butterworth-Van Dyke circuit.

4.1.4 Electrical equivalent circuit of quartz tuning fork

Piezoelectric oscillators can be modeled by an electronic equivalent circuit called the Butterworth-Van Dyke (BVD) circuit shown in Fig. 28. The LCR resonator models the mechanical resonance: the inductance, L , stands for the size of kinetic energy storage, i.e., the effective mass; the capacitance, C , reflects the potential energy storage, i.e., the spring constant; and the resistor, R , models the dissipative processes. The parallel capacitance, C_0 , is given by the contacts and cables. The transfer function $Y(\omega) = I(\omega)/U(\omega)$, the so called admittance, is

$$Y(\omega) = \frac{1}{R + \frac{1}{i\omega C} + i\omega L} + i\omega C_0, \quad (101)$$

and is experimentally measurable. The admittance of the LCR branch is small and can be compensated electronically with a bridge circuit. In Fig. 29 we plot the phase and transfer function of a BVD circuit with respect to frequency. On the resonance, the current through LCR branch flows in phase with the voltage. The current through the parallel capacitance has a phase shift of 90 degrees and causes a small phase shift of the total current. The maxima in the transfer function graph represent the resonance frequency of the LCR branch. However, the admittance of C_0 is small compared to the admittance of the LCR branch. The parallel capacitance leads to the typical minimum in admittance shortly after the maxima.

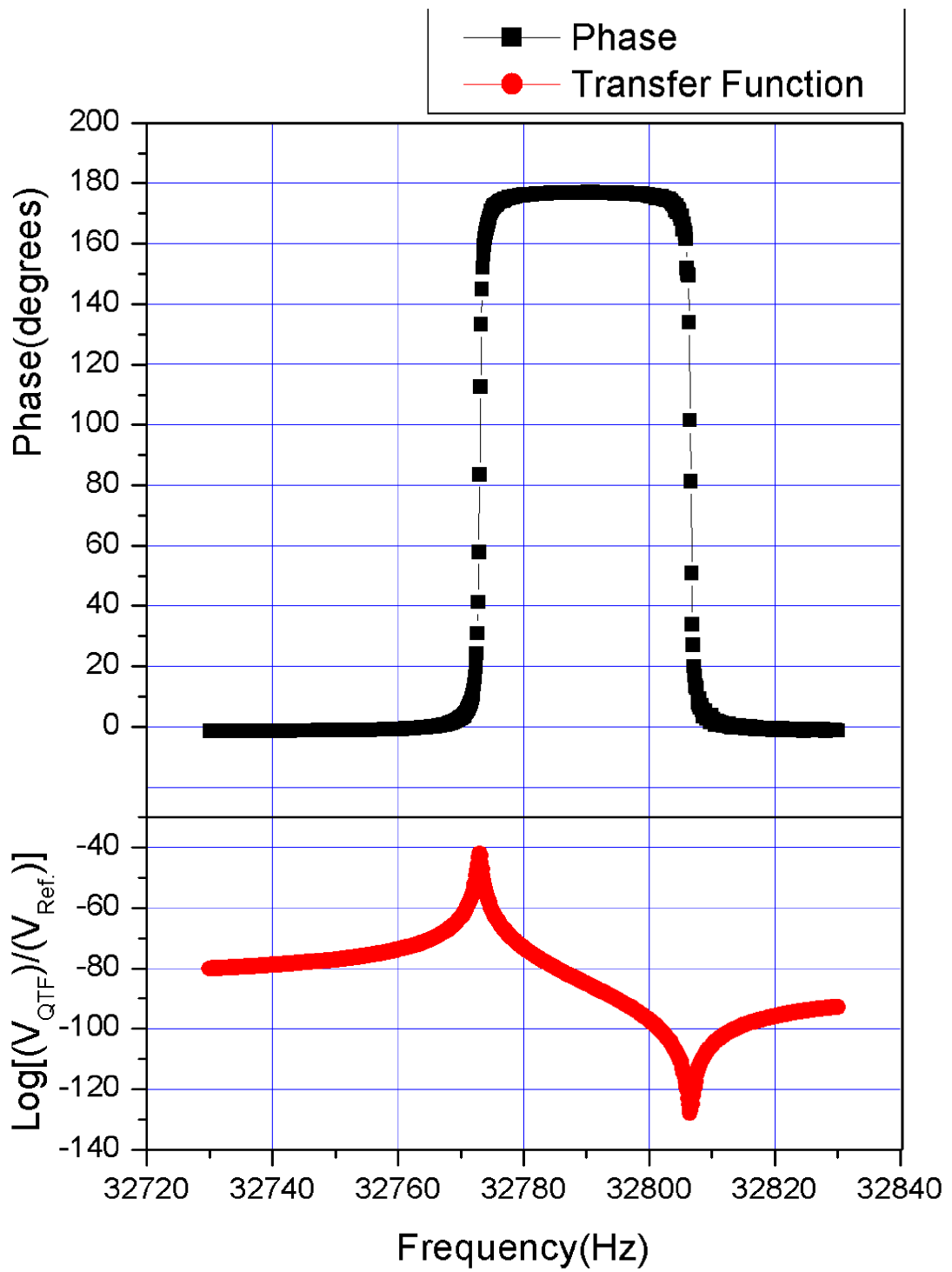


Figure 29: Transfer function of Butterworth-Van-Dyke filter.

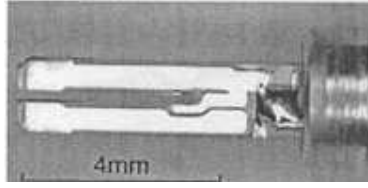


Figure 30: The NC26 quartz tuning fork after removing the aluminium casing.

4.1.5 Low temperature effect

To calculate the effect of temperature on resonance frequency we assume that the fluid in which the cantilever is vibrating obeys the ideal gas law. The density of fluid is inversely proportional to temperature when the pressure is kept constant; therefore from Eq. (95), $-\Delta f/f_0$ will also be inversely proportional to temperature, T .

$$\frac{\Delta f}{f_0} \propto \frac{1}{T}. \quad (102)$$

4.2 Setup for calibration of QTF

It was noted in the previous section that by knowing the effective mass of the QTF we can find the force acting on the sensor. This section explains the experimental setup used to determine the effective mass of the tuning fork. First, we describe the type of QTFs we used and the method used for sample preparation. The next section describes the uncertainty in resonance frequency of QTF due to manufacturing process. We then selected one of the samples and glued one of the prongs of QTF to a ceramic substrate. Next, we explain the effect of gluing the prong on $-\Delta f/f_0$. The results of this experiment were used to determine the effective mass of the QTF. We added measured mass on the vibrating prong and measured $-\Delta f/f_0$; and using the effective mass, we verified our experimental results.

4.2.1 Sample preparation

A QTF model NC26 from Fox Electronics was used for the experiment. These QTFs are available for the watch industry and are enclosed in aluminum cases. Also the QTFs have the resonance frequency of $2^{15} = 32768$ Hz. We designed twelve samples of QTFs by carefully removing their cases. To remove the case, we fixed the QTF between the jaws of a rotating drill and gently touched the case of the QTF with a very sharp blade. The pressure on the blade was kept constant so that it cut the aluminium uniformly. Eventually the aluminium was cut off, leaving behind the QTF, as shown in Fig. 30. Special care was taken not to damage the prongs. We did not want to mix different samples, and so we numbered the QTF samples as Sample#1, Sample#2, and so on.

4.2.2 Frequency measurement

We used the Stanford Research Systems model SR780 two-channel network signal analyzer for our measurements. The analyzer is configured to measure admittance in one window and phase in other. (Details of the configurations are given in Appendix A of this thesis.) Using `Labview` program, we measured the data in tabular form and transferred them to a computer hard disc. We fitted the data for admittance plots to the transfer function of Butterworth Vandyke filter to find the values of equivalent resistance R , capacitance C , inductance L , and stray capacitance C_0 . Using these parameters, we obtained the values of $-\Delta f/f_0$ and the quality factor. We verified both of these values using the parameters R , C , L , and C_0 obtained from equivalent phase plots. We studied the $-\Delta f/f_0$ and the quality factor of the QTFs in pressure range from 10^{-6} bar to room pressure. Here, the value for f_0 is the resonance frequency at 10^{-6} bar.

4.2.3 Tip Preparation

The tips for the force sensor were prepared by a double lamella drop-off etching technique (Fig. 31). In this technique the tip is prepared in a 2M NaOH solution at a dc voltage of 2-3 V. The etching apparatus consists of a metal plate with a centered hole of 3 mm diameter. The wire is threaded through the hole, and the upper end is glued to the QTF. The lower end is dipped in a conducting cup filled with electrolyte. A drop of freshly prepared NaOH solution is placed in the hole so that the solution fills the cavity and is not overflowing on the bottom or top of the stainless steel plates. Positive dc voltage is connected to the cup (cathode) and negative pole is connected to the metal plate with the hole (anode). Etching occurs at the portion of the wire that is encircled by the metal plate. When the wire becomes thin, the lower part of the wire falls down and at this moment, the current switches to zero. No circuit breaker is needed, and no more etching is done at the upper part of the tungsten wire, which serves as the tip. Once the tip is etched the assembly is rinsed with distilled water, and the tip is checked with an optical microscope. The alignment of the tungsten wire has to be very carefully adjusted through the center of the hole of the electrode to avoid lateral forces caused by surface tension. The etching height is set so that the tuning fork does not touch the top stainless steel cup, and far more importantly, no epoxy on the tungsten wire will be immersed in the solution. The silver in the epoxy will severely affect the electrochemical reaction and adversely influence the etching of the tungsten. Fig. 31 shows the setup to prepare the STM tips. The right figure shows the voltage and current variation with time during the etching process.

We then add point masses of order 10^{-7} kgs on the tip of the tuning fork prong and study $-\Delta f/f_0$. Then, we use this value to determine the mass added to the QTF. This experimental value is compared to the known added mass, hence the calibration is verified. Using the calculated value of ρ_c and measured $-\Delta f/f_0$, we calculated the added mass on the tuning fork and compared it with the known value of added mass.

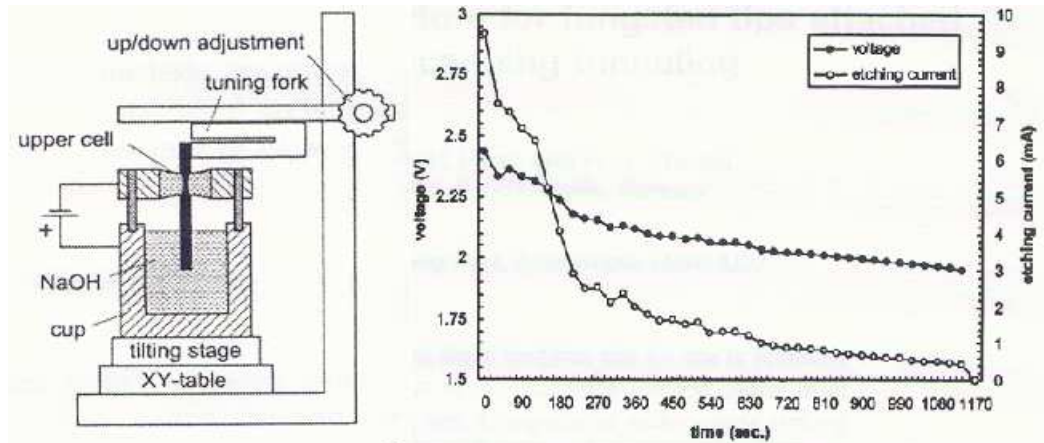


Figure 31: Left: Tip preparation using double lamella drop-off etching technique. Right: Voltage-Current variation with time during the electrolysis.

4.3 Results

In this section we present several results obtained during the calibration procedure. Since we start with more than one sample of QTF, we prove that even if the individual samples have different frequencies, $-\Delta f/f_0$ is indifferent. Next, we study the effect of adding a substrate on one of the prong of QTF because, in our experimental design, we plan to use the freely vibrating prong as a cantilever. Another interesting observation found during the calibration process was the effect of gravity. The effect of low temperatures was also verified before we attached the tip to our sample QTFs. Finally, we conclude the calibration section with a comparison between the value of attached mass as measured using a weigh machine and the value obtained from our calibration method.

4.3.1 Sample effect on resonance frequency

We studied the effect of different QTF samples on $-\Delta f/f_0$. Fig. 32 shows the study for four different QTFs. To present the range of data for pressure in a more manageable way, $-\Delta f/f_0$ is plotted with respect to pressure on a logarithmic scale.

This plot gives more details about change in $-\Delta f/f_0$ at low pressures. The graphs show that $-\Delta f/f_0$ is invariant to sample. Although the resonance frequency for each sample can be different, but $-\Delta f/f_0$ is the same. We are worked in a high pressure region, but even at low pressures, the effect remains the same. The different curves lie on the top of each other, and the error is within the resolution of the instrument 3×10^{-6} . Additionally, it should be noted that, at room temperature and pressure, these force sensors in air have a noise floor of $0.62pN/\sqrt{Hz}$ [61]. However, this noise can be ignored because the forces we are measuring here are of much higher magnitude.

4.3.2 QTF and cantilever

We glued one prong of the fork to the ceramic substrate [62]. This setup is like a cantilever, since the other prong is free to vibrate. Gluing one prong to a substrate is also equivalent to adding extra mass on one of the prongs, thus $-\Delta f/f_0$ was expected to reduce by a factor given by Eq. (100). To verify this hypothesis, $-\Delta f/f_0$ was measured the same way as before and plotted with respect to pressure, as shown in Fig. 33. The logarithmic graph plots the wider range for pressure indicating a decrease followed by increase in $-\Delta f/f_0$ when the pressure is continuously reduced. Also at high pressures the magnitude of $-\Delta f/f_0$ scales down. This can be explained by the Eq. (99) that says adding an external mass on the QTF will decrease the above magnitude by a factor proportional to the mass. Further, we can choose a conducting epoxy to measure a tunneling current in a way similar to that in a scanning tunneling microscope.

To determine the proportionality constants that relate the pressure calibration with the external force, we obtained the data for helium gas density and viscosity at pressure range from 0.1 to 1 bar [63]. Using the calliper we measured the dimensions of QTF and used the values, $L = 3.00$ mm, $b = 0.33$ mm, and $h = 0.40$ mm for

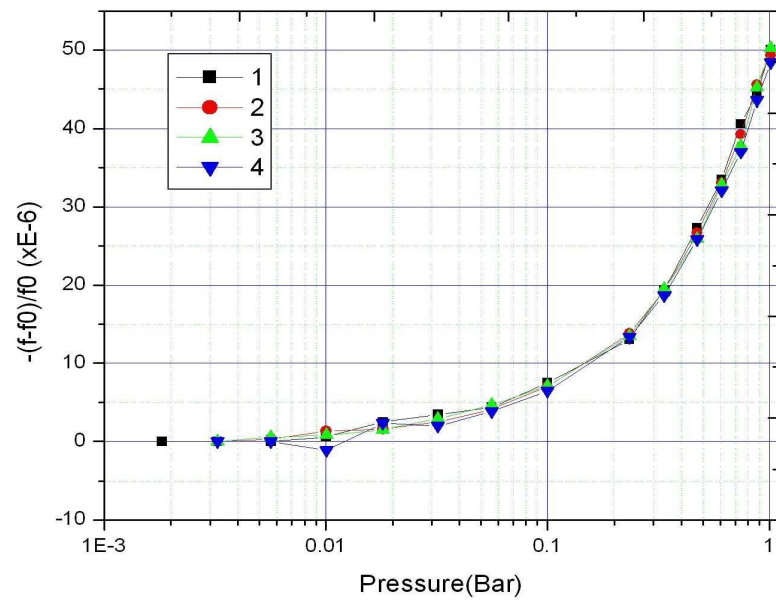
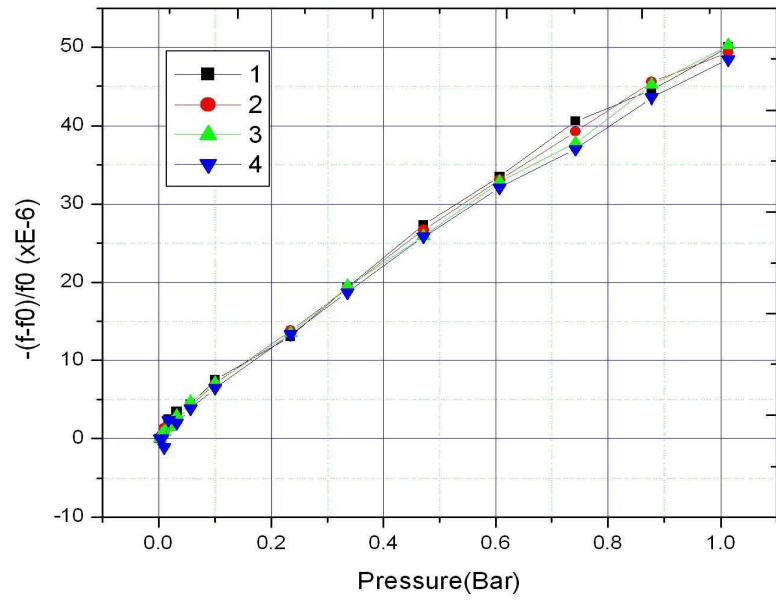


Figure 32: The graphs display the pressure on linear (top) and log (bottom) scale variation of $-\Delta f/f_0$ with pressure for four QTFs.

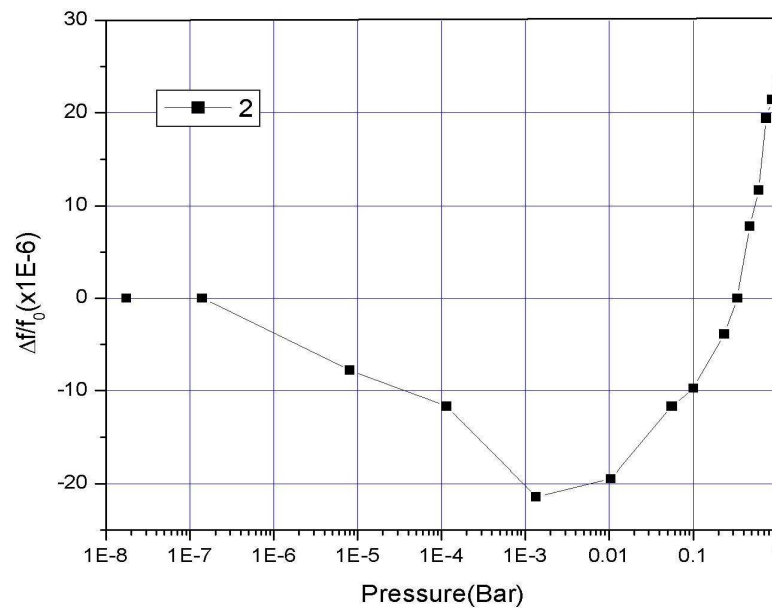
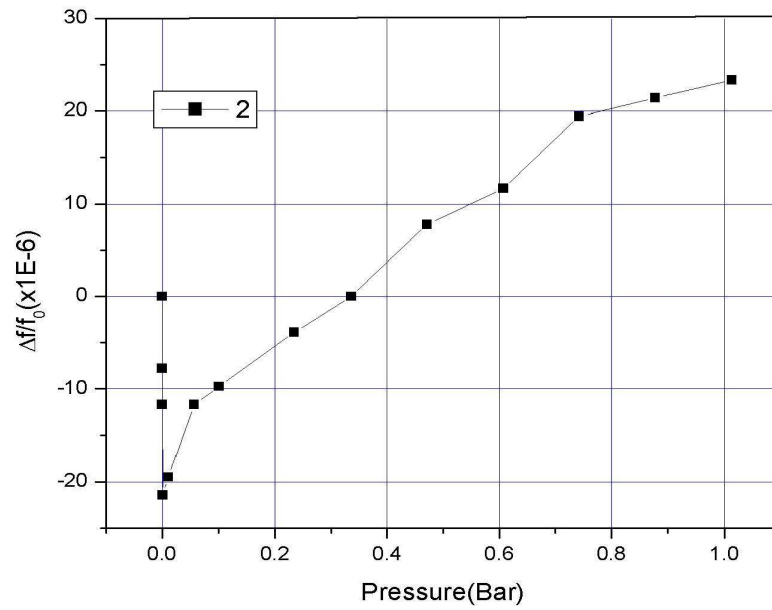


Figure 33: To design an equivalent cantilever, we glued one of the prongs of QTF on a substrate. This modifies the tuning fork and consequently the measurements of $-\Delta f/f_0$ vs. pressure changes.

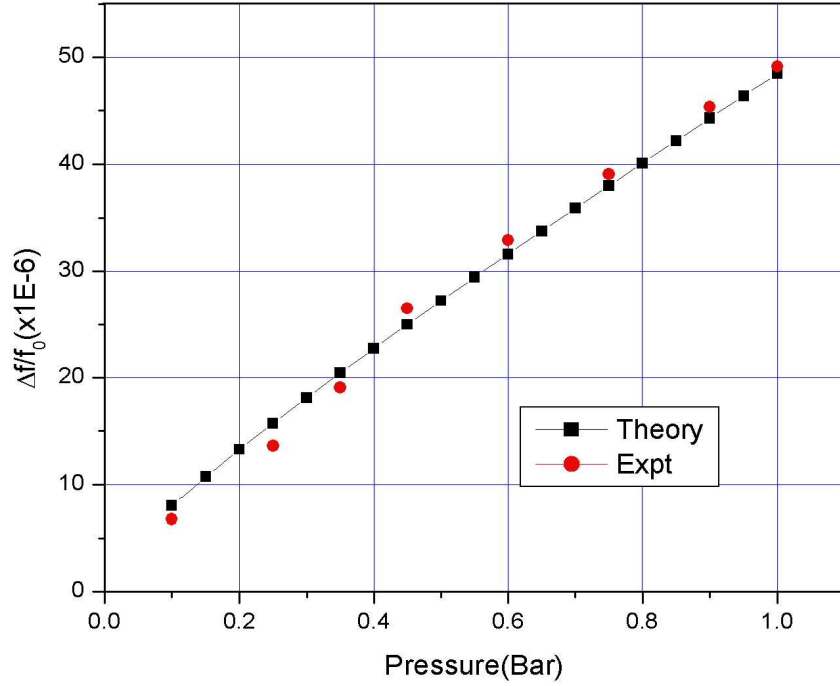


Figure 34: Theoretical and experimental comparison of $-\Delta f/f_0$ vs. pressure. We adjusted the effective density, ρ_c of QTF in the theoretical model to fit it with the experimental plot. The plot here gives $\rho_c = 1525\text{Kg/m}^3$.

the length, width, and height, respectively. Then we plotted Eq. (94) to obtain the theoretical graph for the vibration of a prismatic cantilever in a fluid. It should be noted that we plotted the theoretical graph between $-\Delta f/f_0$ and pressure, where the ideal gas law was used to relate the corresponding density of helium gas with pressure. We compared this graph with the experimental observations graph and adjusted the effective density, ρ_c of QTF, to fit the experimental graph shown in Fig. 34. We obtained $\rho_c = 1525\text{Kg/m}^3$, which gives $m_0 = 6.04 \times 10^{-4}$ gms. To verify the calibration we show that the added mass on the tip agrees with our calibration of $-\Delta f/f_0$. In the Table 1 we show the comparison of added mass to mass calculated

Table 1: Resonance Frequency at Room Pressure for QTF after addition of different masses.

Mass (gms)	Resonance Frequency(Hz)	$\Delta f = f_0 - f^1$ (Hz)	Calculated Mass (gms)
0.0001	27314.00	4811.56	0.0001178
0.0002	22550.75	9574.81	0.0002344
0.0004	19414.44	12711.12	0.0003122

using $-\Delta f/f_0$. Here f_0 is the resonance frequency without any added mass. The corresponding change in the resonance frequency due to each additional glued mass is plotted in Fig. 35.

4.3.3 Gravity effect

We also studied the effect of gravity on the fork. Fig. 36 shows that there is significant difference in the resonance frequency of the QTF depending on whether the the fork is aligned vertically or horizontally relative to the direction of gravity. In Fig. 37 we show the corresponding vertical and horizontal alignment of the vibrating prong relative to direction of gravitational force. Shift in resonance frequency increases by as much as three times when both prongs are vibrating parallel to gravitational force. With the addition of extra mass on the prong, the effect of gravity becomes increasingly prominent. This affect can be explained easily by the fact that when the prongs are parallel to gravity, the added mass will effect the resonance frequency. The gravitational force affects this mode of vibration. But when the gravitational force is perpendicular to the vibrating prongs, the mode of vibration of prongs is not affected by the force acting on prongs due to gravity.

4.3.4 Low temperature effect

Finally we studied the effect of low temperature on the shift in resonance frequency. Thus, we reduced the temperature to 77 K using liquid nitrogen. Fig. 38 shows that the slope of graph of $-\Delta f/f_0$ vs. pressure changes by a factor of 3.8. The change in the slope can be explained directly by the change in density of helium gas due

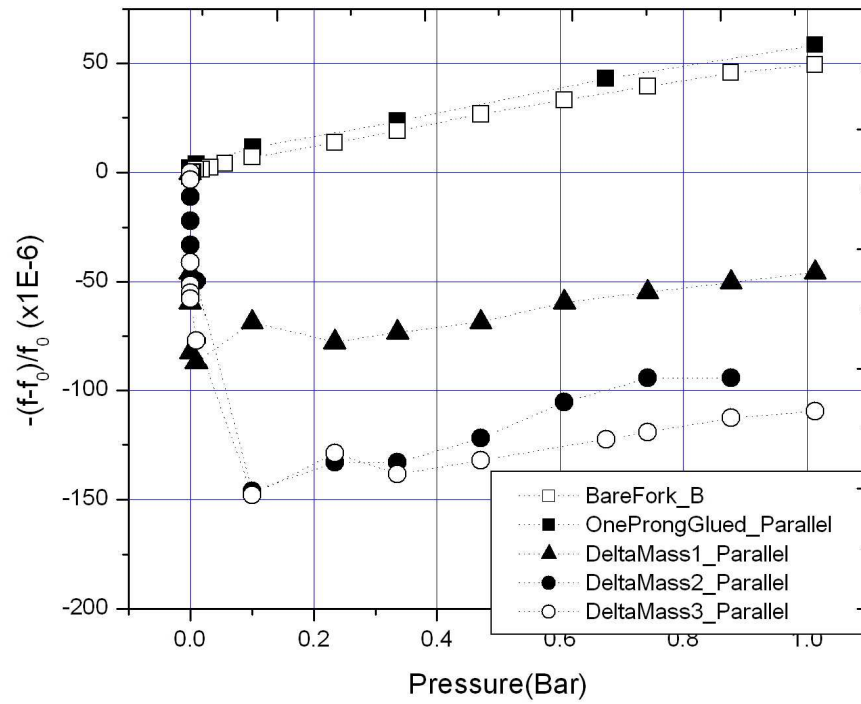


Figure 35: To verify the calibration we glued test masses on the vibrating prong and this graph displays that the changes in $-\Delta f/f_0$ are in agreement with the proposed theoretical model.

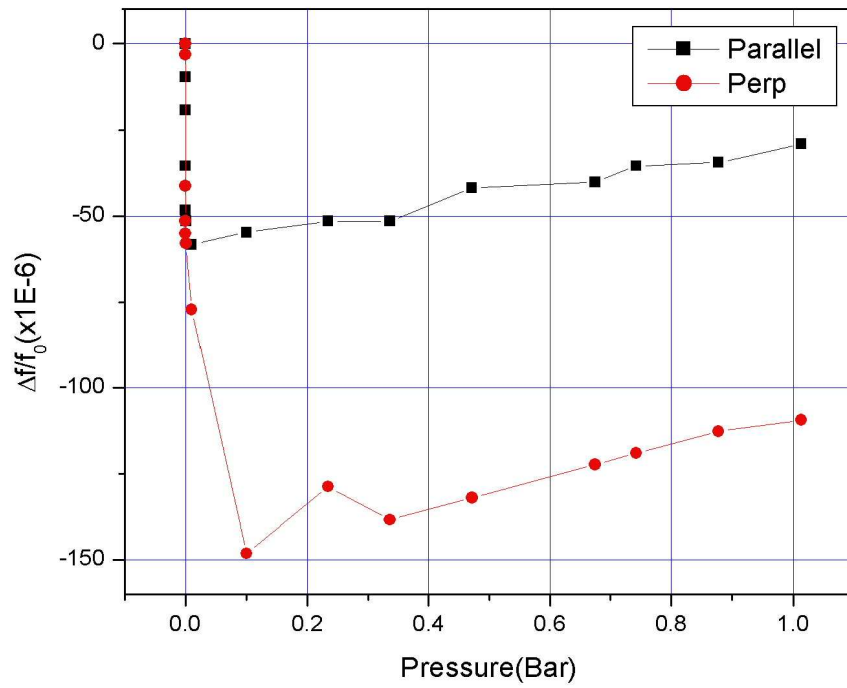


Figure 36: Variations in frequency due to parallel and perpendicular alignment of the QTF after three additional pieces of small masses are attached on the tip. $-\Delta f/f_0$ increases by as much as three times when both prongs are vibrating parallel to gravitational force.

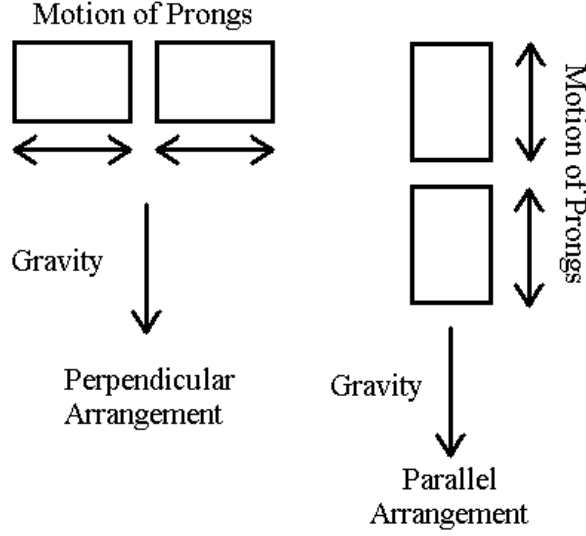


Figure 37: Parallel and perpendicular arrangements of the QTF prongs with respect to gravity.

to change in temperature. When the temperature drops to that of liquid nitrogen, the density of helium gas increases which decreases the resonance frequency of the QTF. As a result of decrease in resonance frequency, $-\Delta f/f_0$ increases by the same factor we used to decrease the temperature. Thus, the observed result is in agreement with the proposed theoretical model given by Eq. (102) in the theory section of this chapter.

4.4 *Experimental Setup*

In this section we describe a detailed setup for our experiments to measure the physical and electrical properties of the niobium nanowire. The setup is similar to a basic setup of a scanning tunnelling microscope, and the idea is taken from the setup developed by Müller [65]. We start with the isolation system developed to make our system indifferent to the vibration of the environment, which includes the building, floor or any other vibration source. Next we build up the electronics to amplify the nano-amperes current to a value measurable by commercially available instruments. Then

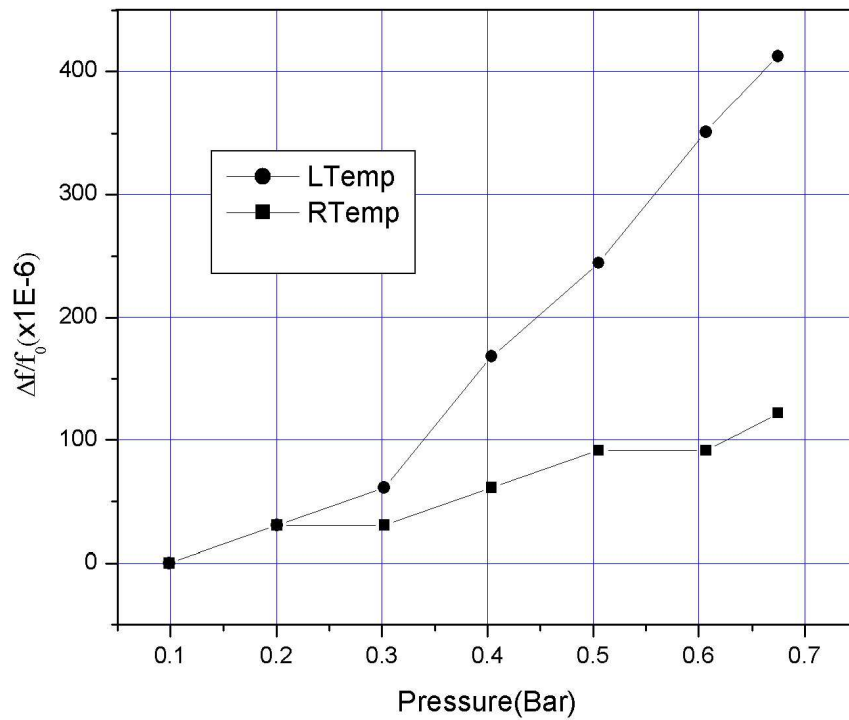


Figure 38: Low temperature measurements are compared with the room temperature results. The slope increases because the decrease in temperature increases the density of helium gas that increases the corresponding shift in resonance frequency.

we develop the mechanics for the sample to approach the vibrating prong (cantilever) of the QTF. This includes the coarse approach using a step-up motor and later the fine approach using the piezo crystals.

4.4.1 Vibration isolation

The basic idea of vibration isolation is to make the internal resonance frequencies of the entire experimental setup very high and to mount it on a support with a very low resonance frequency. The support will follow only the low-frequency building vibrations and suppress most of the high-frequency components. The experiment in turn will not be disturbed by the remaining low-frequency vibrations, because they do not introduce any internal motions into the setup (it just moves as a whole). Typical frequencies that can effect the experiment are:

- 1 Hz building vibrations due to people walking around, etc.
- 10-100 Hz building vibrations due to ventilation, appliances, etc.
- 1-10 kHz lowest internal resonance of typical mechanics of the setup.

The quality of vibration isolation also depends on the spectral distribution of building vibrations and on the lowest resonance frequency of the mechanical setup. Popular vibration isolation systems used for scanning tunneling microscopes mainly use one of the following methods:

- Air support tables which include heavy plate resting on inflated supports, possibly with active regulation to maintain constant height. These tables are nice because they give a large, steady work surface, but they are expensive and bulky.
- A stack of steel plates (typically about 1 cm thick), with rubbery material in between them is quite efficient. Although the elastic material is quite stiff and the resonance frequencies of the individual stages are quite high, the supported mass decreases from bottom to top, which generates multiple stages of damping resonance frequency.
- “Pendulum” method includes massive blocks suspended by springs, rubber bands,

or elastic tubing. This method of vibration isolation is inexpensive and simple to build. However this method may need some damping (e.g. damping from internal friction of the suspension) to avoid oscillations at resonance. It is easy to achieve very low resonance frequencies by combining a large mass with a soft suspension and that is why we have used this method for vibration isolation of our system. The following formulation gives a brief explanation of the mechanism.

If a block of mass, m , is suspended by a spring of spring constant, k , and length, L , the resonance frequency for vertical and lateral motion will be,

$$f_{vertical} = \frac{1}{2\pi} \sqrt{k/m} \quad (103)$$

$$f_{lateral} = \frac{1}{2\pi} \sqrt{g/L}, \quad (104)$$

where the gravitational acceleration, $g = 9.81 \text{ m/s}^2$. Again if the mass, m , is attached to the suspended spring, the spring will lengthen by a distance $d = mg/k$. This can be substituted into Eq. 103 to give,

$$f_{vertical} = \frac{1}{2\pi} \sqrt{g/d}. \quad (105)$$

Therefore, the oscillation frequency can be simply estimated from the distance the spring stretches when the load is attached. Typically, a resonance frequency of 1 Hz will result via an extension of 25 cm under a load that can be achieved by combining a huge mass with a strong spring or a smaller mass with a soft spring. Results really should be the same, as long as the mass used is a rigid block with high internal resonance frequencies. The lateral resonance frequency will automatically be lower than the vertical one, since $L > d$ is always true once the mass is attached. We implemented this mechanism using two rubber cords with a fastener from which we hang the support. The entire experimental setup was placed on this support, and it provided sufficient mass to damp the undesired vibration.

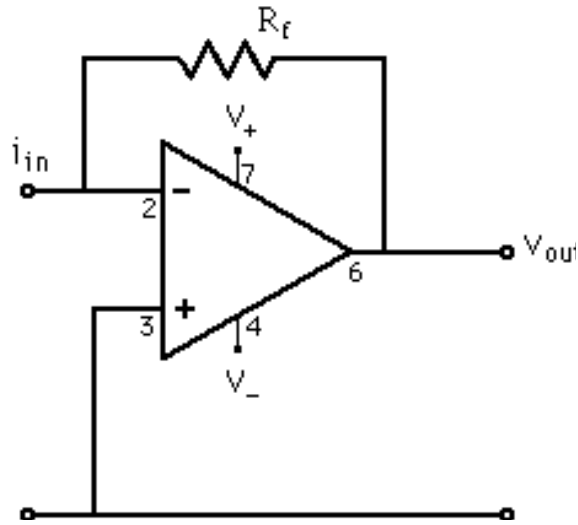


Figure 39: Current to voltage amplifier circuit.

4.4.2 Tunneling current amplifier

The following section focuses on the amplifier that converts the small tunneling current to a measurable voltage. The requirements for the current amplifier are simple enough: convert the small tunneling current to a voltage that can be handled comfortably, and do it as fast as possible to allow for fast Z height tracking and fast scanning. Typical tunneling current setpoints are of the order of 1 nA. To allow flexibility for higher setpoints and leave some headroom in case the tip comes closer to the sample than desired, tunneling currents of about 100 nA should be handled without overflows. Some applications require tunneling currents as low as a few pA, but that means very high amplification. The current amplifier is located on the STM scanning head (right next to the tunneling junction itself). We have used a double staged current to voltage amplifier circuit for converting small current signals (0.01 microamps) to a more easily measured proportional voltage. Using the current rule for opamps, i.e., the inputs draw no current, we have $V_{out} = -I_{in}R_f$.

- A1 = LF356 (Operational Amplifier)

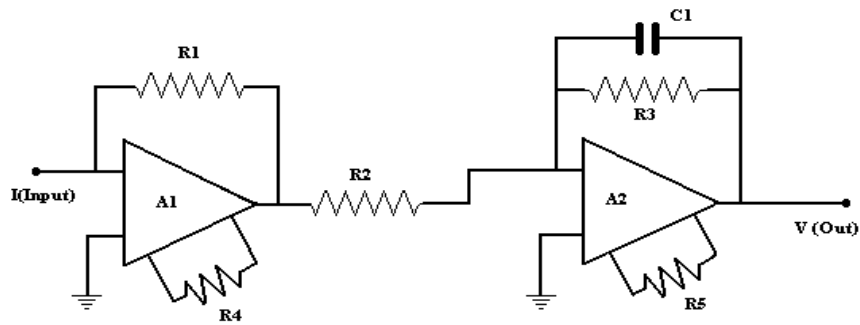


Figure 40: Operational amplifier circuit to convert small current to measurable voltage.

- A2 = LF356 (Operational Amplifier)
- C1 = $0.022\mu\text{F}$
- R1 = $100\text{K}\Omega$
- R2 = $1\text{K}\Omega$
- R3 = $1\text{M}\Omega$
- R4 = $20\text{K}\Omega$ (Variable Resistor)
- R5 = $20\text{K}\Omega$ (Variable Resistor)

LF356s are operational amplifiers produced by National Semiconductors. These are monolithic JFET input operational amplifiers that incorporate well matched, high voltage JFETs on the same chip with standard bipolar transistors. These amplifiers feature low input bias and offset currents/low offset voltage and offset voltage drift, coupled with offset adjustment that does not degrade drift or common-mode rejection. The devices are also designed for high slew rate, wide bandwidth, extremely fast settling time, low voltage and current noise, and a low $1/f$ noise corner.

4.4.3 Approach mechanism

The following section describes the mechanics used to control the motion of the tip while it approaches the sample. Besides the fact that we are working with the length scales of the order of nanometers or less, another factor that is considered while designing the system is the stability of the tip and sample system. Therefore, we used the tripod system of precession screws and the stepper motor for coarse approach mechanics and the piezo stack actuators for the fine approach. The sample was fixed on the base while the tip was fixed on the head that moved closer to sample using the coarse and fine approach mechanics. The following paragraphs give the separate details of each of these mechanics.

Coarse approach: A straightforward mechanism is to use a micrometer-resolution precision screw, in addition to the differential springs, consisting of a soft spring, which is compressed by a screw, and in turn pushes against a very strong spring supporting either the sample or the tip. However, we avoided the spring system and used a mechanical tripod shown in Fig. 41 for the coarse approach. The mechanical setup is simple: both the head and the base consist of single blocks. The head rests on three supports that are the ball-shaped tips of precision screws. The piezo scanning system is mounted on the head. In particular, the piezo scanning system is glued to a removable piece that is attached to the head with a screw. The sample is attached to the base by scotch tape, which is not shown in the figure. The two precision screws in front, next to the piezo system, have knurled knobs for manual operation. Turning these screws will change the tip to sample distance by nearly the same distance that the screw is moved. Since sample surfaces are very smooth and a reflection of the approaching tip can be seen on the surface, the coarse approach using these screws usually is done manually, under visual control using an optical microscope.

Precession screw with stepper motor: Motion of the third support screw in the back, however, is reduced by a factor of about 15. Since the piezo tip is quite

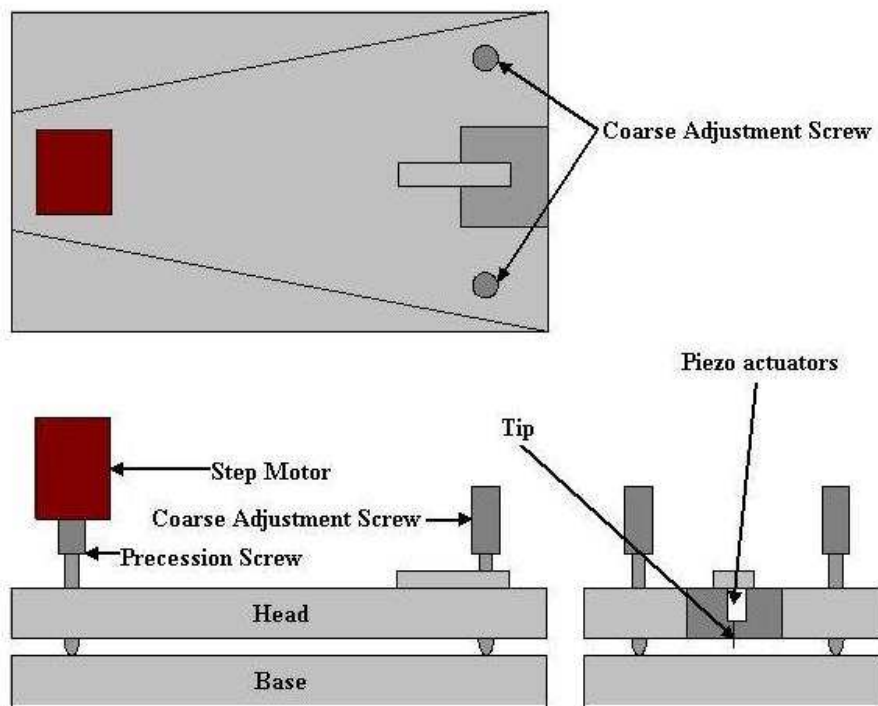


Figure 41: Approach mechanics design displaying the base, head, and three screws. The step motor controls the fine adjustment screw. The piezo actuators control the precise approach of the tip to sample.



Figure 42: Step motor used to drive the precession screw automatically. The motor can be integrated with a computer to program the steps needed for the tip-sample approach.

close (≈ 1 cm) to the line connecting the other two supports and the third screw is 15 cm away from this line, the whole head acts as a lever. Also the travel of the original precision screw is limited typically to a few millimeters; so the range of approach using this screw is of the order of a few tens of microns. Additionally, the precession screw is driven automatically by a stepper motor to eliminate the tedium of a manual approach and the vibrations introduced by touching the instrument. So we used a Lin Engineering integrated motor, shown in Fig. 42, to control the motion of the screw. This motor can be programmed using Labview, and an appropriate feedback loop can be set for the desired approach mechanics of the tip. Next, using a coupler we connect the precession screw to the motor. However, the axis of motor shaft and the screw require a very precise alignment, and the coupler could not provide sufficient precession.

Piezo approach: Piezo elements are apparently used universally to produce the small motions (on the nanometer scale) of the tip in scanning probe and atomic force microscopy. Piezoelectric materials - most notably some types of ceramics that have been polarized by letting them cool down in the presence of an electric field - exhibit a mechanical deformation when a voltage is applied across them. The exact amount of deformation depends on the material and its geometry. Typically, excursions of a few nanometer/Volt may be obtained from handy piezo elements, say 1 inch in length. Among the different available geometries, piezo stack actuators shown in Fig.



Figure 43: Piezo stack actuator used for the X/Y scanning motion and for the Z height tracking.

43 were used for the fine approach mechanism. These actuators are manufactured by piling up a quantity of piezoelectric discs or plates, which are individually contacted electrically. The stack axis is the axis of the linear motion: the thickness of the layers increases by applying a voltage and thereby the total stack lengthens. We glued three actuators for the X/Y scanning motion and for the Z height tracking. The applied voltage across the piezo actuators is controlled by the Thorlabs 3-D axis piezo controller. Again this controller can be integrated with the computer to setup the feedback loop.

Finally, the feedback loop can be programmed using the proportional, integral, and differential controllers such that at each step of the loop we check the tunneling current. For zero values of this current, we rotate the step motor to rotate the precession screw then change the voltage of the Z axis piezo actuator so that the stacks elongate and tip moves closer to sample. The tunneling current is measured again and the loop continues until we achieve a non-zero current, which indicate that the tip is close enough to the sample to continue with the experiment.

4.4.4 Phase-locked loop

Having the approach mechanics similar to a STM setup, in our quest to measure the force on the nanowire, we now need a continuous frequency tracking system. As

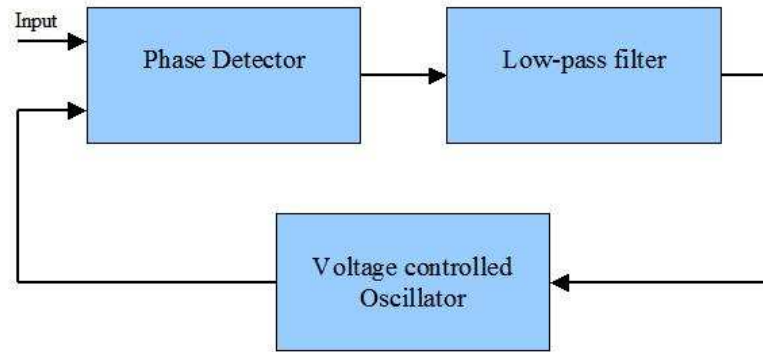


Figure 44: Block diagram of a phase-locked loop circuit used to track the frequency that is changing with the applied force on the cantilever.

the tip is dipped in bulk material and then pulled back, the atoms will rearrange themselves such that they are in the minimum energy and the minimum force configuration. The continuous rearrangement will change the force continuously, which in turn will change the resonance frequency of the vibrating QTF. This change in frequency can be tracked by a simple electronic circuit, called a phase lock loop (PLL). The basic configuration of a PLL, as shown in Fig. 44, is a phase detector, a loop filter, and a voltage controlled oscillator (VCO). The phase detector compares the phase of the input signal with that of the VCO, and its output voltage is filtered and applied to the VCO whose output frequency moves in the direction so as to reduce the phase difference of the input signal and output of VCO. When the loop is “locked,” the frequency of the VCO is exactly equal to the average of the input signals. The entire circuit is commercially available on single microchips, like MC14046B from ON Semiconductor, and can be configured for the required frequency range. (Details of the configuration are given in Appendix C of this thesis). The VCO also gives a DC voltage that is directly proportional to the “locked” frequency. This voltage can be measured precisely and the required results can be observed. However, a more advanced version of the circuit called the Lock-in Amplifier is commercially available from the Stanford Research Systems. This amplifier can

be interfaced with the computer and therefore we used it for all frequency tracking measurements. Theoretically, this method of measuring the physical and electrical properties of nanowire should work, and it should be able to give observable results. However, a more sophisticated method was developed simultaneously that not only gave more accurate results but also was much easier to implement.

4.5 Mechanically Controllable Break Junctions [66, 67]

The method used the microfabrication facilities and is more commonly known as Mechanically Controllable Break Junctions (MCBJ). The essence of the MCBJ technique is the use of a bendable substrate which, when placed in a three point bending configuration, enables the length and, consequently, the width of the contact to be changed dynamically through piezoelectric actuation. Indeed, the MCBJ method allows complete control over the length of device region from that of a bulk contact to a single atom contact to a tunnel junction. However, not only do MCBJ have an extensive range of possible atomic configurations, but also they are naturally robust against mechanical vibrations, which implies that one can easily maintain single atom contacts for long periods of time. This combination of range and stability provide an ideal testbed for mesoscopic system physics. For the fabrication of mechanically controllable break junctions, the major design goal is to create a metallic structure whose smallest dimensions can be altered through elastic deformation of the underlying substrate; to that end, our design employs the technique of suspending a narrow metallic bridge between two contacts on a flexible substrate. Using this configuration, the width of the bridge can be precisely varied from hundreds of nanometers down to a single atom by bending the substrate with a mechanical actuator.

CHAPTER V

SQUEEZE-FILM EFFECT

In the presence of a compressible gas film, the moving surfaces of the two prongs of QTF squeeze the gas from between them. If the gas pressure is low, the molecular mean free path is comparable to the gap between the prongs, and the gas cannot be treated as a continuous medium. The gas at low pressure has an interesting effect on the frequency response of the QTF: above the cut-off frequency, the gas film is trapped and squeezed between the moving prongs and behaves like a low dissipation spring element; whereas below the cut-off frequency, the gas has enough time to flow out of the prong surfaces, thus causing significant dissipation. Figure 35 shows that $-\Delta f/f_0$ decreases with pressure and then increases again. The effect of decreasing and then increasing of $-\Delta f/f_0$ becomes more prominent after the addition of extra mass. Although a hypothesis is presented to explain this effect, a detailed theoretical model was beyond the scope of this thesis. Therefore, we use results derived from fluid flow in a viscous medium to develop the hypothesis. We start with the Reynold's equation, which is essentially the Navier-Stokes' equation in the presence of several constraints. The squeeze number is an important assumption for the derivation of this equation. Another important parameter is Knudsen's number, which defines the effective gas viscosity in different pressure ranges. Having the above definitions, we narrowed the pressure range to where this formalism is valid. For pressures outside this range, we develop a model involving the vibrating cantilever and the atoms of the fluid medium to explain the variation in frequency.

5.1 Theoretical background

We used the theory of squeeze-film effect to explain the strange frequency response QTF. In micromechanical systems when a cantilever is moving near a stationary surface in presence of a fluid, a squeeze-film damping effects the resonance frequency of the cantilever. As a plate moves perpendicularly towards a parallel surface a small distance away, the plate forces the fluid to be pushed out of the gap causing a damping force and compresses the fluid resulting in a spring force. The pressure gradient of gas between the body and the stationary surface is related to the velocity profiles in the x and y directions when the body is undergoing squeeze-film motion in z direction. The flow of fluid can be described by the Navier-Stokes' equation (Eq. (86)). However, for this particular system the following assumptions are made [68]:

- The gap height, ξ is always much smaller than the lateral extent of the moving body.
- The motion is sufficiently slow that the unsteadiness can be neglected.
- The gas obeys the ideal gas law.
- The system is isothermal with density proportional to pressure.

In particular, by assuming steady state conditions, $\frac{\partial \mathbf{u}}{\partial t} = 0$, and neglecting the inertial term, $\mathbf{u} \cdot \nabla \mathbf{u}$, we write the classical momentum equation for the film reduced from the Navier-Stokes' equation (Eq. (86)) as:

$$\frac{\partial p}{\partial \zeta} = \frac{\partial}{\partial z} \left(\eta \frac{\partial u_\zeta}{\partial z} \right), \quad (106)$$

where ζ represents the x and y coordinates, and $u_\zeta = u_\zeta(x, y, z)$ is the velocity field components (in x and y directions) as a function of the coordinates. Essentially the assumptions mentioned above can be written in a condensed format by considering the ratio of the inertial force per unit volume, $\rho u_\zeta (\partial u_\zeta / \partial \zeta)$, to the viscous force per unit volume, $\eta (\partial^2 u_\zeta / \partial z^2)$, which gives the applicability of Eq. (106). As shown in Ref. [69], the magnitude of the ratio can be approximated by a modified Reynold's

number, \mathbf{Re}^* ,

$$\frac{\rho \vartheta^2 \xi^2}{b \eta \vartheta} = \frac{\rho \omega b \xi^2}{\eta b} = \mathbf{Re}^*, \quad (107)$$

where $\vartheta = u_\zeta(x, y, 0)$ is the velocity of the driving surface (the velocity of the driving surface is considered identical in both x and y directions) and is given by the frequency of vibration times the dominant length scale, i.e., $\vartheta = \omega b$. It should be noted that the modified Reynold's number is dependent on the thickness of the film rather than on the cross section area of the vibrating cantilever. So the use of Eq. (106) instead of the complete Navier-Stokes' equation is justified if the ratio (modified Reynold's number) is such that $\mathbf{Re}^* \ll 1$, or in other words, the viscous force should be larger than the inertial force. For our analysis of the frequency response of QTFs, this ratio determines the upper bound of the pressure.

Now the momentum equation in Eq. (106) can be combined with the continuity equation,

$$\frac{\partial \rho}{\partial t} + \nabla \cdot (\rho \mathbf{u}) = 0, \quad (108)$$

to obtain a single differential equation relating the pressure, density, surface velocity, and film thickness. This differential equation is the well-known Reynold's equation for a thin fluid film between two moving surfaces. The combination of Eq. (106) and Eq. (108) allows the distributed film velocity, \mathbf{u} , to be eliminated and replaced by the film surface velocity, ϑ . It should be noted that the velocities of the adjacent bearing surfaces will be identical for a no slip condition. Next, the momentum equation (Eq. (106)) can be integrated to obtain the expressions for u_ζ . Then using these expressions from the continuity equation, Eq. (108), and integrating that equation gives the desired Reynold's equation,

$$\frac{\partial}{\partial x} \left(\frac{\rho \xi^3}{\eta} \frac{\partial p}{\partial x} \right) + \frac{\partial}{\partial y} \left(\frac{\rho \xi^3}{\eta} \frac{\partial p}{\partial y} \right) = 12 \frac{\partial}{\partial t} (\rho \xi). \quad (109)$$

The Reynold's equation can be written in condensed form by normalizing it such that

we make the following variable changes:

$$p = (1 - \bar{p}e^{\omega t})P_0, \quad (110)$$

$$\xi = \xi_0 + \bar{\xi}, \quad (111)$$

$$x = \bar{x}b, \quad (112)$$

$$y = \bar{y}b. \quad (113)$$

Here P_0 is the ambient pressure, ξ_0 gap's nominal height, and b is the width of the cantilever. Additionally, the local density of fluid, ρ , is directly proportional to the pressure, p , because we assume that the gas is ideal. Also, if the cantilever is vibrating with a frequency, ω , then the pressure is assumed to be an exponential function (defined in Eq. (110)) of that frequency. Further, Griffin, et al. [70], have assumed the time dependent gap's height, $\bar{\xi}(t)$, as a sudden or step change at time $t = 0$. All the above simplifications lead to the following form of Reynold's equation:

$$\frac{\partial^2 \bar{p}}{\partial \bar{x}^2} + \frac{\partial^2 \bar{p}}{\partial \bar{y}^2} = -\frac{12\eta b^2 \omega}{\xi_0^2 P_0} \bar{p}. \quad (114)$$

The constants on the right hand side of the equation are combined to define the squeeze number, σ as:

$$\sigma = \frac{12\eta b^2 \omega}{\xi_0^2 P_0}. \quad (115)$$

Additionally, Eq. (114) is an eigenvalue equation and its lowest eigenvalue will define the cut-off frequency, ω_c , that limits the lower bound of the pressure while analyzing the frequency response of the QTF:

$$\omega_c = \frac{\pi^2 \xi_0^2 P_0}{12\eta b^2}. \quad (116)$$

Thus, we have a pressure range whose upper bound is determined by the modified Reynold's number in Eq. (107), and the lower bound is determined by the cut-off frequency in Eq. (116).

In addition to the above formulation, Veijola et al. [71], used the Knudsen's number, K_n , that is the ratio of free mean path, λ to the gap height, and ξ_0 to define

the effective viscosity in the model for squeeze-film effect. Essentially, Veijola et al., have extended a model developed by Fukui et al. [72], who used the Boltzmann's transport equation to derive a modified Reynold's equation for arbitrary Knudsen numbers and expressed the effective viscosity in terms of Poiseuille flow rate. But the Poiseuille flow rate cannot be represented in closed form. So Veijola et al., derived a simple approximate equation that differs by less than 5% from the original equation that is valid for the Knudsen number's range given by, $0 \leq K_n \leq 880$. Therefore the approximation for the effective viscosity, η_{eff} , is given by:

$$\eta_{\text{eff}} = \frac{\eta}{1 + 9.638K_n^{1.159}}. \quad (117)$$

Having an expression for effective viscosity leads us to the range of Reynold's numbers in which the squeeze-film effect of Eq. (114) can be observed for the vibrating prongs of QTF.

The next step was to calculate the hydrodynamic function for this range of Reynold's numbers and analyze the change in frequency shift graph. So we solve Eq. (114), and get:

$$\bar{p}(\bar{x}, \bar{y}) = \bar{p}_0 \cos(\sqrt{\sigma_x} \bar{x}) \cos(\sqrt{\sigma_y} \bar{y}), \quad (118)$$

where the sum of σ_x and σ_y is equal to the squeeze number, σ . Next, we want the expression for effective pressure per unit length, which can be integrated over the cross section of the cantilever to obtain the force per unit length (as in Eq. (88)). Also in this equation the vorticity is not effected by the squeeze-film because the curl of the velocity fields, u_ζ , (u_ζ obtained by solving the momentum equation, Eq. (106)) gives a zero for z -component vorticity. Then, we expand Eq. (118) in Taylor's series and write the expression for real pressure per unit length using the pressure normalization equation defined in Eq. (110) and obtain

$$p = P_0 \left(\sigma_x \frac{x}{b} \right) e^{\omega t}. \quad (119)$$

This pressure is similar to the ambient pressure with an extra term, σ_x . The surface integration of this pressure will give an expression similar to Eq. (89), but now having the squeeze number in the force equation. Here, the significance of the squeeze number is that the viscous forces are much greater than the inertial forces. On simplification, we obtain the expression for resonance frequency as

$$\frac{\Delta f}{f_0} = -\Gamma(\omega) \frac{1}{2} \frac{\pi \sigma_x \rho b}{4 \rho_c h}. \quad (120)$$

Although this equation has several assumptions, we hypothesize that this model should explain the observed shift in resonance frequency.

5.2 Results and analysis

The above model is limited to a pressure range that is determined by the modified Reynold's number assumption in Eq. (114) and the cut-off frequency limit given by expression in Eq. (116). The first equation implies that the squeeze-film effect will be observed for pressures less than 0.1 bar, while the cut-off frequency or 32768 Hz limits the pressure to values greater than 10^{-4} bars. Having the lower and upper bounds of pressures, we calculated the effective viscosity, η_{eff} , using the Knudsen's number that was obtained using the mean free path and the thickness of the fluid film. Using 0.275 mm as the thickness of film as shown in Fig. 45 from Ref. [74] and 196 nm [73] for mean free path of helium gas at room temperature and pressure, we calculated the Knudsen's number that varies between 7.13×10^{-3} (for pressure = 0.1 bar) and 712.73 (for pressure = 10^{-6} bars). Therefore, the Knudsen's number for our system satisfies the criteria ($0 \leq K_n \leq 880$) stated in the theory. Next, we calculated the squeeze number in Eq. (115) and Reynold's number in Eq. (97) using the physical constants from Ref. [63]. We used the density of helium gas equal to 0.16040 kg/m³ and viscosity, η , at room temperature and pressure equal to 19.93×10^{-6} Pa.sec. The width of the cantilever was approximated to be 0.6 mm and the height was set to 0.5 mm. Thus the Reynold's number changed from 15.38 for (for pressure = 0.1

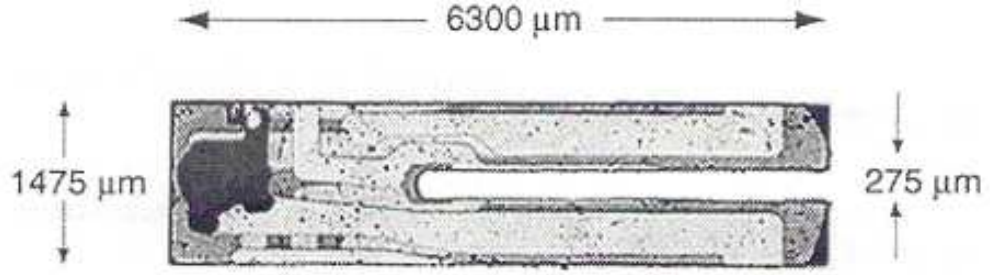


Figure 45: Dimensions of quartz tuning fork.

bar) to 2.91 (for pressure = 10^{-6} bars). Since the Reynold's number is small, we used the $Re \rightarrow 0$ approximation in Eq. (98) and obtained the graph shown in Fig. 48. Thus the hydrodynamic function varies from 1.72 to 3.79 for the corresponding pressures. With this we have all the parameters needed in Eq. (120), and we plotted the theoretical values of shift in resonance frequency and compared them with the observed values in Fig. 49.

The analysis of the graph shows that although the shift in resonance frequency follows the theoretical model, it does not explain completely the observed phenomena. A possible reason for the inconsistency is the number of approximations taken in the theoretical model. The effective viscosity in Eq. (117) is an empirical formula, and it can be changed to fit the experimental results. A possible formula can be generated by fitting an exponential decay function that is dependent on the Knudsen number. So the Eq. (117) can be modified to generate a new effective viscosity as follows:

$$\eta_{\text{eff}} = \frac{\eta}{1 + 0.471 + 0.164 \ln(K_n) + 0.017 [\ln(K_n)]^2}. \quad (121)$$

However, this force fitting of the viscosity lacks a physical explanation. Though, it gives a much better explanation of the observed results. We used the effective viscosity in Eq. (121) to plot the graph shown in Fig. 47.

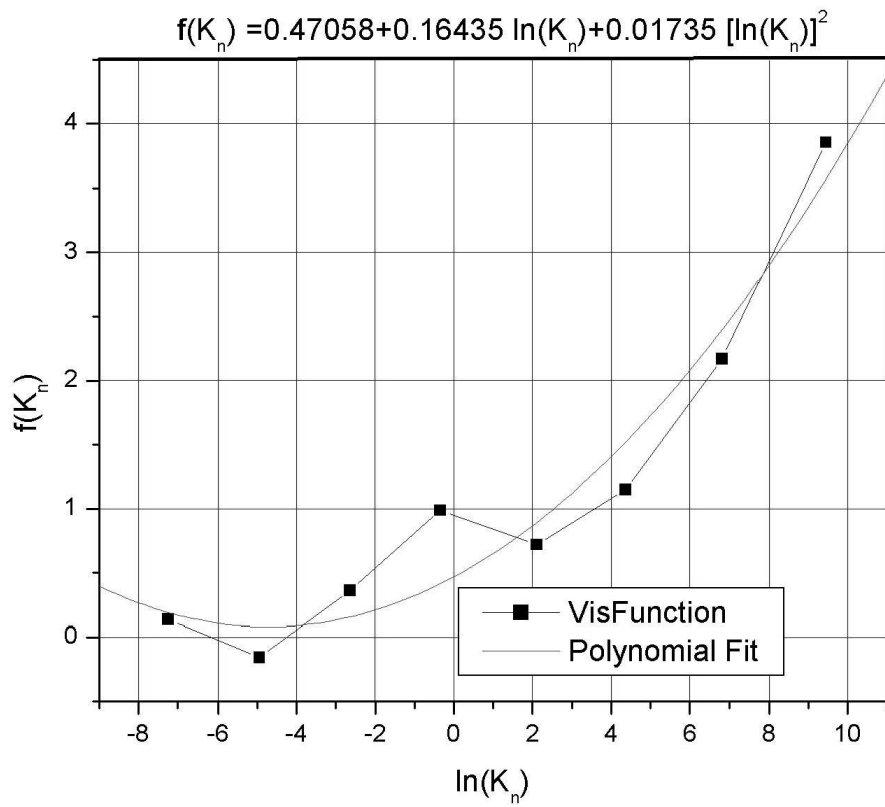


Figure 46: Polynomial fit of effective viscosity function to natural logarithm of Knudsen's number.

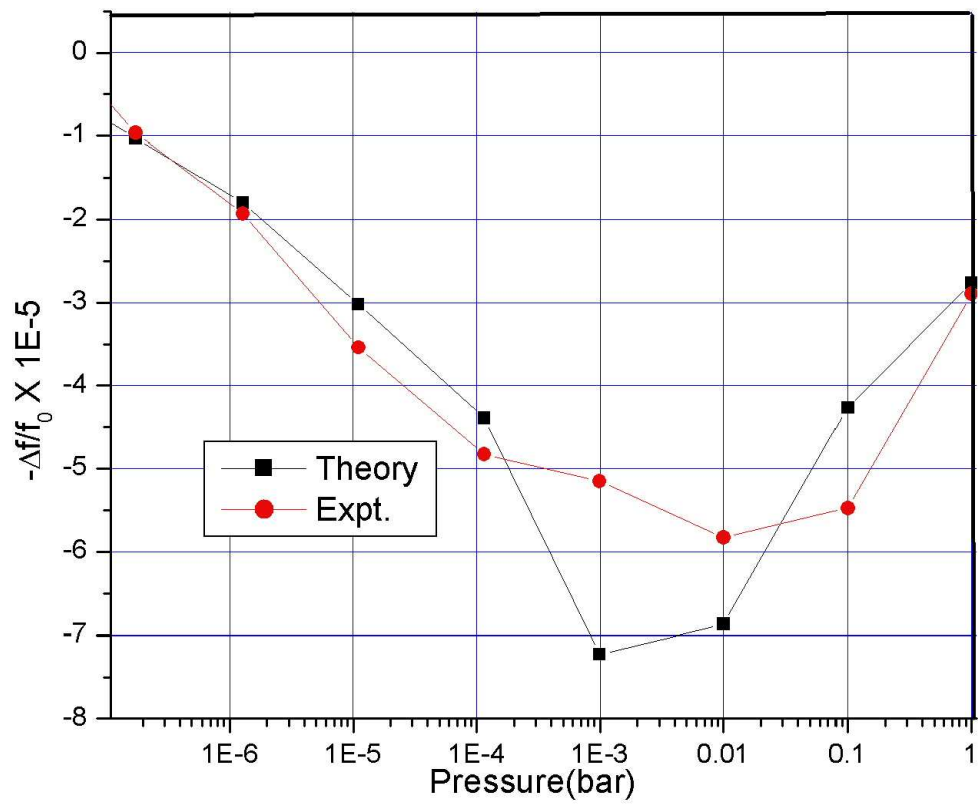


Figure 47: Theoretical model generated to fit the data.

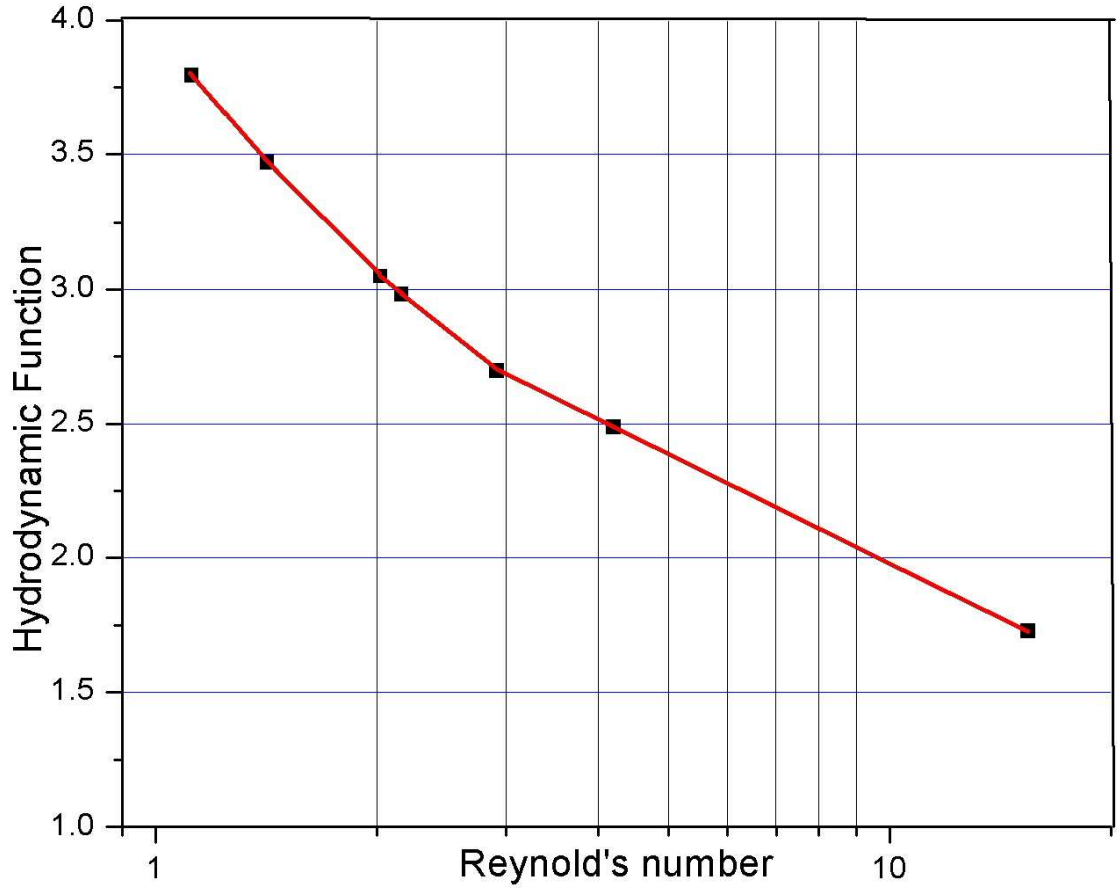


Figure 48: Hydrodynamic function plot for moving cylindrical cantilever in fluid.

Also a detailed finite-element, numerical model will give a better result for the hydrodynamic function, which can explain the differences. The complete simulation was beyond the scope of this thesis, therefore we leave it for future work. Further, Blech [75] has demonstrated that the damping force due to the squeeze-film is maximum at the cut-off frequency, which corresponds to the pressure of 10^{-4} bars in our system. Thus, for pressures below this critical value, we observe the decreased damping force and so $-\Delta f/f_0$ increases.

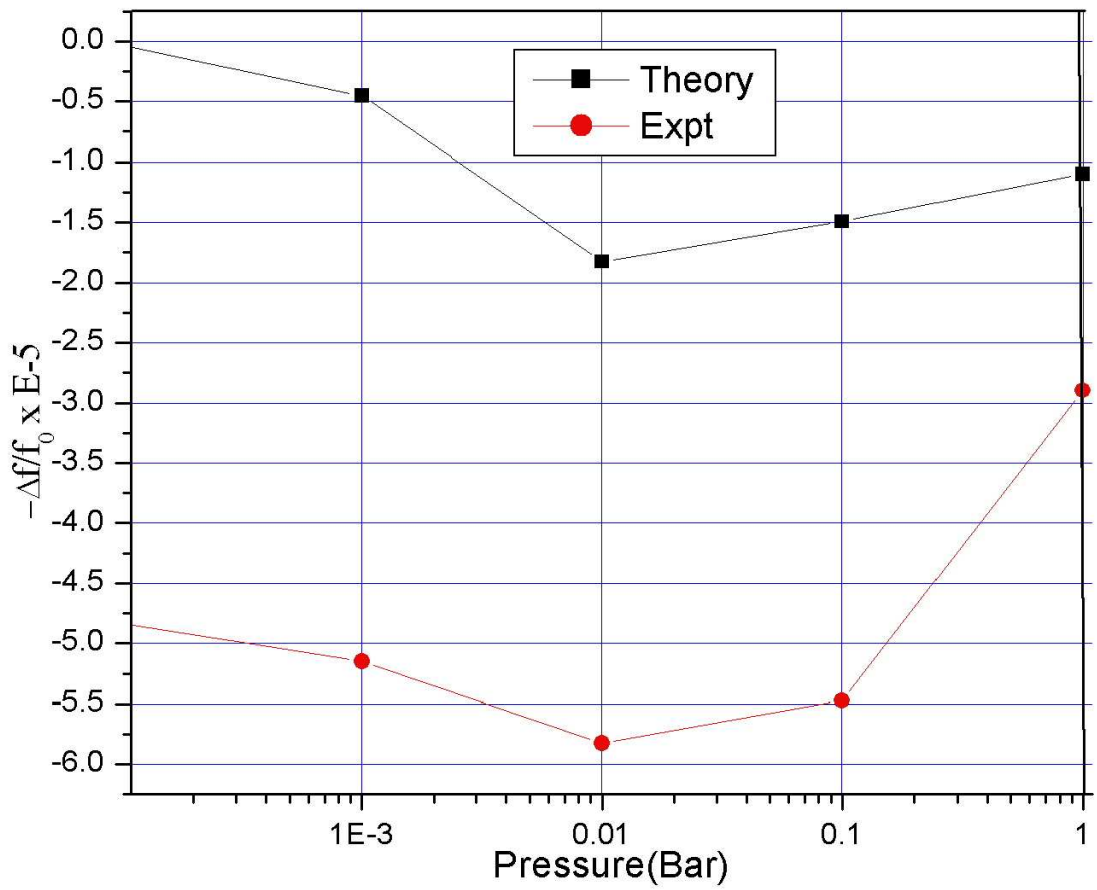


Figure 49: Squeeze-film effect in QTF sensors.

5.3 Conclusion

Presented in this dissertation is a detailed analysis of a simple problem. As can be seen, even a simple real life problem has a diverse range of complexity. We started with the structure calculation of a niobium wire, that involves only a few atoms. Different physical theories with several approximations were used to find the structure. We successfully calculated the structure on a desktop computer. Since the main advantage of the method presented for structure calculation is its lower requirement for computational power, more complex structures, including several atoms as in bio-molecules, can be simulated using the tools. Along with the structure calculation, we also analyzed the transport properties of nano-structures using the inexpensive computational resources. Therefore, this method presents hope for future research in a way that the many-body problem can be solved practically. Therefore, different fields of physics, chemistry, and biology can be studied in detail and this research can be considered a forward step in our pursuit of understanding nature.

Having the theoretical tools and models, we developed experimental methods and then moved towards the engineering implementations of methods to verify the above developed theory. We started with a simple quartz tuning fork and modified it to be a sensor. The sensor can have several practical applications in other research areas, but we focused on the verification of the theoretical results. During the development of the sensor, we studied different electronic tools available to process the data. Although, we tried to minimize my diversification and mostly used the commercially available instruments, we still built some circuits for data acquisition. With the development of nano-technology, in the future, we will need more sophisticated electronics to acquire and analyze our data. Mainly, we need circuits with greater precision. For example, with the available resources we could not increase the force resolution because we were limited by the frequency resolution. Besides the electronics, we also studied vacuum technology that includes building a system to control the pressure of the gas

then the measurement of that pressure. A careful use of cryogenics also was needed to analyze the low-temperature effects.

In addition, another area of research that could not be avoided was fluid dynamics. While calibrating the quartz tuning fork with respect to pressure, we observed squeeze-film effect, and we used finite element analysis to complete the calibration. We used several approximations for the hydrodynamic function and a detailed calculation is required for more accurate results. However, we did not complete the verification of structure and transport properties of niobium nanowire using the QTF method, partly because of the limited scope and partly because the development of MCBJ, which is a more accurate method. Since, we explored the problem from multiple dimensions and so this dissertation opens the scope for several research fields.

APPENDIX A

MEASUREMENT OF TRANSFER FUNCTION

Appendix A investigates the measurement transfer function of a quartz tuning fork using FFT. We used a Stanford Research SR780 Network Analyzer for all our measurements and *Labview* to transfer the data to computer where we complete the analysis.

A.1 Stanford Research SR780 Network Analyzer Set-up

The following section gives a stepwise description for the set-up of the network analyzer. **Preset:**

1. Press **System** to display the System menu.
2. Press <**Preset**> to return the unit to its default settings.
3. Press **Enter** to confirm preset. This step is required to prevent accidental reset. Wait until the self tests are completed.
4. Use a BNC Tee to connect the **Source Output** to the QTF input and **Ch1 A Input**. Also connect the QTF output to **Ch2 A Input**. In this instrument, transfer function is defined as Ch2 response over Ch1 reference. Thus, Ch1 monitors the QTF input (source output), and Ch2 measures the response of the device under test.

Source: Press **Source** to select the source menu.

1. Press <**Chirp**> to choose Chirp output, which is an equal amplitude sine wave at each frequency bin of the FFT spectrum.

2. Using the knob, set the amplitude to 1 Volt.
3. Press **Window** to select the Window menu.
4. Press **<Window>** to adjust the FFT Window function.
5. Select **(Uniform)** with the knob and press **Enter**. The Chirp source requires the use of the Uniform window since not all chirp frequency components are present at all points in the time record. The chirp is exactly periodic with the FFT time record and does not leak with the uniform window.
6. Press **Auto Range** for Ch1 and Ch2 to let the analyzer automatically set the Input Ranges to agree with the signals.

Frequency: Press **Freq** to select the Frequency menu.

1. Press **** to adjust the FFT Span. Use the knob to adjust the **Span** to 125 Hz and **Center frequency** to 32768 Hz and press **Enter**.

Display Setup: Press **Display Setup** to select the Display Setup menu.

1. Press **<Measurement>** to adjust the Measurement of the active DisplayA.
2. Select **<F2/F1>** with the knob to choose Transfer Function (the ratio of the response (Ch2) to the input (Ch1)) for the Measurement in DisplayA (top) and press **Enter**.
3. Press **<Units>** to change the Units to **dB** and press **Enter**.
4. Press **Active Display** to make DisplayB (bottom) the active display.
5. Follow the previous steps of Display setup and select **(Phase)** with the knob and press **Enter**.

Display option: Press **Display Options** to select the Display Options menu.

1. Select (Log) with the knob to display response function in Log scale and press **Enter**.

Marker: Press **Marker** Select the Marker menu.

1. Press <Width> to adjust the Marker Width for DisplayA and select (Normal) (Width = 1/2 division) with the knob, then press **Enter**.
2. Press <Seeks> to adjust what the Marker Seeks within the Marker Region and select (Max) with the knob and press **Enter**.
3. The **Link** key links the two display markers together. This allows simultaneous readout of Transfer Function Magnitude (top) and Phase (bottom).

A.2 Labview Setup

We used the SR780 Network Analyzer Labview package to transfer our data to the computer. The downloaded data was separated into x and y coordinate systems and simultaneous plots were obtained. The front panel of Labview is shown in Fig. 50.

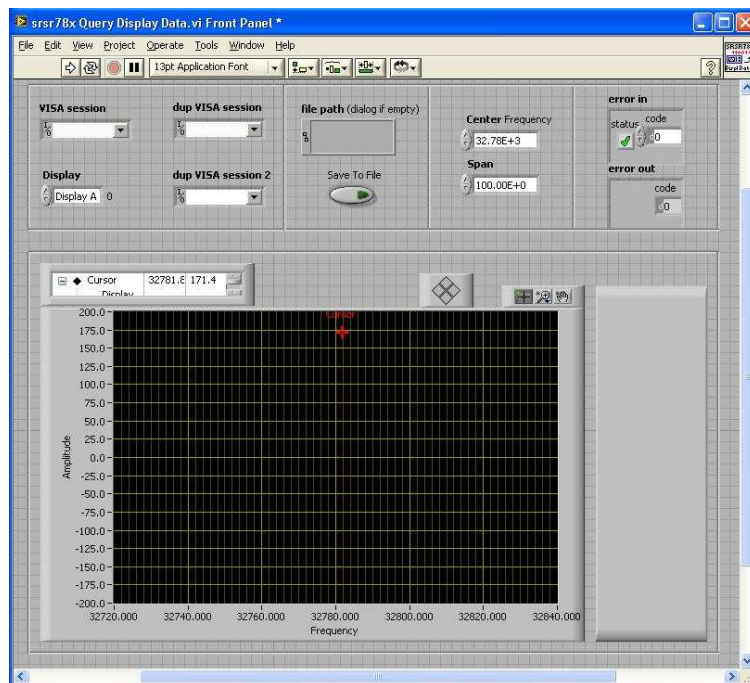


Figure 50: Labview front panel for data acquisition from SR780 network analyzer.

APPENDIX B

MODELING IN COMSOL MULTIPHYSICS

The model is implemented using three application modes that the predefined **Fluid-Structure Interaction** multiphysics entry sets up automatically. First, the **Incompressible Navier -Stokes** application mode computes the fluid dynamics. This mode is active in the area of the flow channel, and this model performs its computations with the total stress tensor form. Further, we implement the boundary conditions with non-ideal weak constraints. This setup results in a more accurate computation of the boundary conditions. The Lagrange multipliers, computed with the non-ideal weak constraints, correspond to the negative of the x - and y -components of the fluid force. Therefore it is not necessary to solve this force separately. Instead the Lagrange multipliers define the loads in the Plane Strain application mode. Second, the Plane Strain application mode solves the model's structural mechanics portion. We activate it in the area of the cantilever. To get a more accurate computation of the large strains, the large deformation analysis type is the default setting. The deformation velocity solved with this application mode acts as the boundary condition for the Incompressible Navier-Stokes and the Moving Mesh (ALE) application modes. Third, the Moving Mesh (ALE) application mode solves for the deformed mesh. The application modes as used here form a differential-algebraic equation (DAE) system, because not all the equations depend on time. This means that the application modes (in the discrete system) have several algebraic equations that do not contain time-dependent terms. Therefore, to speed up the computations, one can activate advanced time-stepping settings to exclude the algebraic equations from the error estimation and to use the

singular mass matrix. For more accurate results, one must reduce the absolute tolerance values for the time stepping.

Model Navigator

1. In the **Model Navigator**, select **2D** from the **Space dimension** list.
2. From the list of application modes, select **MEMS Module>Fluid-Structure Interaction>Plane Strain with Fluid Interaction>Transient analysis**.
3. Click **OK** to close the **Model Navigator**.

Geometry Modeling

1. Go to the **Draw** toolbar and shift-click the **Rectangle/Square** button.
2. To generate the box containing the air, enter 2.436×10^{-2} in the **Width** edit field and 1.862×10^{-2} in the **Height** edit field. Also set the origin of the rectangle to 1.18×10^{-2} for x -coordinate and to 8.1×10^{-3} for y -coordinate. Click **OK** to close the dialog box.
3. Now to generate the cross-section of the cantilever, shift-click the **Rectangle/Square** button again and enter 5.0×10^{-4} in the **Width** edit field and 6.0×10^{-4} in the **Height** edit field. The origin of this rectangle is set to 1.525×10^{-4} for x -coordinate and 5.5×10^{-5} for y -coordinate. Click **OK**.

Physics Settings

1. From the **Options** menu, choose **Constants** and define the following constants with names and expressions:

Name	Expression
mu	10^{-3}
rho	100
u_{\max}	5×10^{-2}
E	2×10^5

2. Again from the **Options** menu, go to **Expressions** and then click **Boundary Expressions**. Enter the following equation for boundary 1 and click **OK**.

$$u_{\text{in}} = \frac{U.t^2}{\sqrt{(0,04 - t^2)^2 + (0,1.t^2)^2}} \quad (122)$$

Subdomain Settings

1. From the **Multiphysics** menu, make sure **Incompressible Navier-Stokes (mmglf)** is selected. Then in the **Subdomain Settings** dialog box select subdomain 1 and in the **Group** list select **Fluid domain**. Choose the density and viscosity for air at room temperature and pressure. Leave the remaining settings to default.
2. To deactivate the incompressible Navier-Stokes equations in subdomain 2 (the solid), select subdomain 2 then in the **Group** list select **Solid domain** before closing the dialog box.
3. Now we set the **Plane Strain (smpn)** settings in the **Multiphysics** menu.
4. Deactivate the structural mechanics equations in the fluid by selecting subdomain 1, then in the **Subdomain Settings** dialog box in the **Group** list select **Fluid domain**.
5. Now select subdomain 2 then select **Solid domain** in the **Group** list and enter E in the E edit field for the Young's modulus. The remaining parameters are left to default.
6. The **Subdomain Settings for Moving Mesh (ALE)** are such that the subdomain 1 is free to move and subdomain 2 moves has **Displacement variables** set to u, v .

Boundary conditions

1. From the **Multiphysics** menu, select **Incompressible Navier-Stokes (mmglf)** to define the boundary setting for fluid region and apply the following boundary conditions on the active boundaries:

Boundary	1	2-4	5-7	8
Type	Inflow/Outflow velocity	No Slip	No Slip	Pressure
x velocity	u_{in}	0	ut	0
y velocity	0	0	vt	0

2. The boundary settings for **Plane Strain (smpn)** application mode are left as default.
3. For **Moving Mesh (ALE)** all the boundaries are set to **Mesh displacement**.

Mesh generation

The mesh parameters are set to default. The resulting triangular mesh is shown in Fig. 51.

Computing the Solution

1. From the **Solve** menu choose **Solver Parameters**.
2. In the **Times** edit field enter 0:0.00005:0.0005 sec.
3. Type 1e-3 in the **Absolute Tolerance** edit field to provide sufficient accuracy in the time stepping and leave the remaining parameters on their default values.
4. From the **Solve** menu choose the **Solver Manager**.
5. On the **Initial Value** page go to the initial value area and click the **Initial Value Expression** option button. Close the dialog box and click the **Solve** button on the main toolbar to solve the equations.

Postprocessing and Visualization

1. From the **Postprocessing** menu choose **Plot Parameters**.
2. On the **General** page find the **Plot Type** area; select the **Surface**, and **Streamline** check boxes, then clear all the other check boxes.

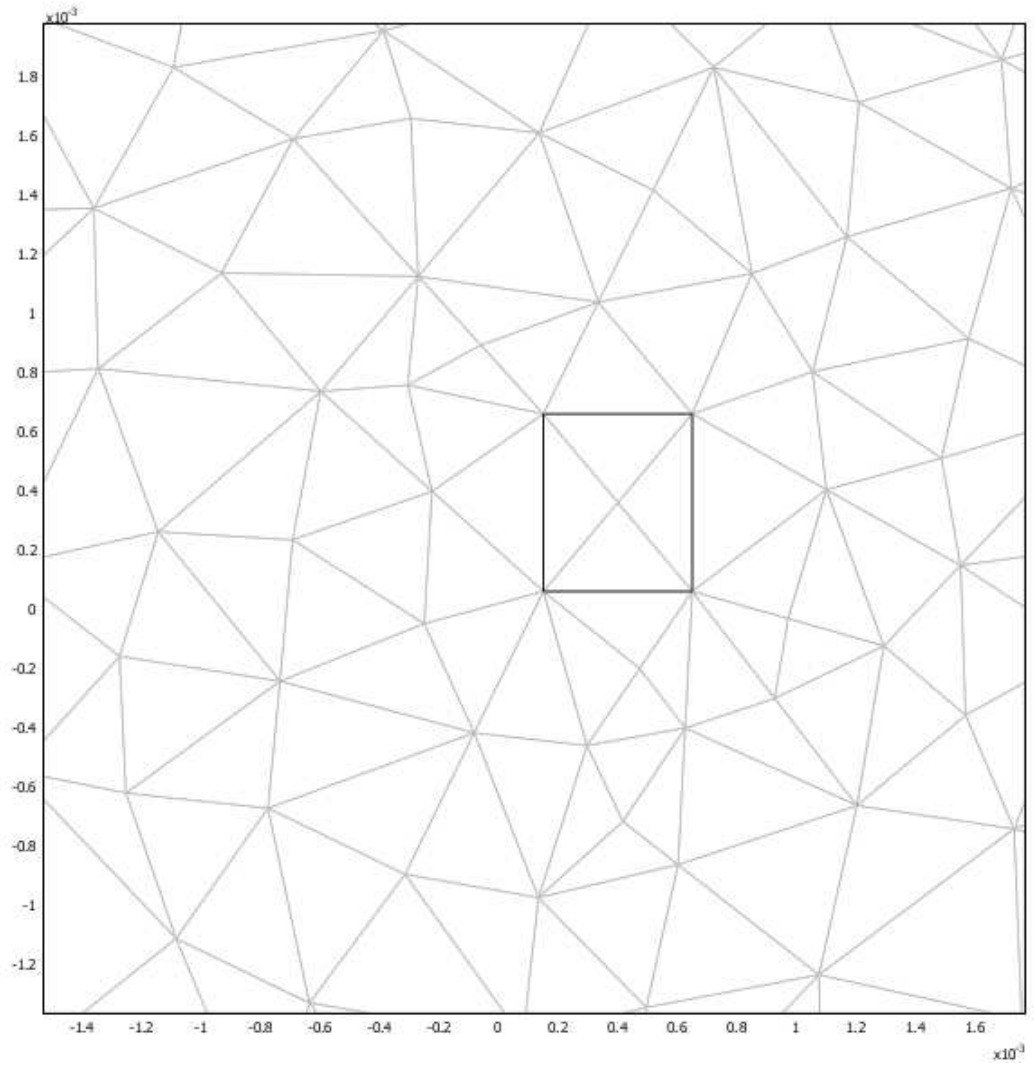


Figure 51: Mesh generated from the finite-element analysis.

3. On the **Surface** page go to the **Predefined** quantities list on the **Surface Data** tab, and select **Pressure** field in the list of quantities under **Incompressible Navier- Stokes**.
4. Click the **Uniform Color** option button, click the **Color** button, and set the color to **grey**.
5. Click the **Streamline** tab, and select **Velocity Field (ns)** from the **Predefined** quantities list.
6. To calculate the values of force and vorticity on the boundaries, click **Boundary Integration** from the **Postprocessing** menu. Select the corresponding **Pressure** and **Vorticity** in the **Predefined Quantities** and the numerical values in the bottom of the windows. We calculated these values for a range of velocity, u_{max} such that it defines the required Reynold's number range. The resulting plot is shown in Fig. 27.

APPENDIX C

PHASE LOCK LOOP CHIP MC14046B CONFIGURATION

As shown in Fig. 52, MC14046B has two phase comparators, a VCO, a source follower, and a zener diode. The two comparators have two common signal inputs, PCA_{in} and PCB_{in} . Input PCA_{in} can be coupled directly to large voltage signals or indirectly (with a series capacitor) to small voltage signals. The self-bias circuit adjusts small voltage signals in the linear region of the amplifier. Phase comparator 1 (an exclusive OR gate) provides a digital error signal $PC1_{out}$ and maintains 90° phase shift at the center frequency between PCA_{in} and PCB_{in} signals (both at 50% duty cycle). Phase comparator 2 (with leading edge sensing logic) provides digital error signals, $PC2_{out}$ and LD, and maintains a 0° phase shift between PCA_{in} and PCB_{in} signals (duty cycle is immaterial). The linear VCO produces an output signal VCO_{out} whose frequency is determined by the voltage of input VCO_{in} and the capacitors and resistors connected to pins $C1_A$, $C1_B$, R_1 and R_2 . The source-follower output SF_{out} with an external resistor is used where the VCO_{in} signal is needed but no loading can be tolerated. The inhibit input Inh , when high, disables the VCO and source-follower to minimize standby power consumption. The zener diode can be used to assist in power supply regulation.

VCO Configuration: The power supply was connected. High voltage +10 volts to pin 16 (V_{DD}) and ground to pin 8 (V_{SS}). The VCO gives an output frequency signal at VCO_{out} (pin 4) depending upon the dc voltage at VCO_{in} (pin 9). The voltage can be between V_{SS} to V_{DD} . No other input signal (input for Phase detectors) is necessary of this configuration. However, depending upon the input voltage at VCO_{in} the

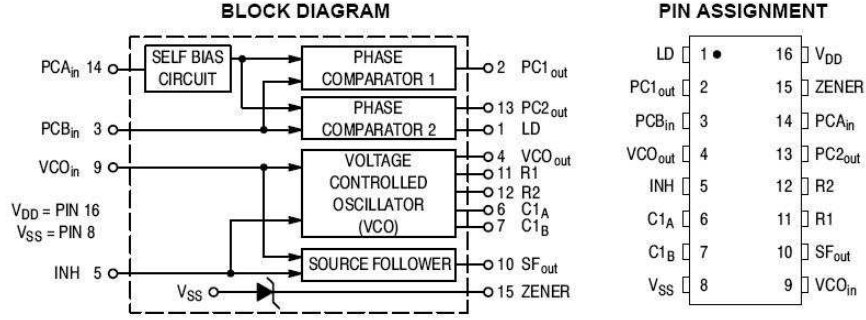


Figure 52: Block diagram and pin assignment of the microchip MC14046B commercially produced by On Semiconductor.

VCO_{out} frequency can vary between f_{\min} to f_{\max} . Note: This relationship between input voltage and output frequency is linear. The f_{\min} and f_{\max} are determined by the resistors and capacitors connected to pins 6, 7, 11, and 12 of the chip. Resistor R_1 connected to pin 11, R_2 connected to pin 12, and Capacitor C_1 connected between pins 6 and 7. The other ends of R_1 and R_2 are grounded. Now f_{\min} & f_{\max} are given by following expressions

$$f_{\min} = \frac{1}{R_2(C_1 + 32 \text{ pF})}, \quad (123)$$

where VCO_{in} = V_{SS}, and

$$f_{\max} = f_{\min} + \frac{1}{R_1(C_1 + 32 \text{ pF})} \quad (124)$$

where in this case VCO_{in} = V_{DD}. The 32 pf is a chip characteristic capacitor that has to be added in the equation for calculating the frequency. The range of R_1 , R_2 and C_1 is as follows:

$$10 \text{ k}\Omega \leq R_1 \leq 1 \text{ M}\Omega, \quad (125)$$

$$10 \text{ k}\Omega \leq R_2 \leq 1 \text{ M}\Omega, \quad (126)$$

$$100 \text{ pF} \leq C_1 \leq .01 \text{ }\mu\text{F}. \quad (127)$$

For our experiment we selected $R_1 = 30.1 \text{ k}\Omega$, $R_2 = 806 \text{ k}\Omega$, and $C_1 = 2.15 \text{ nF}$. This gives $f_{\min} = 15,225.75 \text{ Hz}$. We adjusted the input voltage for the chip from 10.0 V to 6.8 V to set the f_{\min} to 32 kHz. f_{\max} is given by $f_{\min} + 568.60 \text{ Hz}$. A direct

method of relating the f_{\max} to input voltage for the chip could not be found and so we measured experimentally using a Stanford Research Network Analyzer. The difference $\Delta f = 2f_L = f_{\max} - f_{\min} = 903$ Hz was observed for a change in VCO_{in} from 0 to 6.8 V DC. This configuration gives a resolution of 7.5 mV for 1 Hz change in frequency.

Phase Comparator, Low-Pass Filter, and Source-Follower Configuration: We tried Phase Comparator 1 and Phase Comparator 2 for our experiment; Phase Comparator 1 was selected. The datasheet of the chip shows that the output for first comparator is simpler than the 2nd one, so we used the first comparator for our experiment. We used the Filter A as the Low-Pass filter. $C = 2.15$ nF and $R = 197.6 \Omega$. The result is:

$$f_C \approx \frac{1}{2\pi} \sqrt{\frac{2\pi f_L}{RC}} = 1.3 \text{ kHz.} \quad (128)$$

This is an error in the configuration since the data sheet says that for 2nd phase comparator, $f_C \leq f_L$. Appropriate values for R and C are given as follows:

$$R \leq 35.3\text{K}\Omega,$$

$$C = 0.01\mu\text{F}.$$

REFERENCES

- [1] HOHENBERG, P. and KOHN, W., “Inhomogeneous electron gas”, *Physical Review*, vol. 136, p. B864-B871, 1964.
- [2] KOHN, W. and SHAM, L. J., “Self-consistent equations including exchange and correlation effects”, *Physical Review*, vol. 140, p. A1133-A1138, 1965.
- [3] MARCHENKOV, A., DAI, Z., ZHANG, C., BARNETT, R. N., and LANDMAN, U., “Atomic dimer shuttling and two-level conductance fluctuations in niobium nanowires”, *Phys. Rev. Lett.*, vol. 98, p. 046802(4), 2007.
- [4] GROSSO, G. and PARRAVICINI, G. P., *Solid State Physics*, Academic Press, 2000.
- [5] SZABO, A. and OSTLUND, N. S., *Modern Quantum Chemistry*, McGraw-Hill, New York, 1989.
- [6] HEDIN, L., “New method for calculating the one-particle Green’s function with application to the electron-gas problem,” *Phys. Rev.*, vol. 139, p. A796, 1965.
- [7] CEPERLY, D. M. and ALDER, B. J., “Ground state of the electron gas by a stochastic method”, *J. Chem. Phys.*, vol. 45, p. 566-569, 1980.
- [8] WILK, L., VOSKO, S. J. and NUSAIR, M., “Accurate spin-dependent electron liquid correlation energies for local spin density calculations: a critical analysis”, *Can. J. Phys.*, vol. 58, p. 1200-1211, 1980.
- [9] PERDEW, J. P. and ZUNGER, A., “Self-interaction correction to densityfunctional approximations for many-electron systems”, *Phys. Rev. B*, vol. 23, p. 5048-5079, 1981.
- [10] VOSKO, S. H., JACKSON, K. A., PEDERSEN, M. R., SINGH, D. J., PERDEW, J. P., CHEVARY, J. A., and FIOLOHAIS, C., “Atoms, molecules and surfaces: Application of the generalized gradient approximation from exchange and correlation,” *Phys. Rev. B*, vol.46, p. 6671-6687, 1992.
- [11] PERDEW, J. P., *Electronic Structure of Solids*, Akademie Verlag, Berlin, 1991.
- [12] BURKE, K., PERDEW, J. P., and ERNZERHOF, M., “Generalized gradient approximation made simple,” *Phys. Rev. Lett.*, vol. 77, p. 3865-3868, 1996.
- [13] HANSEN, L. B., HAMMER, B., and NORSKOV, J. K., “Improved adsorption energetics within density functional theory using revised perdue-burke-ernzerhof functionals,” *Phys. Rev. B*, vol. 59, p. 7413-7421, 1999.

- [14] KRESSE, G. and JOUBERT, D., “From ultrasoft pseudopotentials to the projector augmented-wave method,” *Physical Review B*, vol. 59, p. 17581775, 1999.
- [15] VANDERBILT, D., “Soft self-consistent pseudopotentials in a generalized eigenvalue formalism,” *Phys. Rev. B*, vol. 41, p. 7892, 1990.
- [16] SCHLÜTER, M., HAMANN, D. R., and CHIANG, C., “Norm-conserving pseudopotentials,” *Phys. Rev. Lett.*, vol. 43, p. 1494-1497, 1979.
- [17] TROULLIER, N., and MARTINS, J. L., “Efficient pseudopotentials for plane-wave calculations,” *Phys. Rev. B*, vol. 43, 1991.
- [18] ALLAN, D. C., ARIAS, T. A., PAYNE, M. C., TETER, M. P., and JOANNOPOULOS, J. D., “Iterative minimization techniques for ab initio total energy calculations: molecular dynamics and conjugate gradients,” *Reviews of Modern Physics*, vol. 64, p. 10451097, 1992.
- [19] ARIAS, T. A., LIPPERT, R. A., and EDELMAN, A., “Multiscale computation with interpolating wavelets,” *Journal of Computational Physics*, vol. 140, p. 278310, 1997.
- [20] GALE, J. D., GARCIA, A., JUNQUERA, J., ORDEJÓN, P., SOLER, J. M., ARTACHO, E. and SÁNCHEZ-PORTAL, D., “The siesta method for *ab initio* order-n materials simulation,” *Journal of Physics: Condensed Matter*, vol. 14, p. 2745-2779, 2002.
- [21] The official homepage for the Gaussian electronic structure program: <http://www.gaussian.com>.
- [22] The official homepage of SIESTA program: <http://www.uam.es/departamentos/ciencias/fismateriac/siesta>
- [23] SOHN, KI-SOO, LEE, SEONGBOK, BYLANDER, D.M., and KLEINMAN, LEONARD, “Nb₂ dimer: Examination of singlet and triplet character,” *Physical review B*, vol. 39, p. 9983-9986, 1989.
- [24] KELDYSH, L. V. “Diagram technique for non-equilibrium processes,” *Soviet Physics JETP-USSR*, vol. 20, p. 1018, 1965.
- [25] KADANOFF, L. P. and BAYM, G., *Quantum Statistical Mechanics*, Benjamin, 1962.
- [26] HAUG, H. and JAUHO, A.-P., *Quantum Kinetics in Transport and Optics of Semi-conductors*, Springer, 1998.
- [27] DATTA, S., *Electronic Transport in Mesoscopic Systems*, Cambridge University Press, 1995.
- [28] FERRY, D. K. and GOODNICK, S. M., *Transport in Nanostructures*, Cambridge University Press, 1997.

- [29] YEYATI, A. L., AGRAIT, N., and RUITENBEEK, J. M. VAN, “Quantum properties of atomic-sized conductors,” *Physics Reports*, vol. 377(81), p. 279, 2003.
- [30] WANG, Z. L., FRANK, S., PONCHARAL, S. P., and DE HEER, W. A., “Carbon nanotube quantum resistors,” *Science*, vol. 280, p. 1744-1746, 1998.
- [31] LANDAUER, R., “Spatial variation of currents and fields due to localized scatterers in metallic conduction,” *IBM J. Res. Dev.*, vol. 1, p. 223-231, 1957.
- [32] GRIFFITHS, D., *Introduction to Quantum Mechanics*, New Jersey: Pearson, 2 ed., 2004.
- [33] MARTIN, T. and LANDAUER, R., “Wave-packet approach to noise in multichannel mesoscopic systems,” *Phys. Rev. B*, vol. 45, p. 1742, 1987.
- [34] BUTTIKER, M., “Scattering theory of current and intensity noise correlations in conductors and wave guides,” *Phys. Rev. B*, vol. 46, pp.12485-12507, 1992.
- [35] BUTTIKER, M., IMRY, Y., LANDAUER, R., and PINHAS, S., “Generalized many-channel conductance formula with application to small rings,” *Phys. Rev. B*, vol. 31, p. 6207, 1985.
- [36] The official homepage of Atomistix Tool Kit program:
www.atomistix.com.
- [37] GARCIA, N., COSTA-KRAMER, J.L., GIL, A., MARQUES, M.I., and CORREIA, A., “Conductance quantization in metallic nanowires NATO ASI Series,” *Series E: Applied Sciences*, vol. 345, p. 581, 1997.
- [38] TAYLOR, J., GUO, H., and WANG, J., “Ab initio modeling of quantum transport properties of molecular electronic devices,” *Physical Review B*, vol. 63, p. 245407, 2001.
- [39] BRANDBYGE, M., JOSE-LUIS MOZOS, ORDEJÓN P., TAYLOR, J., and STOKBRO, K., “Density functional method for nonequilibrium electron transport,” *Physical Review B*, vol. 65, p. 165401, 2002.
- [40] THYGESEN, K.S., BOLLINGER, M.V., and JACOBSEN, K. W., “Conductance calculations with a wavelet basis set,” *Physical Review B*, vol. 67, p. 115404(11), 2003.
- [41] SEMENOFF, G.W., “Condensed-matter simulation of a three-dimensional anomaly,” *Phys. Rev. Lett.*, vol. 53, p. 2449-2452, 1984.
- [42] FRADKIN, E., “Critical behavior of disordered degenerate semiconductors,” *Phys. Rev. B*, vol. 33, p. 3263-3268, 1986.
- [43] HALDANE, F.D.M., “Model for a quantum Hall effect without Landau levels: Condensed-matter realization of the ‘parity anomaly’,” *Phys. Rev. Lett.*, vol. 61, p. 2015-2018, 1988.

- [44] NOVOSELOV, K.S. et al., “Electric field effect in atomically thin carbon films,” *Science*, vol. 306, p. 666-669, 2004.
- [45] NOVOSELOV, K.S. et al., “Two-dimensional atomic crystals,” *Proc. Natl Acad. Sci. USA*, vol. 102, p. 10451-10453, 2005.
- [46] NOVOSELOV, K.S. et al., “Two-dimensional gas of massless Dirac fermions in graphene,” *Nature*, vol. 438, p. 197-200, 2005.
- [47] ZHANG, Y., TAN, J.W., STORMER, H.L., KIM, P., “Experimental observation of the quantum Hall effect and Berry’s phase in graphene,” *Nature*, vol. 438, p. 201-204, 2005.
- [48] RYCERZ, A., TWORZYDLO, J., BEENAKKER, C.W.J., “Valley filter and valley valve in graphene,” *Nature Physics*, vol. 3, p. 172-175, 2007.
- [49] YOUNG-WOO SON, MARVIN, L.C., and STEVEN G.L., “Half-metallic graphene nanoribbons,” *Nature*, vol. 444, p. 347-349, 2006.
- [50] ANDERSON, P. W., “Absence of diffusion in certain random lattices,” *Physical Review B*, vol. 109, p. 1492-1505, 1958.
- [51] BIEL, B., GRACÍA-VIDAL, F.J., RUBIO, A., and FLORES, F., “Anderson localization in carbon nanotubes: defect density and temperature effects,” *Physical Review Letters* vol. 95, p. 266801 2005.
- [52] GORNYI, I.V., MIRLIN, A.D., and POLYAKOV D.G, “Dephasing and weak Localization in disordered Luttinger liquid,” *Physical Review Letters* vol. 95, p. 046404 2005.
- [53] LI, T.C. and LU, SHAO-PING, “Quantum conductance of graphene nanoribbons with edge defects,” *Phys. Rev. B*, vol. 77, p. 085408, 2008.
- [54] FANU, U., “Effects of configuration interaction on intensities and phase shifts,” *Phys. Rev.*, vol. 124, p. 1866-1878, 1961.
- [55] ROSALES, L., PACHECO, M., BARTICEVIC, Z., LATGÉ, A., and ORELLANA, P.A., “Transport properties of graphene nanoribbons with side-attached organic molecules,” *Nanotechnology*, vol. 19, p. 065402, 2008.
- [56] GIESSIBL, F., “High-speed force sensor for force microscopy and profilometry utilizing a quartz tuning fork,” *Applied Physics Letters*, vol. 73, p. 3956, 1998.
- [57] SADER, J., “Frequency response of cantilever beams immersed in viscous fluids with applications to the atomic force microscope,” *Journal of Applied Physics*, vol. 84(1), p. 64-76, 1998.
- [58] TUCK, E., “Calculation of unsteady flows due to small motions of cylinders in a viscous fluid,” *Journal of Engineering Mathematics*, vol. 3(1), p. 29-44, 1969.

- [59] KARRAI, K. and GROBER, R., “Piezo-electric tuning fork tip-sample distance control for near field optical microscopes,” *Ultramicroscopy*, vol. 61(1-4), p. 197-205, 1995.
- [60] DORIGNAC, J., KALINOWSKI, A., ERRAMILI, S., and MOHANTY, P., “Dynamical response of nanomechanical oscillators in immiscible viscous fluid for in vitro biomolecular recognition,” *Physical Review Letters*, vol. 96(18), 2006.
- [61] CHRISTEN, M., “Air and gas damping of quartz tuning forks,” *Sensors and Actuators*, vol. 4(4), p. 555-564, 1983.
- [62] “Torr Seal Resin Sealant,” Varian, Inc.
- [63] National Institute of Standards and Technology.
- [64] BINNIG, G. and SMITH, D. P. E., “Single-tube three-dimensional scanner for scanning tunneling microscopy,” *Rev. Sci. Instrum.*, vol. 57(8), p. 1688, 1986.
- [65] MÜLLER, J., The official home page is: <http://www.e-basteln.de>.
- [66] DAI, Z., “Coherent and Dissipative Transport in Metallic Atomic-Size Contacts”, *Georgia Institute of Technology*, 2006.
- [67] DONEHOO, B. “A Superconducting Investigation of Nanoscale Mechanics in Niobium Quantum Point Contacts,” *Georgia Institute of Technology*, 2008.
- [68] KWOK, P. Y. and BREUER, K. S., “Fluid effects in micromachined structures,” *Journal of Micromechanical systems*, vol. 14(4), p. 770-781, 2005.
- [69] GROSS, W. A., *Gas film lubrication*, John Wiley and Sons, Inc., New York, 1962.
- [70] GRIFFIN W. S., RICHARDSON H. H., and YAMRANAMI S., “A study of fluid squeeze-film damping”, *Journal of Basic Eng., Trans. ASME*, p. 451-456, June 1966.
- [71] VEIJOLA T., H. KUISMA, J. LAHDENPERA, and T. RYHANEN, “Equivalent-circuit model of the squeezed gas film in a silicon accelerometer,” *Sensors and actuators A-Physical*, vol. 48(3), p 239-248, 1995.
- [72] FUKUI S. and KANEKO R., “Analysis of ultra-thin gas film lubrication based on linearized Boltzman equation: first report - derivation of generalized lubrication equation including thermal creep flow”, *Journal of Tribology Trans. ASME*, 110, p. 253-262, 1988.
- [73] MOORE, WALTER J., *Physical Chemistry*, Prentice-Hall. Inc. N.J., 3rd Edition, p. 225.

- [74] CLUBB, D. O., BUU, O. V. L., BOWLEY, R. M., NYMAN, R., and QWERS-BRADLEY, J. R., "Quartz tuning fork viscometers for helium liquids," *Journal of Low Temperature Physics*, vol. 136, p. 1-13, 2004.
- [75] BLECH, J. J., "On isothermal squeeze films," *Journal of Lubrication Technology*, vol. 105, p. 615-620, 1983.

VITA

Sanjay Bidasaria was born on August 13, 1979 in Kolkata, India, where he grew up and went to school. In 1999, he was admitted in Indian Institute of Technology, Kharagpur, India, where he completed his Bachelors in Science in Physics by 2003. After this, he joined Georgia Institute of Technology in Fall 2003 for his graduate studies. He completed his special problems with Professor Elisa Reido and then began working in Professor Alexei Marchenkov's lab, who would eventually become his graduate advisor. Sanjay completed a Masters in Physics in 2005, as well as an additional Minor in Finance in 2007; as well, throughout this period he continued working on research in Dr. Marchenkovs lab. Finally, on October 13th of 2008, Sanjay defended his doctoral thesis and finished his schooling.